Title
Near-Infrared to Visible Hybrid Molecule-Nanocrystal Photon Upconversion

Author
Mahboub, Melika

Publication Date
2018

UNIVERSITY OF CALIFORNIA
RIVERSIDE

Near-Infrared to Visible Hybrid Molecule-Nanocrystal Photon Upconversion

A Dissertation submitted in partial satisfaction
of the requirements for the degree of

Doctor of Philosophy

in

Materials Science and Engineering

by

Melika Mahboub

September 2018

Dissertation Committee:
    Dr. Ming Lee Tang, Chairperson
    Dr. Roger Lake
    Dr. Lorenzo Mangolini

The Dissertation of Melika Mahboub is approved:

Committee Chairperson

University of California, Riverside

Acknowledgement

It’s been an unforgettable moment for me to study as a Ph.D in materials science and engineering program for five years. In such an amazing period I achieved a lot of accomplishments both in my carrier as well as my personal life. I experienced a lot of love, joy and friendship. With this I want to appreciate all who supported me with their professional help and love.

First, I would like to sincerely appreciate my advisor Dr. Ming Lee Tang. It was an honor to work with Ming Lee Tang for four years at UC Riverside. Thanks for training me and showing me how to be a good scientist. I appreciate all your patience and all the efforts you put to correct me when I was wrong. Working in your lab was such a blessing and it is unforgettable. You showed me the critical thinking, endeavor and how to be more efficient. You showed me how to solve any problems even though they look difficult at the first glances. You were always there and supported me whenever I needed you. Thanks for being such a great advisor.

I would like to thank my committee members, Dr. Roger Lake and Dr. Lorentzo Mangolini. They gave me a valuable suggestions in my research. I want to thank Dr. Cengiz Ozkan who was the committee member of my qualifying exam. Thanks for encouraging me and expressing good comments and questions during the exam.

I want to thank all my lab mates who supported me so professionally in my research. My special thanks are to Zhiyaun Huang, Xin Li, Pan Xia, Emily Moses, Daryl Hawkes, Carter Gerke. I want to thank my great undergraduate mentee, Narek Megerdich and my awesome high school mentee, Andrew Minh Pam who were so helpful in proceeding my projects. I wish them the best in proceeding their professional career. I thank all the alumni who have helped in my research and made my Ph.D memorable.

I thank all my collaborators who taught and helped me with the knowledge of the field out of my expertise. They are Dr. Christopher J. Bardeen, Dr. Tianquan Lian, Dr. Graham Kenneth, Dr. Chun H. Lui, Dr. Hill Harman. Thanks for being such good collaborators.

Last but not least, I want to appreciate my parents and sisters. Even though my father, Mahboub Mahboub is not present in my life physically, he is in my thought every day. This Ph.D. is because of you dad as you wanted me to be educated at the highest level and your love is always in my heart. I thank my mother Iran Montazerolghaem for encouraging me all the time and loving me for who I am. Mom you are a strong independent woman who showed me an endeavor and independence in life. I thank my sisters, Ramona Kennedy, Rona Mahboub, Sarona Mahboub, and Saina Mahboub who always supported me with their love and encouragement.

Acknowledgement of previously published material

1. Chapter 1 has been published in “Mahboub, M.; Maghsoudiganjeh, H.; Pham, A. M.; Huang, Z.; Tang, M. L. Adv. Funct. Mater. 2016, 6091-6097”.

2. Chapter 2 has been published in “Mahboub, M.; Huang, Z.; Tang, M. L. Nano Lett. 2016, 16 (11), 7169-7175”.

3. Chapter 3 has been published in “Mahboub, M.; Xia, P.; Jeremiah, V. B.; Li, X.; Chun, H. L.; Tang, M. L. ACS Energy Lett. 2018, 3, 767”.

4. Chapter 6 is referred from the supporting information of the above 3 publications.

ABSTRACT OF THE DISSERTATION

Near-Infrared to Visible Hybrid Molecule-Nanocrystal Photon Upconversion

by

Melika Mahboub

Doctor of Philosophy, Graduate Program in Materials Science and Engineering
University of California, Riverside, September 2018
Dr. Ming Lee Tang, Chairperson

Third generation photovoltaics are inexpensive modules that promise power conversion efficiencies exceeding the thermodynamic Shockley–Queisser limit, perhaps by using up or down-converters, intermediate band solar cells, tandem cells, hot carrier devices, or multiexciton generation. Photon upconversion has attracted enormous attention due to its wide range of applications in biological imaging, photocatalysis, and especially photovoltaics. Here, in the first chapter, the effect of quantum confinement on the efficiency of Dexter energy transfer from PbS and PbSe nanocrystals (NCs) to a rubrene acceptor is studied. A series of experiments exploring the relationship between NC size and the upconversion quantum yield (QY) in this hybrid platform show that energy transfer occurs in the Marcus normal regime. By decreasing the NC diameter from 3.5 to 2.9 nm for PbS and from 3.2 to 2.5 nm for PbSe, the relative upconversion QY is enhanced about 700 and 250-fold respectively. In addition, the dynamic Stern–Volmer constant (K_{SV}) for the quenching of PbSe NCs by rubrene increases approximately fivefold with a decrease in NC diameter from 3.2 to 2.5 nm to a value of 200 M^{-1}. This work shows that high quality, well-passivated, small NCs are critical for efficient triplet energy transfer to molecular acceptors. In the second chapter, we report an efficient upconversion of infrared to visible light. Colloidally synthesized core–shell lead sulfide– cadmium sulfide nanocrystals in combination with tetracene derivatives absorb near infrared light and emit visible light at 560 nm with an upconversion quantum yield (QY) of 8.4 ± 1.0%, which is a factor of 4 lower than the maximum upconversion QY possible. The molecular and nanocrystal engineering here paves the way toward utilizing this hybrid upconversion platform in photovoltaics, photodetectors and photocatalysis. In the third chapter, we study the effect of shell composition and thickness on triplet energy transfer (TET) from PbS QDs to rubrene in a hybrid organic–inorganic photon upconverison system and show that defect states introduced by surface adsorbed Zn and Cd result in up to 700 and 325 fold enhancements in the photon upconverison quantum yield (QY). Time-correlated single-photon counting, photoluminescence (PL), and photon upconversion QY measurements on PbS QD light absorbers with submonolayer shells of 0.37–1.60 Å of CdS and 0.04–0.22 Å of ZnS reveal these core–shell QDs have reduced radiative and nonradiative rates relative to the core. Their broadened absorption and PL line widths suggest TET may occur from thermally accessible surface defects, in addition to the dark excitonic states at the band-edge. Finally by study the photophysics and electronic properties of differently sized PbS and PbSe QDs we study the effect of composition in the photon upconveersion process and we demonstrate that appropriate QDs synthesis precursors are essential for gaining high quality QDs that results in efficient upconversion QY of ~12%.

Table of Contents

List of Figures:

4.1.2.2 TET rate from NC PL quenching

List of Tables:

Chapter 1 Triplet energy transfer from PbS(Se) nanocrystals to rubrene: the relationship between the upconversion quantum yield and size.

1.1 Introduction

Colloidally synthesized nanocrystal (NCs) that are quantum confined behave like artificial atoms with discrete energy levels. Like their molecular counterparts, NCs may interact electronically with their environment, exchanging energy or charge. The role of NCs as donor (acceptor) depends on the environment, *e.g.* solvent, phase, temperature, its surface properties, and its band offsets relative to the potential acceptor (donor). With their size dependent optical properties and energy levels,[1] NCs have great potential as cost-effective components in various optoelectronic devices like solar cells,[2,3] light emitting diodes,[4,5] and transistors,[6,7] as well as bright labels for fluorescence based sensing[8,9] and diagnostics.

Here, the focus is on energy transfer between PbX NCs and rubrene, a conjugated hydrocarbon molecule (Figure 1a). This model system offers the prospect of improving the efficiency of solar cells via photon upconversion.[10,11] We[12] and others[13,14] recently discovered that semiconductor NCs can donate energy to the triplet states of molecules, denoted triplet energy transfer (TET) in Figure 1a. Using terminology developed by the molecular photon upconversion community,[15,16] NCs serve as sensitizers for molecular triplet states. In a spin-allowed process termed triplet-triplet annihilation (TTA), two molecules in their triplet excited state can interact and produce one molecule in its ground state, the other in its first excited singlet state, S_1. Thus in rubrene, two near-infrared (NIR) photons can be combined for the emission of one photon at the wavelength of ~560 nm (the emission maxima of rubrene). In principle, the use of PbX NC sensitizers and rubrene annihilators allows the upconversion of NIR photons up to 1.14 eV or ~1090 nm (the lowest excited triplet state, T_1 of rubrene).[17] This hybrid photon upconversion platform takes advantage of the high extinction coefficients of the NC sensitizer and its ability to absorb infrared photons more energetic than its bulk bandgap (0.4 eV and 0.28 eV for PbS and PbSe respectively). The ability to tune the NC bandgap based on its size is particularly favorable when contrasted with the narrow absorption cross-sections of the lanthanide sensitizer ions[18,19] that are difficult to spectrally modify, and the difficulty in finding molecular sensitizers that absorb strongly in the NIR without undergoing rapid internal conversion to the ground state.[20] Furthermore, PbX NCs generally have microsecond lifetimes,[21,22] making them suitable for energy transfer applications. The schematic of the energy transfer is shown in Figure 1a. The NC first absorbs NIR photons, then sensitizes the T_1 state of rubrene via triplet energy transfer (TET). Two rubrene molecules in their T_1 state can undergo triplet-triplet annihilation (TTA) to emit a visible photon.[23] The HOMO and LUMO levels of rubrene were measured in dichloromethane at RT by cyclic voltammetry[24], while the positions of the conduction and valence band of the PbX nanocrystals were estimated by Hyun et al.[25] Our previous work has indicated that energy transfer prevails in this hybrid system, with rubrene showing a delayed fluorescence due to sensitization by the PbS NCs with microsecond lifetimes.[12]

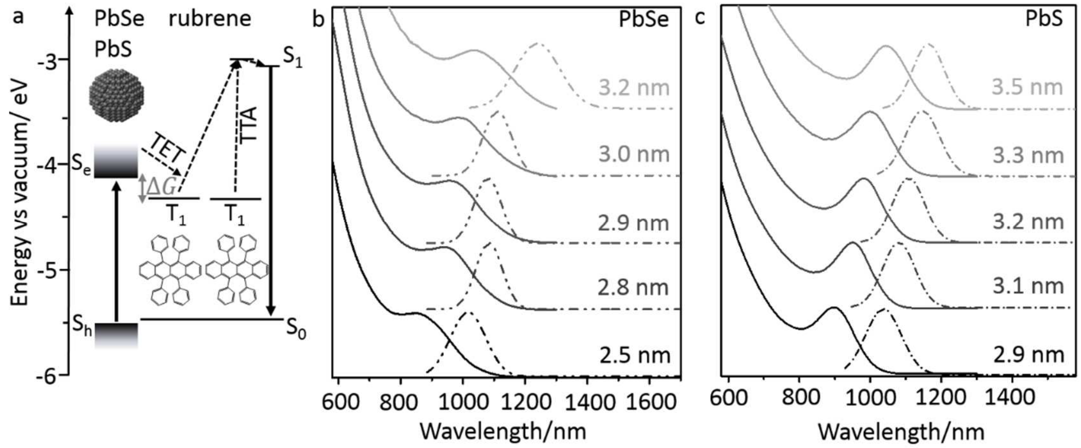

Figure 1.1. (a) Schematic of the energy transfer in a PbX nanocrystal (NC)-rubrene upconversion system. The energy levels of rubrene[24] are measured by cyclic voltammetry in dichloromethane. The absorption (solid line) and emission spectrum (dashed-dot line) of (b)-PbSe NCs and (c) PbS NCs of 5 different sizes in toluene at room temperature.

In this work, we investigate the effect of quantum confinement on the efficiency of triplet sensitization in this hybrid organic-inorganic rubrene-PbX NC system. A series of PbS and PbSe NC sensitizers with optical gaps equal to or larger than 1.1 eV were used in combination with rubrene molecules as annihilators. The efficiency of triplet energy transfer as a function of size was studied by two separate methods. Firstly, the relative upconversion efficiencies of a mixture of PbX NCs and rubrene in solution was measured. Secondly, a Stern-Volmer analysis of the steady-state energy transfer between PbSe donors and rubrene acceptors was conducted. We find that rubrene, as a triplet state acceptor for PbSe NCs, gives a Stern-Volmer quenching constant, $K_{SV} < 200$ M^{-1}. Here, we observe the smaller NCs result in higher photon upconversion, indicating that TET is in the Marcus normal regime. The correlation of NC size with upconversion quantum yield (QY) parallels our study on a related hybrid system, where CdSe NC sensitizers facilitate the upconversion of green to violet light in combination with diphenylanthracene annihilators.[26] This has implications for the ultimate efficiency of this hybrid system, and the design of NC-molecule combinations that utilize photon upconversion for imaging, photocatalysis, enhancing solar cell efficiencies, *etc.*

1.2 Results and discussion

1.2.1 Synthesis of different sizes of PbS/PbSe nanocrystals

We made small PbS and PbSe quantum dots colloidally by modifying the protocol reported by Ma et al.[2] When quantum confined, their excitonic absorption shifts hypsochromically towards the visible wavelengths. Ma et al. showed that extremely small PbSe NCs can be synthesized using a highly reactive Se precursor (bis(trimethylsilyl)selenide, TMS_2Se), and decreasing the injection temperature.[2] This decrease in temperature decreases the solubility of the Pb-X monomer and thus increases the number of nucleation sites, decreasing the final NC size. We made small PbS and PbSe NCs by decreasing both the injection temperature and the oleic acid concentration (Table 1 and Table 2). Oleic acid increases the solubility of the metal-chalcogenide monomer in the growth solution. In line with the simulations by Abe et al.,[27] this increased solubility promotes the growth of existing nuclei, increasing the NC size at the expense of NC concentration. Zhang et al. observed the same trend where PbSe NC size increases with an increase in oleic acid concentration.[28] For PbSe NCs, the oleic acid concentration was varied instead of injection temperature since $(TMS)_2Se$ is more reactive than $(TMS)_2S$, and high injection temperatures gave poor size control. Details on the NC synthesis are given in the methods section. The absorption and photoluminescence (PL) spectra of the synthesized PbSe, and PbS NCs are shown in Figure 1b and c respectively. Their first excitonic peaks range from 1.19 eV to 1.45 eV.

Table 1.1: Results of PbS QDs Synthesized at Different Injection Temperatures.

NC diameter [nm]	Temperature [°C]		Peak maxima [nm]$^{a)}$	
	Injection	Growth	Absorption	Emission
2.9	77	67	897	1036
3.1	90	80	950	1081
3.2	102	92	982	1108
3.3	110	98	998	1146
3.5	125	115	1044	1164

$^{a)}$ In toluene and room temperature. For all synthesis 2.0 ml oleic acid were added at the specified injection temperature. The NCs were held at the growth temperature for 2 minutes before quenching with ethanol.

Table 1.2: Results of PbSe QDs Synthesized with Different Oleic Acid Concentrations.

NC diameter [nm]	Oleic Acid [ml]	Peak maxima [nm]^{a}		K_{SV} [M^{-1}]
		Absorption	Emission	
2.5	3.6	853	1017	204
2.8	7.0	940	1084	108
2.9	8.5	955	1079	108
3.0	10	983	1110	45
3.2	12	1039	1240	44

$^{a)}$ In toluene and room temperature. For all synthesis, the specified volume of oleic acid was added at the injection temperature of 130°C. The NCs were held at the growth temperature of 120°C for 90 seconds before quenching with hexane.

1.2.2 Upconversion measurements

In this hybrid photon upconversion system, the upconversion quantum yield, Φ_{UC} is affected by three elementary processes (see equation 1):

$$\Phi_{\mathrm{UC}} = \Phi_{\mathrm{TET}}.\Phi_{\mathrm{TTA}}.\Phi_{\mathrm{RUB}} \quad (1)$$

where Φ_{TET} is the efficiency of TET between sensitizer and annihilator; Φ_{TTA} the efficiency of the TTA process; and Φ_{RUB} is the fluorescence quantum yield of the rubrene annihilator. In the measurements comparing the upconversion QY, the rubrene annihilator and NC sensitizer are kept at the same concentration, while the PbX NC sensitizers are varied in size. Therefore, we assume Φ_{TTA} and Φ_{RUB} remains constant and Φ_{UC} depends only on the difference inΦ_{TET}. Rubrene is a good annihilator because of its high fluorescence QY (Φ_{RUB} =0.98)[29] and annihilation efficiency (Φ_{TTA} ~0.33).[30]

The upconversion QY increases as particle size is decreased. Figure 2 shows the upconversion signal, or the emission of rubrene from the PbS/ rubrene (Figure 2a) and PbSe/ rubrene (Figure 2b) solutions. In this experiment, the rubrene and NC concentrations are kept constant at 2 mM and 10 µM respectively. Excitation is performed with an 808 nm cw NIR laser diode, while the emission of rubrene is normalized by the absorption of the NCs at this excitation wavelength. The relative upconversion QY of these samples versus the first excitonic peak, are plotted in Figure 2c. This relative QY is the ratio of the areas under the curves in Figure 2a and 2b to the area under the curve in Figure 2b for the 3.5 nm PbS/rubrene sample. By increasing the band gap from 1.19 eV to 1.45 eV, or decreasing the size of the PbSe NCs from 3.2 nm to 2.5 nm, the upconversion signal is enhanced about 250 times. For the PbS NCs, a change in size from 2.9 nm to 3.5 nm leads to an enhancement of about 700 times. When the relative upconversion QY is normalized by the PL QY of the NC, the same trend holds (Figure 2d). In this work, the maximum upconversion QY is about 0.01%.[12]

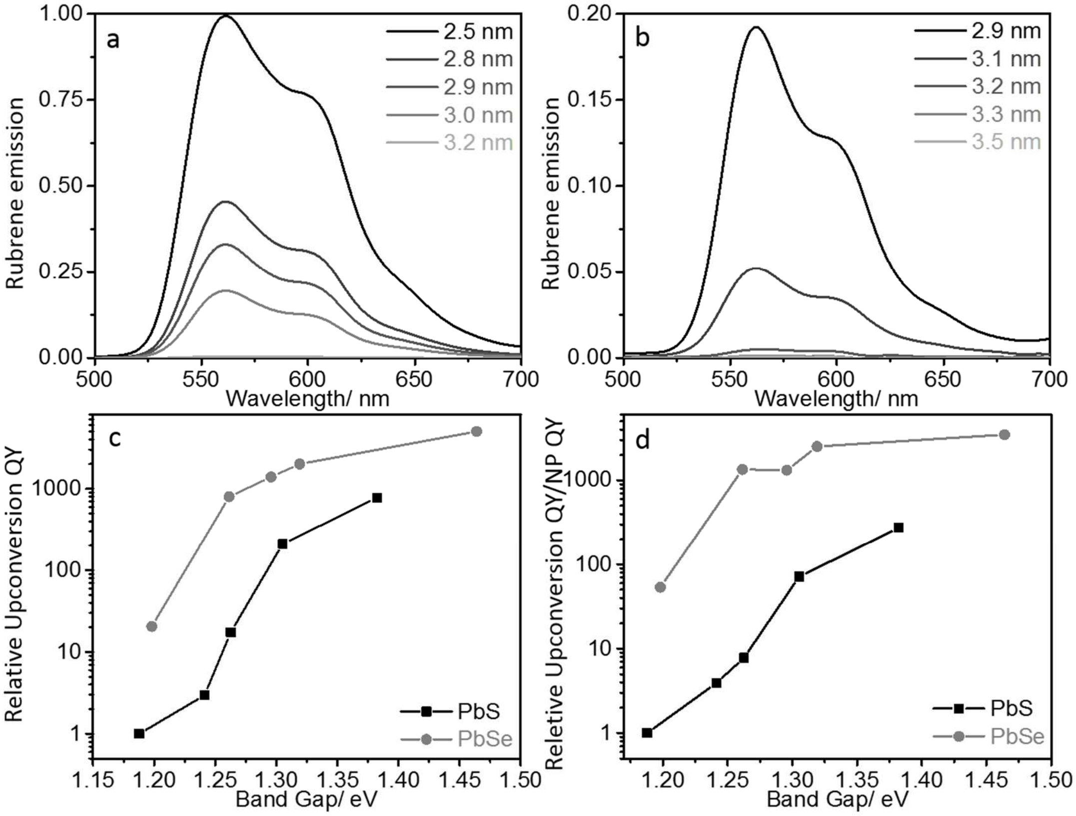

Figure 1.2. The effect of nanocrystal (NC) size on the upconversion of NIR light to visible light is shown. The upconverted emission from 2 mM rubrene mixed with 10 µM of (a) PbSe, and (b) PbS NCs excited with a 1230 W/cm^2 808 nm cw laser is plotted. (c) The relative upconversion QY of PbS and PbSe NCs with the first excitonic peak ranging from 1.19 to 1.45 eV is plotted for comparison. (d) The upconversion QY in (c) is normalized by the NC PL QY. All measurements were performed in toluene at RT.

Dexter energy transfer can be considered as the correlated transfer of two electrons.[31,32] For chalcogenide NCs, due to the band curvature, a decrease in particle size results in a shift of the conduction band, as opposed to the valance band.[33] This increase in band gap results in an increase in the driving force (ΔG) for energy transfer from NC donor to rubrene acceptor. As illustrated in Figure 1a, the driving force is the difference in the energy of the triplet state of the NCs and the lowest triplet excited state, T_1, of rubrene. The increase in upconversion QY, and by induction, the efficiency of TET as a function of the driving force indicates triplet sensitization is in the Marcus normal regime. According to Marcus theory,[34] an increase in driving force increases the rate of energy transfer, reaching a maximum when the driving force equals the reorganization energy. Using femtosecond transient absorption (TA) spectroscopy, Kamat et al. showed the rate of electron transfer from CdSe to TiO_2 NCs increases about 3 orders of magnitude with a decrease in the CdSe NC size from 7.5 to 2.4 nm.[35] Lian et al., also using TA, showed an increase in the electron transfer rate from CdS, CdSe, CdTe NC donors to the anthraquinone, methylviologen, and methylene blue acceptors as the NC diameter is decreased.[36] An Auger-assisted electron transfer model was used to explain the absence of a Marcus inverted regime. In a related hybrid NC-molecule upconversion platform, we have shown that 2.5 nm diameter CdSe NCs are better triplet sensitizers of diphenylanthracene compared to 5.1 nm diameter particles.[26] These smaller CdSe NCs give a photon upconversion QY of ~8 % compared to the ~0.3% for their larger counterparts. Unlike Tabachnyk et al.,[37] who report the resonant energy transfer of triplet excitons from pentacene to PbSe NCs, no resonance enhancement was seen here when the bandgaps of the PbX NCs approached the T_1 energy level (1.1 eV) of rubrene.

In addition to the changes in the driving force for energy transfer due to NC size, we consider how other factors such as exciton lifetime and geometry may play a role in this hybrid system. For example, an increase in exciton lifetime may increase the probability for energy transfer to rubrene. When the band gap of PbS NCs increase from 1.2 to 1.5 eV, the exciton lifetime increases 1.3 times from 2.5 to 3.4 μs[14], in tandem with an increase in PL QY. However, over this range of NCs, the upconversion quantum yield increases by 700 times. Thus we believe that the excitonic lifetime plays a secondary role to its energetics. In terms of particle geometry, the increased curvature of smaller NCs may result in a more disordered ligand shell. Alkyl ligands on the NC surface are flexible and can form gauche defects on the NC. Weiss et al.[38] and Benderskii et al.[39] probed the disorder in *n*-octylphosphonate and dodecanethiol ligands on CdSe NCs (radius =2 to 3 nm) and gold NCs (radius =0.9 to 11.5 nm) respectively by vibrational sum frequency generation. They demonstrated that as the NC size decreases, these linear, aliphatic, surface bound ligands are more disordered. This may allow rubrene to approach smaller NC at smaller distances and lead to more efficient energy transfer.

This enhancement of upconversion QY with decreasing the NC size is consistent with the pattern seen in NC-based solar cells.[40,41] Luther et al. showed that the open circuit voltage, V_{oc}, in a Schottky cell is enhanced by decreasing the NC size from around 7 to 3 nm.[40] Ma et al. also saw a similar trend in their V_{oc} when the PbSe NC size was decreased from 3.0 nm to 2.3 nm in a ITO/PEDOT/PbSe/Al photovoltaic cell.[2] Law et al have shown that smaller PbSe NCs have lower thin-film transistor mobility compared to larger NCs,[42] because of the larger number of interparticle hops between small NCs, and the possibility of localized trap states being deeper with respect to the band edges. The latter may explain why the upconversion QY measured for smaller NCs is less than expected considering the trajectory suggested by larger NCs (Figure 2c and d). Non-radiative recombination is attributed mainly to mid-gap states, trap states, and charged surfaces.[8,43,44,45,46] By decreasing the NC size, the trap states may play a more significant role because of increase in the dangling bonds and unpassivated surfaces, while the mid-gap states may become more accessible energetically. When comparing the PbS and PbSe NCs with the same first excitonic peak, PbSe NCs show a higher upconversion signal. This is consistent with previous work on thin film transistors based on PbX NCs, where PbSe NC thin films result in a device with higher mobility.[6,42] The larger Bohr radius of PbSe (44 nm) compared to PbS (18 nm) suggests that its excitonic wave function may extend further from the NC, promoting more efficient TET to rubrene, and therefore a higher upconversion QY.

1.2.3 PL quenching experiments (Stern-Volmer plots)

Stern-Volmer quenching experiments provide an alternative method of quantifying the efficiency of TET and its dependence on NC size. Here, the collisional quenching of the PL of PbSe NCs by TET to the rubrene acceptor is studied. From the Stern-Volmer equation (equation 2),

$$\frac{F_0}{F} = 1 + K_{SV}.[\text{rubrene}] \ (2)$$

F is the PL intensity of the NCs in the upconversion samples in the presence of rubrene, F_0 is the PL intensity of the NC in the absence of rubrene and K_{SV} is the dynamic Stern-Volmer quenching constant. Figure 3a shows the collisional Stern-Volmer plot of PbSe NCs generated from the change in NC PL as various amounts of rubrene were added to a fixed amount of PbSe NCs. The steady-state NC PL from a series of samples excited with 808 nm cw light was recorded, with the PbSe concentration fixed at 0.5 μM, and the rubrene concentration varied from 0.5-7.0 mM. In general, increasing the NC size (from 2.5 to 3.2 nm) leads to a lower K_{SV} (Figure 3b), and consequently lower TET efficiency, consistent with the results of the upconversion QY measurements. The highest K_{SV} value of 200 M^{-1} measured here for the 2.5 nm PbSe NCs is at least two orders of magnitude lower than the measured K_{SV} for triplet rubrene quenching other molecular sensitizers. The dynamic K_{SV} for a rubrene acceptor provided by transient lifetime measurements for the quenching of the texaphyrin (TXP) molecular sensitizer in dichloromethane at RT is 21000 M^{-1},[47] while that for Pyr_1RuPZn_2 porphyrin in acetonitrile/toluene is 3335 M^{-1}.[48]

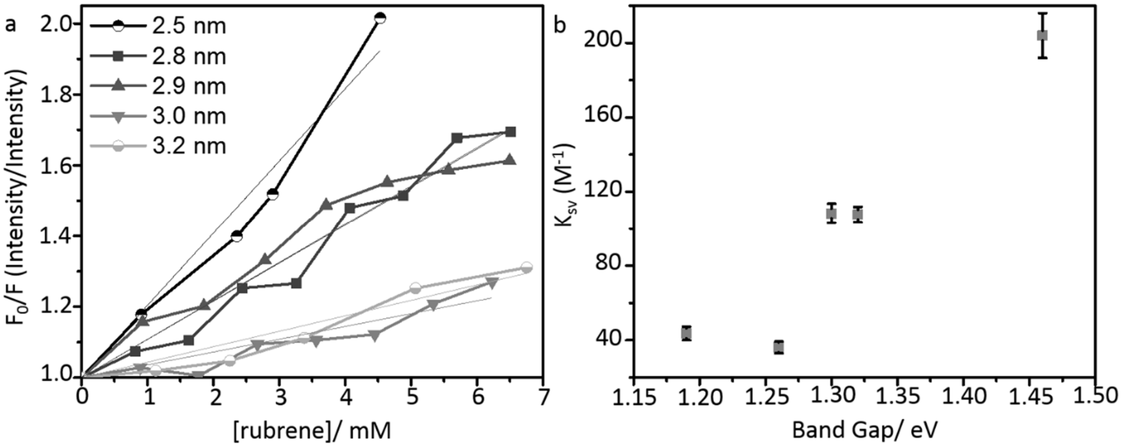

Figure 1.3. The steady-state energy transfer between PbSe nanocrystal (NC) donors of different size and a rubrene acceptor is studied with Stern-Volmer quenching experiments. (a) The change in NC photoluminescence (PL) when excited with a 1230 W/cm^2 808 nm cw laser diode is plotted against the concentration of rubrene. The lines represent the linear fit to the Stern-Volmer plot. (b) K_{SV} values (calculated from the slope of the linear fits in part (a) for 5 different sizes of PbSe NCs are plotted as the NC bandgap increases. All measurements were performed in toluene at RT. (See SI for calculations on errors in concentration and K_{SV}.)

From the range of K_{SV} values measured here, a bimolecular energy transfer quenching rate constant, k_q, of ~10^7 $M^{-1}s^{-1}$ can be calculated from the relationship $K_{SV} = \tau k_q$, where τ is the lifetime of the singlet excited state of the PbSe NC sensitizers in the absence of rubrene. PbSe NCs typically have a lifetime, τ ~ 1-2 μs.[21] The measured k_q is lower compared to the values obtained for rubrene as a triplet acceptor from TXP or from Pyr_1RuPZn_2, where quenching constants of 5.7×10^8 M^{-1} s^{-1} and 1.86×10^8 M^{-1} s^{-1} are reported respectively.[47,48] For the CdSe/9-anthracenecarboxylic acid sensitizer/transmitter hybrid system, k_q values ranging from 10^7 to 10^9 have been reported.[13,49] The fact that the

k_q here is lower is not surprising, since a transmitter ligand enhances the energy transfer between the NC and annihilator, and no transmitter ligand is used here. For example, functionalized tetracene derivatives bound on nanocrystal surfaces create an energy cascade between PbX and rubrene, efficiently directing energy transfer, resulting in an upconversion QY of 2%.[50] In terms of charge transfer, Knowles et al. observed a K_{SV} of 1200 M^{-1} for the quenching of PbSe NCs with benzoquinone (BQ) as an acceptor.[51] This larger K_{SV} was ascribed to the static binding of the BQ molecule on the NC surface. However in our system, considering the surface density of the native oleic acid ligands on PbSe nanocrystals obtained by nuclear magnetic resonance spectroscopy[52] (4.2 nm^{-2}) and the relatively bulky nature of rubrene, it is unlikely that rubrene can diffuse through the long chain oleic acid ligand shell. The insulating aliphatic ligands on the surface of the NCs hinder effective wave function overlap between the NC and rubrene because the efficiency of Dexter energy transfer decreases exponentially with distance. This problem can be addressed by replacing the long chain ligand with a shorter one, or ligand exchange with an appropriate transmitter ligand.[13,12,50]

1.3 Experimental section

1.3.1 Materials

Lead oxide (PbO, 99.999%), oleic acid (OA, tech. grade, 90%), and 1-octadecene (ODE, 90%), bis(trimethylsilyl) sulfide ($(TMS)_2S$) were purchased from Aldrich and used as received. Bis(trimethylsilyl) selenide ($(TMS)_2Se$) was acquired from Gelest Inc. HPLC grade hexane was purchased from Fisher Scientific. Dry ethanol was obtained from Sigma

Aldrich, while dry and degassed toluene was obtained from JC Meyer's solvent purification system.

1.3.2 PbS synthesis

PbS quantum dots were synthesized by modifying a protocol reported by Hines et al.[53] 5 different sizes (from 2.9 to 3.5 nm in diameter) were synthesized by tuning the reaction temperature from 77 to 120 °C (increasing the injection temperature leads to bigger NCs). A typical synthetic procedure for PbS quantum dots having the first excitonic peak of 1.30 eV is as follows: A mixture of PbO (0.45 g), oleic acid (2 ml), and 1-octadecene (ODE) (18 ml) were heated to 110 °C in a 50 ml three-neck flask under 100 millitorr vacuum for an hour during which Pb-oleate is formed, resulting in a clear colorless solution. Meanwhile, the sulfur precursor was prepared by mixing bis(trimethylsilyl)sulfide (0.21 ml) in anhydrous ODE (10 ml) in a glovebox with N_2 atmosphere. Then the reaction atmosphere was switched to Ar, and reaction temperature was set to 77 °C. The sulfur precursor was swiftly injected and the heater removed right after injection. The color of the solution turned from orange to brown in 3 seconds, and the reaction temperature dropped to about 67 °C. 2 minutes after injection, the reaction flask was rapidly cooled down to room temperature with compressed air and the injection of cold hexane (10 ml). As synthesized PbS NCs were quickly transferred air free to a glovebox and were washed 3 times by adding 1:1 volume hexanes/ethanol mixture, followed by centrifuging at 7000 rpm for 5 min. The supernatant was discarded. The final pellet was redispersed in toluene and stored in the dark in the glovebox for future use. The size and the concentration of PbS NCs were determined by measuring the energy of the first exciton peak and the absorption at 400 nm respectively.[54] For bigger NCs the reaction temperature set to higher temperature; for instance for the 3.5 nm PbS the reaction temperature set to 120 °C (see Table 1.)

1. 3.3 PbSe synthesis

PbSe quantum dots were synthesized via a modified protocol reported by Ma et al.[2] 5 different sizes of PbSe NCs (from 2.5 to 3.2 nm) were synthesized by varying the amount of oleic acid (from 3.6 to 12 ml) to the lead precursor. The injection temperature was set to 130°C. The synthesis method for the smallest NCs (2.5 nm) is as follows: A solution of PbO (223 mg, 1 mmol), oleic acid (3.55 ml, 2.5 mmol), and ODE (10 g) was degassed at 100 °C in a 50 ml three-neck flask for 1 h under vacuum. The solution was then heated for an additional 1 h to 150 °C under argon, resulting in a clear, colorless solution. The temperature was reduced to 130 °C. Then $(TMS)_2Se$ (62 µl, 0.25 mmol) in ODE (4 ml) was rapidly injected into the hot solution. Use caution and proper ventilation during this step, as toxic hydrogen selenide gas is also produced. Immediately after injection, the heater was turned off. After 105 seconds the reaction solution were cooled with compressed air and the injection of ethanol (10 ml) when the reaction cooled to 80 °C. The PbSe NCs were cleaned with the same procedure as the PbS NCs. Finally the NCs were stored in toluene in the dark inside the glovebox for future use. The size of the PbSe NCs was determined by measuring the first exciton peak of the absorption spectrum,[55] and the concentration was determined from the calculated size of the PbSe NCs and the absorption at 400 nm.[56] For bigger NCs, the volume of oleic acid was increased (see Table 2).

1. 3.4 Instrumentation

Absorption spectra was recorded on a Jasco-V670 UV-Vis absorption spectrophotometer. A 1230 W/cm^2 808 nm TO can cw elliptical laser diode (Thor Labs) with the largest and the smallest diameters of 0.12 and 0.06 mm respectively was used for excitation. For the upconversion and Stern-Volmer quenching experiments, the upconverted light and NC PL was collected from the front of the cuvette (at right angles from the excitation beam), with the laser focused to 1 mm from the side. This front corner excitation scheme limits the path length of the excitation and emission to 1 mm or less inside the cuvette, which minimizes attenuation of the excitation and reabsorption of the upconverted light. An Edmund Optics-FC10650836 dichroic mirror separated the upconversion signal from the NC PL. The NC PL was focused on an Ocean Optics QP400-2-VIS-NIR fiber with a 25.4 mm focal length N-BK7 plano-convex lens on a NIRS-0900-1700 Bayspec fluorometer. A PAF-SMA-11-A (Thor Labs) fiberport focused the upconversion signal on an Ocean Optics QP400-2-SR fiber connected to a JAZ spectrometer.

1. 3.5. Upconversion and Stern-Volmer quenching experiment sample preparation

The upconversion and Stern-Volmer quenching experiments were excited with the cw 808 nm laser diode described above. All the experiments were done in air tight 3.5 ml Starna cuvettes. For upconversion fluorescence measurements, we made solutions consisting of 2.0 mM rubrene and 10 μM PbS/PbSe NCs in toluene in a N_2 filled glovebox by adding a fixed volume from the stock solution of rubrene and different aliquots of

PbS/PbSe NCs in toluene. Toluene was added such that the resulting solutions had a 1 ml final volume.

For the Stern-Volmer quenching experiments, we made solutions with different concentrations of rubrene while keeping the concentration of PbSe NCs constant. This was done by adding different aliquots from the stock solution of rubrene to a fixed volume of NCs, and diluting with toluene such that the resulting solutions was 1 ml in volume. The final PbSe NC concentration was 0.5 μM while the final concentration of rubrene ranged from 0.5 to 7.0 mM. The Stern-Volmer plot (Figure 3a) was obtained by dividing the area under the PL spectra of PbSe NCs with specific rubrene concentrations to the corresponding area for PbSe NCs without rubrene.

1.4 Conclusion

In conclusion, quantitative Stern-Volmer analyses of the steady-state energy transfer from PbX NC donors to rubrene triplet state acceptors, coupled with the size-dependence of the efficiency of upconversion, reveals that TET occurs in the Marcus normal regime. With a decrease in NC size, the K_{SV} value and the upconversion quantum yield is enhanced. In addition, we see that given the same optical gap, PbSe NCs are better donors compared to PbS NCs for the triplet sensitization of rubrene. This work suggests that well passivated, small lead chalcogenide NCs will result in higher upconversion QYs. While this is helpful for the design of bright, hybrid upconversion-based probes for bioimaging, it suggests that different molecular acceptors should be paired with NC donors to match the driving force for energy transfer, for the efficient capture of the entire solar spectrum for catalysis, power conversion, or energy storage.

1.5 References

1. Alivisatos, A. P. *The Journal of Physical Chemistry* **1996,** *100*, 13226-13239.

2. Ma, W.; Swisher, S. L.; Ewers, T.; Engel, J.; Ferry, V. E.; Atwater, H. A.; Alivisatos, A. P. *ACS Nano* **2011,** *5*, 8140-8147.

3. Huynh, W. U.; Dittmer, J. J.; Alivisatos, A. P. *Science* **2002,** *295*, 2425-2427.

4. Caruge, J. M.; Halpert, J. E.; Wood, V.; Bulovic, V.; Bawendi, M. G. *Nature Photonics* **2008,** *2*, 247-250.

5. Colvin, V. L.; Schlamp, M. C.; Alivisatos, A. P. *Nature* **1994,** *370*, 354-357.

6. Talapin, D. V.; Murray, C. B. *Science* **2005,** *310*, 86-89.

7. Kovalenko, M. V.; Scheele, M.; Talapin, D. V. *Science* **2009,** *324*, 1417-1420.

8. Talapin, D. V.; Lee, J.-S.; Kovalenko, M. V.; Shevchenko, E. V. *Chemical Reviews* **2010,** *110*, 389-458.

9. Medintz, I. L.; Uyeda, H. T.; Goldman, E. R.; Mattoussi, H. *Nature Materials* **2005,** *4*, 435-446.

10. Schulze, T. F.; Schmidt, T. W. *Energy & Environmental Science* **2015,** *8*, 103-125.

11. Wang, H.-Q.; Batentschuk, M.; Osvet, A.; Pinna, L.; Brabec, C. J. *Advanced Materials* **2011,** *23*, 2675-2680.

12. Huang, Z.; Li, X.; Mahboub, M.; Hanson, K. M.; Nichols, V. M.; Le, H.; Tang, M. L.; Bardeen, C. J. *Nano Letters* **2015,** *15*, 5552-5557.

13. Mongin, C.; Garakyaraghi, S.; Razgoniaeva, N.; Zamkov, M.; Castellano, F. N. *Science* **2016,** *351*, 369-372.

14. Wu, M.; Congreve, D. N.; Wilson, M. W. B.; Jean, J.; Geva, N.; Welborn, M.; Van Voorhis, T.; Bulović, V.; Bawendi, M. G.; Baldo, M. A. *Nature Photonics* **2016,** *10*, 31-34.

15. Simon, Y. C.; Weder, C. *Journal of Materials Chemistry* **2012,** *22*, 20817-20830.

16. Schmidt, T. W.; Castellano, F. N. *The Journal of Physical Chemistry Letters* **2014,** *5*, 4062-4072.

17. Herkstroeter, W. G.; Merkel, P. B. *Journal of Photochemistry* **1981,** *16*, 331-341.

18. Zhang, L.; Leng, Y.; Zhang, J.; Hu, L. *Journal of Materials Science & Technology* **2010,** *26*, 921-924.

19. Wu, D. M.; García-Etxarri, A.; Salleo, A.; Dionne, J. A. *The Journal of Physical Chemistry Letters* **2014,** *5*, 4020-4031.

20. Englman, R.; Jortner, J. *Molecular Physics* **1970,** *18*, 145-164.

21. Wehrenberg, B. L.; Wang, C.; Guyot-Sionnest, P. *The Journal of Physical Chemistry B* **2002,** *106*, 10634-10640.

22. Ushakova, E. V.; Litvin, A. P.; Parfenov, P. S.; Fedorov, A. V.; Artemyev, M.; Prudnikau, A. V.; Rukhlenko, I. D.; Baranov, A. V. *ACS Nano* **2012,** *6*, 8913-8921.

23. Monguzzi, A.; Tubino, R.; Hoseinkhani, S.; Campione, M.; Meinardi, F. *Physical Chemistry Chemical Physics* **2012,** *14*, 4322-4332.

24. McGarry, K. A.; Xie, W.; Sutton, C.; Risko, C.; Wu, Y.; Young, V. G.; Brédas, J. L.; Frisbie, C. D.; Douglas, C. J. *Chemistry of Materials* **2013,** *25*, 2254-2263.

25. Hyun, B.-R.; Zhong, Y.-W.; Bartnik, A. C.; Sun, L.; Abruña, H. D.; Wise, F. W.; Goodreau, J. D.; Matthews, J. R.; Leslie, T. M.; Borrelli, N. F. *ACS Nano* **2008,** *2*, 2206-2212.

26. Huang, Z.; Li, X.; Yip, B. D.; Rubalcava, J. M.; Bardeen, C. J.; Tang, M. L. *Chemistry of Materials* **2015,** *27*, 7503-7507.

27. Abe, S.; Capek, R. K.; De Geyter, B.; Hens, Z. *ACS Nano* **2013,** *7*, 943-949.

28. Zhang, J.; Crisp, R. W.; Gao, J.; Kroupa, D. M.; Beard, M. C.; Luther, J. M. *The Journal of Physical Chemistry Letters* **2015,** *6*, 1830-1833.

29. Montalti, M.; Credi, A.; Prodi, L.;Gandolfi, M. T. In *Handbook of photochemistry, third edition*, CRC Press: **2006,** pp 83-351.

30. Cheng, Y. Y.; Khoury, T.; Clady, R. G. C. R.; Tayebjee, M. J. Y.; Ekins-Daukes, N. J.; Crossley, M. J.; Schmidt, T. W. *Physical Chemistry Chemical Physics* **2010,** *12*, 66-71.

31. Dexter, D. L. *The Journal of Chemical Physics* **1953,** *21*, 836-850.

32. Kohler, A.; Bassler, H. *Journal of Materials Chemistry* **2011,** *21*, 4003-4011.

33. Jasieniak, J.; Califano, M.; Watkins, S. E. *ACS Nano* **2011,** *5*, 5888-5902.

34. Marcus, R. A. *The Journal of Chemical Physics* **1965,** *43*, 679-701.

35. Robel, I.; Kuno, M.; Kamat, P. V. *Journal of the American Chemical Society* **2007,** *129*, 4136-4137.

36. Zhu, H.; Yang, Y.; Hyeon-Deuk, K.; Califano, M.; Song, N.; Wang, Y.; Zhang, W.; Prezhdo, O. V.; Lian, T. *Nano Letters* **2014,** *14*, 1263-1269.

37. Tabachnyk, M.; Ehrler, B.; Gélinas, S.; Böhm, M. L.; Walker, B. J.; Musselman, K. P.; Greenham, N. C.; Friend, R. H.; Rao, A. *Nature Materials* **2014,** *13*, 1033-1038.

38. Frederick, M. T.; Achtyl, J. L.; Knowles, K. E.; Weiss, E. A.; Geiger, F. M. *Journal of the American Chemical Society* **2011,** *133*, 7476-7481.

39. Weeraman, C.; Yatawara, A. K.; Bordenyuk, A. N.; Benderskii, A. V. *Journal of the American Chemical Society* **2006,** *128*, 14244-14245.

40. Luther, J. M.; Law, M.; Beard, M. C.; Song, Q.; Reese, M. O.; Ellingson, R. J.; Nozik, A. J. *Nano Letters* **2008,** *8*, 3488-3492.

41. Gao, J.; Luther, J. M.; Semonin, O. E.; Ellingson, R. J.; Nozik, A. J.; Beard, M. C. *Nano Letters* **2011,** *11*, 1002-1008.

42. Liu, Y.; Gibbs, M.; Puthussery, J.; Gaik, S.; Ihly, R.; Hillhouse, H. W.; Law, M. *Nano Letters* **2010,** *10*, 1960-1969.

43. Argeri, M.; Fraccarollo, A.; Grassi, F.; Marchese, L.; Cossi, M. *The Journal of Physical Chemistry C* **2011,** *115*, 11382-11389.

44. Ip, A. H.; Thon, S. M.; Hoogland, S.; Voznyy, O.; Zhitomirsky, D.; Debnath, R.; Levina, L.; Rollny, L. R.; Carey, G. H.; Fischer, A.; Kemp, K. W.; Kramer, I. J.; Ning, Z.; Labelle, A. J.; Chou, K. W.; Amassian, A.; Sargent, E. H. *Nat Nano* **2012,** *7*, 577-582.

45. Cossairt, B. M.; Juhas, P.; Billinge, S. J. L.; Owen, J. S. *The Journal of Physical Chemistry Letters* **2011,** *2*, 3075-3080.

46. Voznyy, O.; Zhitomirsky, D.; Stadler, P.; Ning, Z.; Hoogland, S.; Sargent, E. H. *ACS Nano* **2012,** *6*, 8448-8455.

47. Deng, F.; Sun, W.; Castellano, F. N. *Photochemical & Photobiological Sciences* **2014,** *13*, 813-819.

48. Olivier, J.-H.; Bai, Y.; Uh, H.; Yoo, H.; Therien, M. J.; Castellano, F. N. *The Journal of Physical Chemistry A* **2015,** *119*, 5642-5649.

49. Piland, G. B.; Huang, Z.; Lee Tang, M.; Bardeen, C. J. *The Journal of Physical Chemistry C* **2016,** *120*, 5883-5889.

50. Huang, Z.; Simpson, D. E.; Mahboub, M.; Li, X.; Tang, M. L. *Chemical Science* **2016**, **7**, 4101-4104

51. Knowles, K. E.; Malicki, M.; Weiss, E. A. *Journal of the American Chemical Society* **2012,** *134*, 12470-12473.

52. Moreels, I.; Fritzinger, B.; Martins, J. C.; Hens, Z. *Journal of the American Chemical Society* **2008,** *130*, 15081-15086.

53. Hines, M. A.; Scholes, G. D. *Advanced Materials* **2003,** *15*, 1844-1849.

54. Moreels, I.; Lambert, K.; Smeets, D.; De Muynck, D.; Nollet, T.; Martins, J. C.; Vanhaecke, F.; Vantomme, A.; Delerue, C.; Allan, G.; Hens, Z. *ACS Nano* **2009,** *3*, 3023-3030.

55. Dai, Q.; Wang, Y.; Li, X.; Zhang, Y.; Pellegrino, D. J.; Zhao, M.; Zou, B.; Seo, J.; Wang, Y.; Yu, W. W. *ACS Nano* **2009,** *3*, 1518-1524.

56. Moreels, I.; Lambert, K.; De Muynck, D.; Vanhaecke, F.; Poelman, D.; Martins, J. C.; Allan, G.; Hens, Z. *Chemistry of Materials* **2007,** *19*, 6101-6106.

Chapter 2 Efficient infrared-to-visible upconversion with sub-solar irradiance

2.1 Introduction

Organic semiconductors and inorganic semiconductor NCs are keenly explored as candidate materials for TGPV,[1] since both offer the possibility of raising the PCE by taking advantage of multi-excitonic processes that can spectrally reconfigure the solar spectrum, e.g. MEG[2-6] or singlet fission.[7-9] In addition, both classes of materials lend themselves to cheap, roll-to-roll processing techniques. Here, we present a hybrid nanostructure for the efficient upconversion of NIR to visible photons based on triplet-triplet annihilation (TTA). Compared to the lanthanide-based upconversion systems [10-13] and other multi-photon absorption processes, [14-15] TTA-based upconversion[16-22] is the only demonstrated method for harvesting energy from the sun. Despite efforts to design small molecules or conjugated polymers that harvest infrared photons, it remains difficult to find organic structures that absorb strongly at wavelengths to the red of 750 nm. In addition to lower photostability, organic chromophores that absorb strongly in the NIR undergo rapid internal conversion to the ground state.[23] In this work, the large extinction coefficients and tunable bandgaps of semiconductor NCs from the visible to the NIR make them ideal for capturing the 53% of the solar flux in the NIR region from 700 to 2500 nm. In particular, we have shown that PbS and PbSe NCs with absorption maxima at 1044 nm can be utilized as sensitizers in this hybrid upconversion platform. Baldo and co-workers[24] have demonstrated that PbS/ rubrene thin films can upconvert cw NIR irradiation exceeding 1 μm in wavelength to produce yellow light centered at 560 nm.

2.2 Results and discussion

The hybrid upconversion platform here consists of PbS-CdS core-shell NCs, 5-carboxylic tetracene (5-CT),[25] and rubrene that serve as the sensitizer, transmitter, and annihilator respectively. The high fluorescence QY (98%) of rubrene[26] is critical for its role as annihilator, while the low-lying, long-lived triplet state of 5-CT mediates the energy transfer from NCs to rubrene with the formation of an energy cascade. Fig. 1a shows the energy transfer from PbS-CdS core-shell NCs to the first triplet state of 5-CT and then rubrene. Once this process is repeated and a pool of rubrene triplets form, two rubrenes in their triplet excited state can interact and produce one in its ground state, S_o, and the other in its first excited singlet state, S_1. This spin-allowed process (termed TTA) results in the emission of one high energy photon at the wavelength of ~560 nm from the absorption of two NIR photons by the NC. The absorption and emission spectra of PbS-CdS core-shell NCs, 5-CT, and rubrene are shown in Fig. 1b.

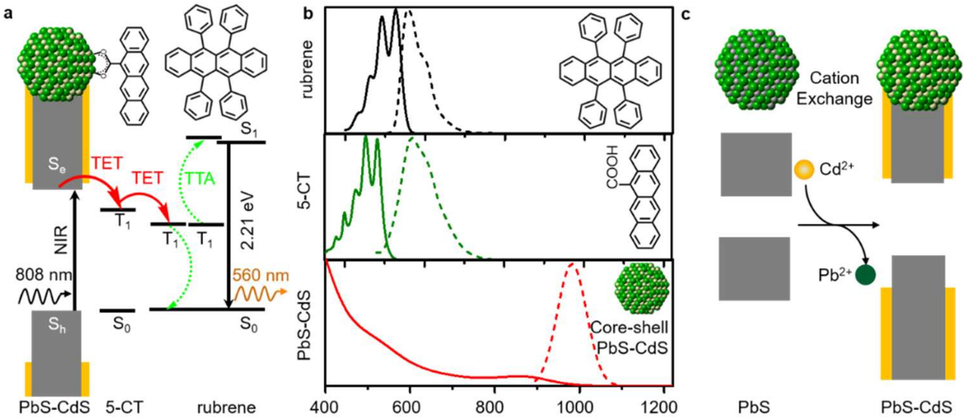

Figure 2.1. PbS-CdS core-shell nanocrystals (NCs), 5-carboxylic tetracene (5-CT), and rubrene serve as the sensitizer, transmitter, and annihilator respectively in this hybrid upconversion platform. a, Schematic of the energy transfer. The PbS-CdS core-shell NCs absorb the near-infrared photons. 5-CT is the transmitter ligand bound to the surface of the NCs that mediates triplet energy transfer (TET) from the NC to the rubrene emitter. Rubrene then undergoes triplet-triplet annihilation (TTA) to upconvert light, producing high-energy photons in the visible. b, The absorption (solid line) and emission (dashed line) spectra of rubrene (black/ top), 5-CT (green/ middle),and PbS-CdS core-shell NCs (red/ bottom) with 2.7 nm PbS core diameter and 0.24 nm CdS shell thickness in toluene at room temperature. c, Schematic of the cation exchange reaction for the synthesis of PbS-CdS core-shell NCs.

PbS-CdS core-shell NCs were synthesized by cation exchange (Fig. 1c). While PbS-CdS core-shell NCs with thick CdS shells have been described as having a quasi-type II energy structure, with the electron delocalized over the entire NC and the hole localized within the core, [27-28] the PbS-CdS core-shell NCs here have relatively thin shells on the order of a monolayer. We chose a CdS shell because Cd^{2+} has an ionic radius similar to Pb^{2+} resulting in a small lattice mismatch (1.7%) with PbS. Also, the CdS shell passivates the trap states on the PbS core, as seen by the enhanced photoluminescence QYs here (Fig. S1) and elsewhere, [29] which translate into improved efficiency and stability in devices like photodetectors and solar cells. [30-31] The CdS shell has also been reported to stabilize the PbS core in aqueous and glassy environments. [32] In terms of core-shell NC synthesis, PbS

NCs cores were injected into the solution of cadmium acetate in oleic acid and 1-octadecene at 90 ˚C. The original lead ions in the PbS NCs were partially replaced by cadmium during cation exchange while the anionic framework is preserved. The resultant PbS core size was determined from its excitonic peak using the empirical formula developed by Moreels et al. [33] Applying a CdS shell on PbS NCs can significantly improve the upconversion QY. Shell thickness increased with the Cd^{2+} to Pb^{2+} molar ratio and reaction time, resulting in a blue shift in NC emission and absorption spectrum (Fig. 2a).

The effect of this CdS shell on the efficiency of triplet transfer from PbS NC donor to rubrene acceptor was examined in the absence of a transmitter ligand. Initially, as the CdS shell thickness is increased, the upconversion QY improves (Fig. 2b). This enhancement is due to the passivation of trap states and decrease in NC core size. In our previous work, we have shown that a decrease in NC size increases the upconversion QY due to an increase in the driving force for energy transfer from NCs to annihilator. [34-36] The CdS shell passivates the surface traps and consequently decreases nonradiative recombination.[31] In NCs, trap states consist of dangling bonds and charge imbalances arising from non-stoichiometric compositions. Watt et al[31] and Loi et al[36] have independently shown that a sub-monolayer CdS shell can improve the PCE in Schottky solar cells made of PbS-CdS core-shell NCs.

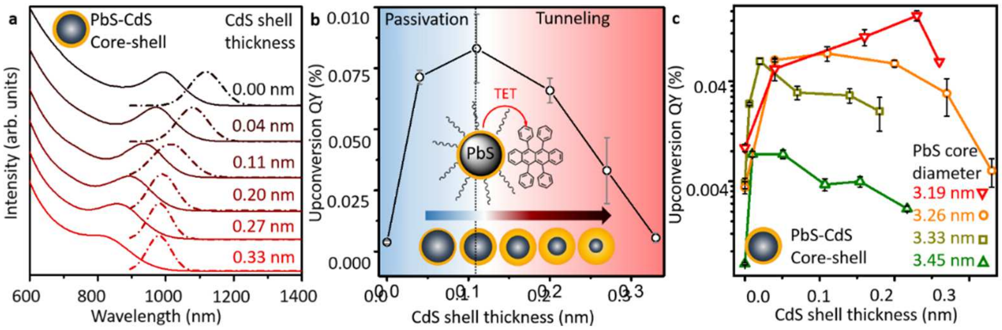

Figure 2.2. Applying a CdS shell on PbS nanocrystals (NCs) can significantly improve the upconversion QY. a, The absorption (solid line) and emission spectrum (dashed-dot line) of PbS-CdS core-shell NCs arising from 3.26 nm diameter PbS NC cores synthesized via cation exchange. The PbS core contracts as CdS shell thickness increases, as indicated by the blue shift in the absorption and emission spectra. b, In the presence of a rubrene annihilator, the upconversion quantum yield (QY) of the core-shell NCs shown in Fig. 2a, rises then fall as CdS shell thickness is increased. The rise is due to NC surface passivation, while the fall is due to the introduction of a large tunneling barrier. c, The upconversion QY of four different sets of PbS-CdS core-shells NCs originating from different PbS cores with diameters of 3.19 nm (red triangle), 3.26 nm (orange circle), 3.33 nm (green square), and 3.45 nm (green triangle). All samples were excited with 22 W/cm^2 808 nm laser diode in toluene at RT. In b and c, the rubrene concentration is 20 mM, and optical density of the NCs at the excitation wavelength was 0.002.

A further increase in CdS shell thickness decreases the upconversion QY. This is mainly because the CdS shell acts as a barrier for efficient wave-function overlap between the PbS core and rubrene. This reduces the efficiency of energy transfer, leading to a lower upconversion QY. The upconversion QY of all samples were measured by front-phase geometry in a 100 µM path length capillary tube (see supplementary information) to minimize any parasitic reabsorption. We calculated the upconversion QY from the following equation:

$$\Phi_{\mathrm{UC}} = 2\Phi_{\mathrm{rub}} \times \frac{\text{(photons absorbed by reference)}}{\text{(photons absorbed by sample)}} \times \frac{\text{(photons emitted by sample)}}{\text{(photons emitted by reference)}} \quad (1)$$

where Φ_{UC} is the upconversion QY, Φ_{Rub} is the fluorescence QY of rubrene and is 0.98.[26]

This general trend where upconversion QY is initially enhanced then diminished with increasing CdS shell thickness is universal. Fig. 2c shows the upconversion QY of four sets of core-shell NCs when mixed with rubrene for five different CdS shell thicknesses. The emission and absorption spectrum of all PbS-CdS NCs are shown in Fig. S2. For each family of PbS-CdS core-shell NCs, we repeated the upconversion QY measurements at least twice and the results are in good agreement. Interestingly, as the initial PbS core size decreases, the upconversion QY maximizes at a thicker CdS shell. This shows a thicker CdS layer is required for passivating the trap states of smaller NCs, consistent with the hypothesis that smaller NCs have a higher density of trap states compared to larger ones due to increased strain from the higher surface area to volume ratio.[37]

We examined a series of PbS-CdS core-shell NCs with identical first excitonic energy levels to determine the mechanism of energy transfer. For Förster energy transfer, the rate of energy transfer, k_{et}, is inversely proportional to the sixth power of the donor and acceptor (D-A) distance, d, while for Dexter energy transfer, k_{et} decays exponentially with d:[38]

$$k_{et} = k_0 \exp(-\beta d) \quad (2)$$

where d can be considered the CdS shell thickness. β is the damping coefficient. To investigate this distance dependence, we synthesized three PbS-CdS core-shell NCs with different shell thicknesses such that the distance between the PbS NC core and rubrene (i.e. donor and acceptor, D-A) is well defined. Fig. 3a shows the emission and absorption spectra of these NCs. These core-shell NCs have the same core size, as indicated by their approximately identical absorption maxima, which implies a similar driving force for energy transfer to rubrene. Equation (3) shows that the upconversion QY is a convolution of many factors:[39]

$$\Phi_{UC}=\Phi_{TET}.\Phi_{TTA}.\Phi_{Rub} \quad (3)$$

where Φ_{UC} is the upconversion QY, and Φ_{TET} is the efficiency of energy transfer, Φ_{TTA} is the efficiency of TTA, and Φ_{Rub} is the fluorescence quantum yield of rubrene. $\Phi_{Rub}=0.98$[26] and $\Phi_{TTA}=0.33$[40]. The triplet-triplet energy transfer efficiency (TTET) from 5-CT to rubrene is 1 due to the high concentration of rubrene (20 mM). At this high concentration, TTET is limited by spin considerations rather than diffusion. [39] This is because 5-CT and rubrene collide in nanoseconds, well within the triplet lifetime of 5-CT (on the order of ms.)[26] As a result, energy successfully transfers from 5-CT to rubrene before the 5-CT triplet decays. In this experiment, since the rubrene annihilator and core-shell NCs sensitizers are kept at the same concentration, we can assume that Φ_{UC} has a linear relation with Φ_{TET}.

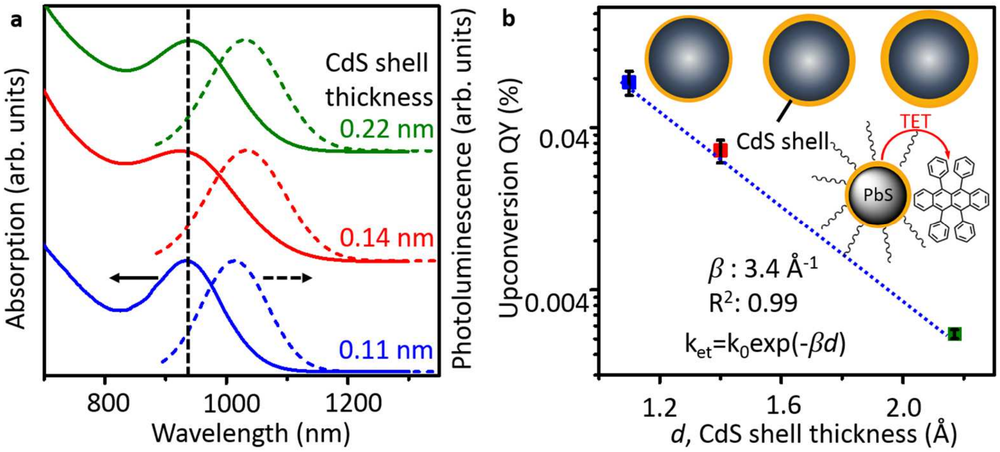

Figure 2.3. The Dexter process dominates in triplet energy transfer (TET) from PbS-CdS core-shell nanocrystal (NC) sensitizers to rubrene annihilators. a, The absorption (solid line) and emission spectrum (dashed-dot line) of PbS-CdS core-shell NCs possessing the same 3.0 nm core diameter (i.e. the same absorption maxima) and consequently the same driving force for energy transfer to rubrene. b, The dependence of upconversion quantum yield (QY) of the NCs shown in Fig. 3a on CdS shell thickness is plotted. All samples were excited by 22 W/cm^2 808 nm laser diode. The exponential decrease of upconversion QY with increasing shell thickness is consistent with Dexter energy transfer with a damping coefficient, β, of 3.4± 0.1 Å^{-1}. All spectra were taken in toluene at room temperature.

The Dexter process dominates in TET from PbS-CdS core-shell NC to rubrene annihilator, and the damping coefficient, β, across a CdS tunneling barrier from a PbS donor to rubrene acceptor can be calculated from Fig. 3b, where the upconversion QY as a function of CdS shell thickness is shown. We can assume Φ_{TET} is linearly related to k_{et} (see supplementary information). Fig. 3b shows that Φ_{TET} decreases exponentially as donor-acceptor distance increases. The empirical damping coefficient, β, is fitted to be 3.4 ± 0.1 Å^{-1} (Equation (2)). This is higher than the β value of 0.43 ± 0.07 Å^{-1} for a CdSe donor to a diphenylanthracene acceptor across a phenyl tunneling barrier.[41] This is the first time a β value is reported for an inorganic shell on semiconductor NCs. β depends on the barrier height and energy offset between donor and acceptor.[42] Here, the energy offset between first triplet state of rubrene and the NC bandgap is 0.36 eV. Consequently, the larger β value here indicates a higher tunneling barrier, perhaps because the PbS-CdS core-shell forms a Type I heterostructure where the band offsets in bulk differ by ~2.0 eV as compared to the energy difference between the CdSe donor and phenyl barriers (<1.0 eV).

5-CT serves to transmit triplets from the NC donor to the rubrene acceptor down an energy gradient, as shown in Fig. 1a. Acenes with appropriate energy levels within the NC bandgap can accept triplet excitons originating from the NC. This TET is particularly effective when the transmitter is bound to the NC surface, e.g. e related tetracene derivative, 4-(tetracen-5-yl)benzoic acid (CPT) can completely quench NC PL while enhancing the upconversion QY. We and other groups have utilized a similar energy cascade using CdSe NCs, 9-anthracene carboxylic acid, and diphenylanthracene as the sensitizer, transmitter, and annihilator respectively for the conversion of green to violet light.

The presence of a bound transmitter, 5-CT, enhances the upconversion QY up to 37 fold to a maximum of 8.4 ± 1.0 %. As the sensitizer, we chose the PbS-CdS core-shell NCs that showed the highest upconversion QY before the addition of a transmitter (λ_{max} = 850 nm; 0.24 nm CdS shell, Fig. 2c). Ligand exchange was performed in a mixture of tetrahydrofuran and toluene (see supplementary information). Successful incorporation of 5-CT on the surface of the core-shell NCs is indicated by a 7 nm red shift in the molecular absorption spectrum (Fig. S3), suggesting a change in its dielectric environment. A 22 W/cm^2 cw 808 nm laser diode was used in the presence of 20 mM rubrene, and the upconversion QY was optimized by varying the concentration of 5-CT during ligand exchange (Fig. 4a). As the concentration of 5-CT increases, the upconversion QY maximized with 60 bound 5-CT ligands per NC. The number of bound tetracene transmitter ligands increases with its concentration during ligand exchange, as indicated by the UV-Vis electronic absorption spectrum of isolated NC-transmitter complexes (see supplementary information). As observed before, a further increase in the number of bound ligands beyond 60 results in lower upconversion QYs.[43] This might be due to TTA occurring between neighboring 5-CT ligands at high transmitter density, and subsequent reabsorption of the upconverted light by the NC. Here, the optimized density of NC-surface bound transmitter ligands is 1.9 nm^{-2}, higher than the 1.2 nm^{-2} measured on 2.9 nm diameter PbS NC sensitizers.[43] This discrepancy could be due to the presence of the CdS shell here, since oleic acid is the native ligand in both cases. It could also be related to the molecular footprint, since the 5-CT ligand here is more compact than the CPT transmitter used previously.[43]

This hybrid system upconverts NIR to visible light even at sub-solar fluxes, as shown in power dependence measurements. Fig. 4b shows the log-log plot of the upconverted visible light vs. excitation density of a cw 808 nm laser diode. The slope of this plot changes from 2 (quadratic dependence) to 1 (linear dependence) as the excitation density increases. A quadratic dependence indicates that triplets decay primarily by first-order loss processes. However at higher excitation density, the triplet concentration is sufficiently high and as a result the TTA process is dominant. This threshold excitation density acquires significant importance because it determines the relevance of this upconversion system for practical applications, e.g. photovoltaics. Above an excitation density threshold of 3.2 mW/cm^2, this hybrid upconversion platform enters the linear regime, where the upconversion QY is constant at 8.4 ± 1.0 %. Considering the wavelength (808 nm) of the excitation beam, this excitation power corresponds to a photon flux of 1.3×10^{16} $s^{-1}cm^{-2}$. This is three times lower than the available solar photon flux in the AM1.5 spectrum from 750 to 850 nm (the absorption tail of the PbS-CdS core-shell NCs) of 4.1×10^{16} $s^{-1}cm^{-2}$ (see supplementary information). To the best of our knowledge, this is the first demonstration of an upconversion system that can operate with high upconversion QY at sub-solar fluxes. This threshold of 3.2 mW/cm^2 is at least 5 orders of magnitude lower compared to the best performing lanthanide based upconversion systems, e.g. bulk $NaYF_4$: Er^{3+} 2%, Yb^{3+} 20% (20 W/cm^{-2} at 980 nm for 3% upconversion QY)[44], or Gd_2O_2S: 10% Er^{3+} (700 W/cm^{-2} for 12 ± 1% under monochromatic excitation around 1500 nm).[45] For a related hybrid upconversion system, Baldo et al.[24] reported a minimum excitation density of 12 W/cm^{-2} for an upconversion QY of 1.2 ± 0.2% using PbS NC sensitizers and dibenzotetraphenylperiflanthene doped rubrene. Considering that the TTA efficiency, ϕ_{TTA}, and the fluorescence QY of rubrene, ϕ_{RUB}, are 33% and 98% respectively, the maximum achievable upconversion QY for this system is around 32.3%. (see Equation (3)). As such, there is room for improving the upconversion QY, especially since NC photoluminescence is still observed under the conditions used in Fig. 4.

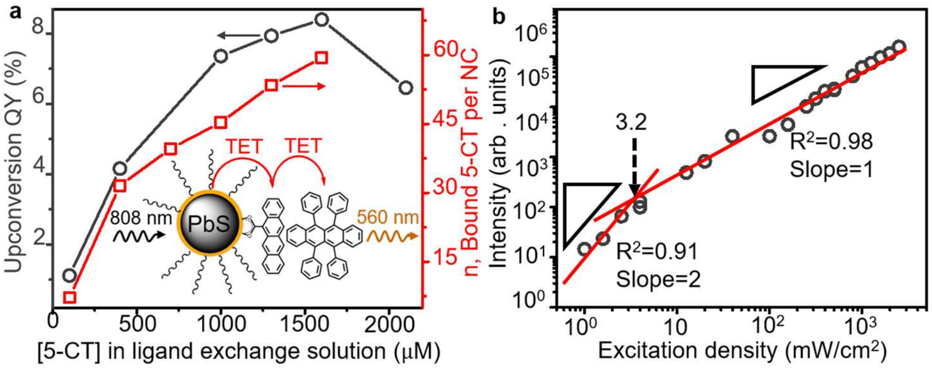

Figure 2.4. The upconversion quantum yield (QY) of tetracene functionalized PbS-CdS core-shell nanocrystals (NCs) reach 8.4 ± 1.0 % at sub-solar excitation power densities. a, Evolution of the upnconversion QY and number of covalently bound 5-carboxylic tetracene (5-CT) ligand on PbS-CdS core-shell nanocrystals (NCs) as the concentration of the 5-CT in the ligand exchange solution increases. b, Log−log plot of the upconversion signal versus excitation power density when the ligand loading is 60 per NC, showing the transition from the quadratic (slope = 2) to the linear (slope = 1) regime. For all measurements, PbS-CdS core-shell NCs with an absorption maxima of 850 nm and CdS shell thickness of 0.24 nm were excited with an 808 nm laser diode in toluene at RT. The native long chain aliphatic oleic acid ligands were partially replaced with the 5-CT transmitter ligand. The concentration of nanocrystals is 10 μM in the ligand exchange solution, and the concentration of rubrene is 20 mM in the upconversion experiments.

2.3 Experimental section

2.3.1 Materials

Lead oxide (PbO, 99.999%), oleic acid (OA, tech. grade, 90%), and 1-octadecene (ODE, 90%), bis(trimethylsilyl) sulphide ($(TMS)_2S$), cadmium acetate hydrate ($Cd(OAc)_2$, 99.99%) were purchased from Aldrich and used as received. HPLC grade hexane was obtained from Fisher Scientific. Dry ethanol and methanol was purchased from Sigma Aldrich, while dry and degassed toluene, acetone, and tetrahydrofuran were obtained from JC Meyer's solvent purification system.

2.3.2 PbS-CdS core-shell nanocrystal (NC) synthesis

Four PbS NCs of different sizes were synthesized following our previous work.[34]

PbS-CdS core-shell NCs were synthesized following Watt et al.[31] First a cadmium-oleate solution was made by dissolving 30 mg $Cd(OAc)_2$ in 88.7 µl of OA and 347.9 µl of ODE at 120 °C until a clear solution forms. For different CdS shell thicknesses, the desired volume of Cd precursor was transferred into 4 ml vials. Then 277 µl of 30 mg/ml of PbS core solution were injected to the Cd-oleate solution while stirring at 90 °C. Right after injection, the temperature were set to 80 °C. After the desired reaction time, 0.416 µl of hexane was injected to quench the reaction. The aliquots and reaction times employed are listed in Table S1 and S2. The NCs were washed once with the addition of acetone and 3 times with methanol, followed by centrifuging at 7800 rpm for 5 min. After each cleaning, the NC pellet was dissolved in 400 µl hexane. Finally the NCs were dissolved in toluene and stored in the glovebox in the dark. Fig. S2 (see supplementary information) indicates the photoluminescence (PL) and emission spectrum of PbS-CdS core-shell NCs with various shell thickness arising from 3 different PbS core sizes of 3.19, 3.33, and 3.45 nm in diameter, while the core-shell NCs for the 3.26 nm PbS core are shown in Fig. 2.

The amount of $Cd(OAC)_2$ required was calculated based on the NCs size and desired CdS shell thickness from following equation:

$$\frac{\text{mole}_{\text{Pb}}}{\text{mole}_{\text{Cd}}}=\frac{\frac{4}{3}\Pi r^3\rho_{\text{PbS}}M_{\text{CdS}}}{\frac{4}{3}\Pi(R^3\text{-}r^3)\rho_{\text{CdS}}M_{\text{PbS}}} \tag{1}$$

here R is the radius of PbS-CdS core-shell NCs; r is the radius of PbS core. ρ_{PbS} and ρ_{CdS} are the density of bulk PbS and CdS respectively (g.cm^{-3}), M_{PbS} and M_{CdS} are the molecular weights of PbS and CdS respectively (g.mol^{-1}). Table S1 and S2 in supplementary information represent the volume of the added Cd-oleate solution and desired reaction times for synthesizing different CdS shells from four different sizes of parent PbS NCs.

The CdS shell thickness was determined by subtracting the parent PbS NC radius from the PbS core radius after cation exchange assuming the overall NC size remains constant. This assumes that the PbS-CdS core-shell NCs used in this study have an extremely thin shell on the order of a monolayer of zinc blende CdS (0.25 nm). However, the actual CdS shell is likely thicker for several reasons: First, Moreels's empirical data is based on the assumption that PbS NCs are perfectly spherical. Second, the PbS core has a common shared outer layer of sulfur atoms with the CdS shell. Finally, when comparing the PbS NCs of the same size as the core of PbS-CdS core-shell NCs, the core-shell is less quantum confined resulting in a partial red shift that results in an under-estimation of the CdS shell.

2.3.3 Instrumentation

Absorption spectra was recorded on a Jasco-V670 UV–Vis absorption spectrophotometer. A 22 W/cm^{-2} 808 nm TO can cw elliptical laser diode (Thor Labs) with the largest and the smallest diameters of 0.64 and 0.32 mm respectively was used for excitation of the upconversion and photoluminescence (PL) samples. Rubrene reference samples were excited with 12 W/cm^{2} 532 nm Coherent Sapphire laser.

The upconverted light and NC PL was collected from the front of the cuvette (at a 70° angle from the excitation beam). A 100 μm thick capillary tube (LRT-010-2-10 Friedrich & Dimmock, Inc.) was used to hold the sample inside an air-free cuvette. This front phase collection scheme and 100 uM capillary tube attenuates the parasitic reabsorption of the upconverted light. A 790 nm short-pass filter (FF01-790/SP-25 BrightLine® multiphoton) and 532 nm notch filter (NF01-532U-25 Semrock) were used to block the excitation beams. A lens with a focal length of 30 mm was used to couple the signal from upconversion sample into a PAF-SMA-11-A (Thor Labs) fiberport through an Ocean Optics QP400-2-SR fiber connected to a JAZ spectrometer.

NC PL were detected using the same setup as the upconversion measurement, but we removed the 790 nm short pass filter and 532 notch filter, and an Ocean Optics QP400-2-VIS-NIR fiber was used to funnel the PL signal to a BaySpec NIR spectrometer. 3.5 ml air-free, quartz Starna cuvettes were used to measure the PL. Power dependence measurements were carried out using the same setup as the upconversion experiments with a 300 μm diameter pinhole placed right after the laser diode resulting in a spherical beam with diameter of 0.23 mm. The incident power was varied with neutral density (ND) filters. The incident power was measured with a calibrated detector (Newport 918D-ST-SL wand detector) and power meter (Newport 2936-R), or calculated based on the ND filter.

2.3.4 Upconversion sample preparation

Following our previous work[43] we placed the samples for upconversion in 100 μm thick borosilicate capillary tubes inside 3.5 ml Starna cuvettes. All upconversion experiments were strictly air free.

2.3.5 Oleic acid capped PbS-CdS core-shell NCs upconversion sample preparation

3 μmol PbS-CdS core-shell NCs were dried by evaporation inside the glovebox. Then 300 μl of 20 mM rubrene was added, resulting in a final concentration of 10 μM in terms of NCs. 100 μl of this solution was used for upconversion QY measurements and the rest was used for UV-Vis-NIR absorption, as shown in Fig. 2 and 3.

2.3.6 5-CT functionalized PbS-CdS core-shell NCs upconversion sample preparation

5-CT were synthesized following the work of Okamoto et al.[25] 5 mM of 5-CT in 10:1 THF to toluene (v:v) was made. An aliquot of this solution of 5-CT and 300 μl of 10 μM PbS-CdS core-shell NCs in toluene were mixed where the 5-CT concentration varied from 100 to 1600 μM. After stirring for 45 min, 1.2 ml of methanol was added and the NCs were crashed out by spinning at 7800 rpm for 5 min. The supernatant was discarded and the pellet was dried in the glovebox under vacuum. Then 300 μl of 20 mM rubrene was added to the pellet to redisperse the NCs. 100 μl of this solution were used for upconversion QY measurement and the rest was used to acquire the UV-Vis-NIR absorption. We repeated this ligand exchange procedure on three different batches of PbS-CdS core-shell NCs (λ_{max} = 850 nm; 0.24 nm CdS shell), two of which were made from different batches of λ_{max} = 974 nm PbS core NCs. For all samples, both the trend and the actual number of bound 5-CT transmitter ligands and resultant upconversion QY were in great agreement.

2.4 Conclusion

In conclusion, this is the first demonstration that the efficient conversion of NIR to visible light can occur at sub-solar excitation densities. By enhancing the energy transfer between sensitizer and annihilator, this work provides a clear direction towards maximizing the upconversion QY in hybrid systems. Here, it is achieved by engineering both the inorganic and organic components, where a CdS shell passivates the trap-states and protects the PbS core during ligand exchange, and a 5-CT transmitter funnels energy down a gradient from NC sensitizer to rubrene annihilator. The exponential decrease in upconversion QY with increasing CdS shell thickness shows the Dexter-like energy transfer occurs, where the damping coefficient β, is 3.4 ± 0.1 Å^{-1}. This high damping coefficient suggests other shell materials with lower bandgaps than CdS should be utilized for PbS cores. In terms of molecular design, modifications to the tetracene core can be used to control the binding affinity, energetics, photophysics, etc of the transmitter ligand. Ultimately, this optimized hybrid upconversion platform may be used in thin films, perhaps in the form of organized frameworks[19] or polymer scaffolds, to surpass the Shockley-Queisser limit in TGPVs.

2.5 References

1. Green, M. A., *Third Generation Photovoltaics advanced solar energy conversion*. Springer: Berlin; Heidelberg, **2006**.

2. Schaller, R. D.; Klimov, V. I. *Physical Review Letters* **2004,** *92*, 186601.

3. Semonin, O. E.; Luther, J. M.; Choi, S.; Chen, H.-Y.; Gao, J.; Nozik, A. J.; Beard, M. C. *Science* **2011,** *334*, 1530-1533.

4. Beard, M. C. *The Journal of Physical Chemistry Letters* **2011,** *2*, 1282-1288.

5. Nozik, A. J. *Chemical Physics Letters* **2008,** *457*, 3-11.

6. Beard, M. C.; Midgett, A. G.; Hanna, M. C.; Luther, J. M.; Hughes, B. K.; Nozik, A. J. *Nano Letters* **2010,** *10*, 3019-3027.

7. Congreve, D. N.; Lee, J.; Thompson, N. J.; Hontz, E.; Yost, S. R.; Reusswig, P. D.; Bahlke, M. E.; Reineke, S.; Van Voorhis, T.; Baldo, M. A. *Science* **2013,** *340*, 334-337.

8. Tritsch, J. R.; Chan, W.-L.; Wu, X.; Monahan, N. R.; Zhu, X. Y. *Nat Commun* **2013,** *4*.

9. Tabachnyk, M.; Ehrler, B.; Bayliss, S.; Friend, R. H.; Greenham, N. C. *Applied Physics Letters* **2013,** *103*, 153302.

10. Auzel, F. *C. R. Acad. Sci. Paris* **1966,** *B262*, 1016-1019.

11. Auzel, F. *Chemical Reviews* **2004,** *104*, 139-174.

12. Zhou, J.; Liu, Q.; Feng, W.; Sun, Y.; Li, F. *Chemical Reviews* **2015,** *115*, 395-465.

13. Chen, G.; Qiu, H.; Prasad, P. N.; Chen, X. *Chemical Reviews* **2014,** *114*, 5161-5214.

14. So, P. T. C.; Dong, C. Y.; Masters, B. R.; Berland, K. M. *Annual Review of Biomedical Engineering* **2000,** *2*, 399-429.

15. Xu, C.; Webb, W. W. *Journal of the Optical Society of America B* **1996,** *13*, 481-491.

16. Huang, Z.; Li, X.; Mahboub, M.; Hanson, K. M.; Nichols, V. M.; Le, H.; Tang, M. L.; Bardeen, C. J. *Nano Letters* **2015,** *15*, 5552-5557.

17. Singh-Rachford, T. N.; Castellano, F. N. *Coordination Chemistry Reviews* **2010,** *254*, 2560-2573.

18. Schulze, T. F.; Schmidt, T. W. *Energy & Environmental Science* **2015,** *8*, 103-125.

19. Mahato, P.; Monguzzi, A.; Yanai, N.; Yamada, T.; Kimizuka, N. *Nat Mater* **2015,** *14*, 924-930.

20. Monguzzi, A.; Tubino, R.; Hoseinkhani, S.; Campione, M.; Meinardi, F. *Physical Chemistry Chemical Physics* **2012,** *14*, 4322-4332.

21. Yakutkin, V.; Filatov, M. A.; Ilieva, I. Z.; Landfester, K.; Miteva, T.; Baluschev, S. *Photochemical & Photobiological Sciences* **2015**.

22. Cheng, Y. Y.; Nattestad, A.; Schulze, T. F.; MacQueen, R. W.; Fuckel, B.; Lips, K.; Wallace, G. G.; Khoury, T.; Crossley, M. J.; Schmidt, T. W. *Chemical Science* **2016,** *7*, 559-568.

23. Englman, R.; Jortner, J. *Molecular Physics* **1970,** *18*, 145-164.

24. Wu, M.; Congreve, D. N.; Wilson, M. W. B.; Jean, J.; Geva, N.; Welborn, M.; Van Voorhis, T.; Bulović, V.; Bawendi, M. G.; Baldo, M. A. *Nat Photon* **2016,** *10*, 31-34.

25. Okamoto, T.; Suzuki, T.; Tanaka, H.; Hashizume, D.; Matsuo, Y. *Chemistry – An Asian Journal* **2012,** *7*, 105-111.

26. Montalti, M.; Credi, A.; Prodi, L.;Gandolfi, M. T. In *Handbook of photochemistry, third edition*, CRC Press: **2006,** 83-351.

27. Fang, H.-H.; Balazs, D. M.; Protesescu, L.; Kovalenko, M. V.; Loi, M. A. *The Journal of Physical Chemistry C* **2015,** *119*, 17480-17486.

28. Tenne, R.; Teitelboim, A.; Rukenstein, P.; Dyshel, M.; Mokari, T.; Oron, D. *ACS Nano* **2013,** *7*, 5084-5090.

29. Lechner, R. T.; Fritz-Popovski, G.; Yarema, M.; Heiss, W.; Hoell, A.; Schülli, T. U.; Primetzhofer, D.; Eibelhuber, M.; Paris, O. *Chemistry of Materials* **2014,** *26*, 5914-5922.

30. Geyer, S. M.; Scherer, J. M.; Moloto, N.; Jaworski, F. B.; Bawendi, M. G. *ACS Nano* **2011,** *5*, 5566-5571.

31. Neo, D. C. J.; Cheng, C.; Stranks, S. D.; Fairclough, S. M.; Kim, J. S.; Kirkland, A. I.; Smith, J. M.; Snaith, H. J.; Assender, H. E.; Watt, A. A. R. *Chemistry of Materials* **2014,** *26*, 4004-4013.

32. Kovalenko, M. V.; Schaller, R. D.; Jarzab, D.; Loi, M. A.; Talapin, D. V. *Journal of the American Chemical Society* **2012,** *134*, 2457-2460.

33. Moreels, I.; Lambert, K.; Smeets, D.; De Muynck, D.; Nollet, T.; Martins, J. C.; Vanhaecke, F.; Vantomme, A.; Delerue, C.; Allan, G.; Hens, Z. *ACS Nano* **2009,** *3*, 3023-3030.

34. Mahboub, M.; Maghsoudiganjeh, H.; Pham, A. M.; Huang, Z.; Tang, M. L. *Advanced Functional Materials* **2016,** 26, 6091-6097.

35. Huang, Z.; Li, X.; Yip, B. D.; Rubalcava, J. M.; Bardeen, C. J.; Tang, M. L. *Chemistry of Materials* **2015,** *27*, 7503-7507.

36. Speirs, M. J.; Balazs, D. M.; Fang, H. H.; Lai, L. H.; Protesescu, L.; Kovalenko, M. V.; Loi, M. A. *Journal of Materials Chemistry A* **2015,** *3*, 1450-1457.

37. Liu, Y.; Gibbs, M.; Puthussery, J.; Gaik, S.; Ihly, R.; Hillhouse, H. W.; Law, M. *Nano Letters* **2010,** *10*, 1960-1969.

38. Albrecht, C. *Analytical and Bioanalytical Chemistry* **2008,** *390*, 1223-1224.

39. Schmidt, T. W.; Castellano, F. N. *The Journal of Physical Chemistry Letters* **2014,** *5*, 4062-4072.

40. Cheng, Y. Y.; Khoury, T.; Clady, R. G. C. R.; Tayebjee, M. J. Y.; Ekins-Daukes, N. J.; Crossley, M. J.; Schmidt, T. W. *Physical Chemistry Chemical Physics* **2010,** *12*, 66-71.

41. Li, X.; Huang, Z.; Zavala, R.; Tang, M. L. *The Journal of Physical Chemistry Letters* **2016,** *7*, 1955-1959.

42. Wenger, O. S. *Chemical Society Reviews* **2011,** *40*, 3538-3550.

43. Huang, Z.; Simpson, D. E.; Mahboub, M.; Li, X.; Tang, M. L. *Chemical Science* **2016**, *7*, 4101-4104

44. Boyer, J.-C.; van Veggel, F. C. J. M. *Nanoscale* **2010,** *2*, 1417-1419.

45. Martín-Rodríguez, R.; Fischer, S.; Ivaturi, A.; Froehlich, B.; Krämer, K. W.; Goldschmidt, J. C.; Richards, B. S.; Meijerink, A. *Chemistry of Materials* **2013,** *25*, 1912-1921.

Chapter 3 Mid-gap States in PbS QDs Induced by Cd and Zn Enhance Photon Upconversion

3.1 Introduction

The high surface area to volume ratio of quantum dots (QDs) makes their optoelectronic properties more sensitive to surface states than bulk materials. Surface states control the rate, yield and direction of energy or charge transfer in QDs, and thus the performance of QD-based optoelectronic devices such as light emitting devices[1-4], photovoltaics[5-9], luminescent solar cell concentrators[10-13], etc. The nature of the core-shell interface is critical in controlling the fate of the QD exciton. Core-shell nanostructures have been used to mitigate the ligand and strain-induced defects at the QD surface, resulting in enhanced stability[14-15], photoluminescence quantum yields (PLQYs)[16-18], and the suppression of loss processes like Auger recombination[19]. For example, sharp interfaces along the core and shell material are predicted to create a large internal field within the QD, favoring multiple exciton generation for next-generation solar cells[19-20]. QDs with unit PLQYs employed as light emitters[17] typically have thick shells. While chemical passivation and band engineering can enhance the emission of core-shell QDs, the role of this interface in terms of charge or triplet energy transfer has not been clearly elucidated.

Considerable power conversion losses in solar cells are due to thermalization and sub-bandgap light transmission. While thermalization is the main loss pathway for low bandgap materials (bandgap, Eg, lower than 1.3 eV) such as silicon, transmission losses dominate for high bandgap materials (Eg > 1.3 eV) such as CdTe. One solution for these losses are tandem solar cells that consist of several semiconductors with different bandgaps that each absorb a specific portion of the solar spectrum. However, these tandem cells are expensive. Potentially inexpensive solutions for thermalization are singlet fission and multiple exciton generation, while photonic upconversion is a promising solution for harvesting the transmitted photons. As more than half of the solar irradiance (53%) is within the 700-2500 nm range, the possibility of NIR-to-VIS photon upconversion system is attractive.

We have previously shown that PbS-CdS core-shell QDs that absorb maximally at 850 nm can convert NIR light to yellow light in solution at sub-solar excitation densities with state of the art efficiencies of 8-9 %[21], while Wu and Baldo[22] have shown that core-only PbS QDs excited with 980 nm incident light can convert 1.6% of absorbed NIR photons into visible light in thin film[22-23]. Since triplet exciton transport between QDs and molecules for photon up- or downconversion is thought to occur via a Dexter process, sub-monolayer shells are optimal, in stark contrast to the 'giant' shells used for light emitting QDs. Similarly, the power conversion efficiency of PbS QDs solar cells is enhanced by thin shells composed of cadmium[16, 24-28] and zinc[24, 28-29] cations. Various factors account for the improved power conversion efficiency, including an increase in the PL lifetime of the QDs[18], enhancement of the PLQY[17-18], longer electron lifetime and higher electron mobility in the PbS QDs film[25]. Transient photovoltage measurements of the PbS QD films after treatment with Cd^{2+} and Zn^{2+} cations show that the saturation of mid-gap states[24] minimizes traps detrimental to charge transport.

3.2 Result and discussion

In this work, we focus on PbS QDs with sub-monolayer shells, as part of a hybrid photon upconversion platform that combines triplet excitons to make high-energy photons, shown in **Figure 1**a. We sought to extend the absorption of the PbS-based core-shell QDs further out to the near-infrared (NIR), and investigate the role of shell composition and structure on triplet exciton transfer from QDs to molecular species. The QDs' role during photon upconversion is to photosensitize rubrene triplet states. Then in a spin-allowed process called triplet-triplet annihilation (TTA), spin-triplet excitons on two neighboring rubrene molecules interact to create one rubrene in the ground state and the other in its singlet excited state.

Here, we use oleylamine to explore six different cations (Cd^{2+}, Zn^{2+}, Sn^{2+}, In^{2+}, Ni^{2+}, and Bi^{2+}) for improving the performance of PbS QDs photosensitizers for photon upconversion. Out of the six shell materials investigated, only Zn and Cd cation adsorbates on the PbS QD light absorber increase the photon upconversion QY by up to 3 orders of magnitude. Compared to the PbS core, these Zn and Cd coated QDs have slightly lower radiative and non-radiative recombination rates (up to 28%), and increased absorption and emission linewidths. The latter is typically associated with increased exciton-phonon or electron-phonon coupling, or increased defect states. The data here suggest that thermally accessible mid-gap defect states created by these adsorbates mitigate triplet energy transfer from PbS QDs to rubrene emitters. We note that the nature of the excitonic state(s) on the QD responsible for sensitizing molecular triplet states has not been experimentally determined. In order to conserve spin, triplet transfer should arise from the dark excitonic states at the band edge that have triplet character, that are typically within *kT* of the bright singlet states in QDs capable of coupling to light. However, defect states, which stem from the non-stoichiometric composition of QDs and dangling bonds on the surface, may very well possess sufficient triplet character necessary for sensitizing spin un-paired molecular excitonic states.

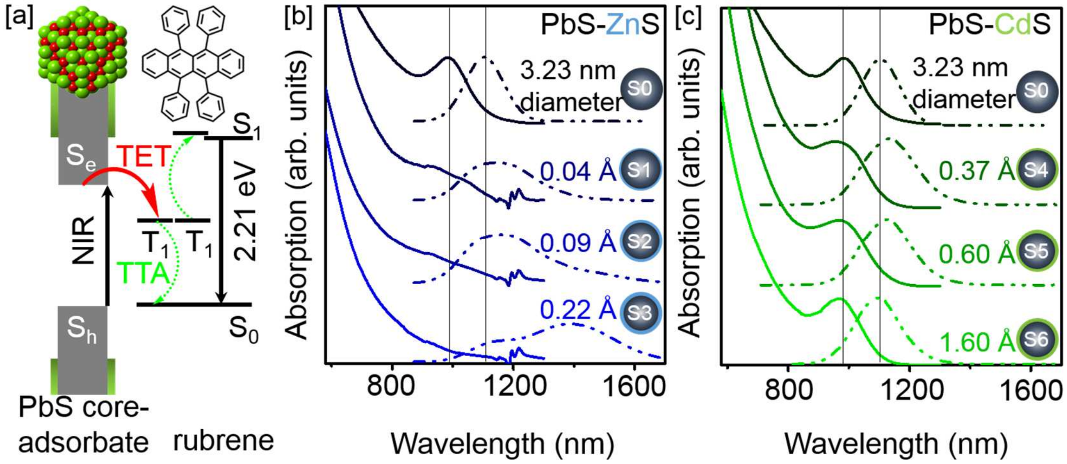

Figure 3.1. [a] Schematic of the energy transfer in this hybrid upconversion platform. PbS quantum dot (QD) light absorbers with Zn and Cd adsorbates and rubrene emitters convert two absorbed NIR photons to yellow photons. The absorption (solid line) and photoluminescence spectrum (dashed-dot line) of [b] PbS-ZnS (blue) and [c] PbS-CdS (green) core-adsorbate QDs with various shell thicknesses from a 3.23 nm diameter PbS QD core. The spectra were obtained in hexane at RT.

The cation adsorbates investigated have a very similar redox potential and ionic crystal radius compared to Pb^{2+}, as summarized in Table S1. The observation that only Cd^{2+} and Zn^{2+} show an enhancement of the upconversion QY is in line with a report by Sargent et al that the best PbS QD photovoltaic performance occurred with Cd, Zn and Ca treatment, while the other metal-chloride salts (Hg, As, Sn, In, Sb, Ga, Sr, Cu) failed to give any improvement[24].Thus this report will focus on the properties of QDs incorporating

Cd and Zn ions. The absorption (solid line) and emission (dash-dotted line) spectrum of three PbS-ZnS (Samples 1-3, S1-S3) and PbS-CdS (Samples 4-6, S4-S6) core-adsorbate QDs synthesized from 3.23 nm diameter PbS cores (Sample 0, S0) with various shell thicknesses are shown in Figure 1b, c respectively. The supporting information includes core-adsorbate QDs obtained from PbS QDs of 3.12 and 3.18 nm diameter (Figure S1 and S2). Different sizes of PbS QDs were synthesized following our previous work[30] and QD size and concentration were determined from their absorption spectrum[31]. As shown in **Figure 2**a and 2f, the adsorbates were introduced with oleylamine due to the higher solubility of their acetate salts compared to the use of oleic acid as solvent. This allowed the cations to be adsorbed at lower temperature to minimize cation exchange, which occurs rapidly when cadmium oleate is introduced. However, the oleylamine used during synthesis here binds less strongly than the original oleic acid ligand. We found that it was necessary to quench the reaction with oleic acid in order to produce colloidally stable core-adsorbate QDs. ICP-OES was carried out to determine the amount of Zn^{2+} and Cd^{2+} cations incorporated (**Table 1**). We found estimates of shell thickness from the absorption spectrum are an underestimate due to exciton delocalization. With the molar ratios of each metal given by ICP-OES, the average ZnS and CdS shell thickness were calculated, assuming the adsorbate was uniformly distributed on the spherical QD whose volume remained constant. (See SI for details).

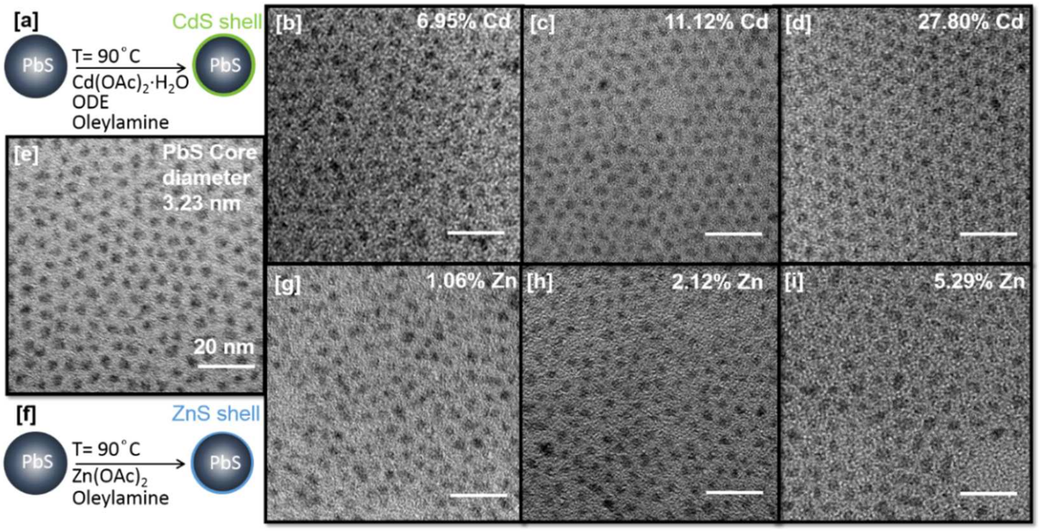

Figure 3.2. Transmission electron micrographs of [a-d] PbS-CdS and [f-i] PbS-ZnS core-adsorbate quantum dots (QDs) synthesized from [e] 3.23 nm diameter PbS QDs. PbS-CdS core-adsorbate with 7.0%, 11.1% and 27.8 mol % of Cd in [b], [c] and [d] respectively. PbS-ZnS core-adsorbate with 1.1%, 2.1% and 5.3 mol % of Zn in [g], [h] and [i] respectively. The scale bar is 20 nm for all the images. The mol % is measured by ICP-OES, refers to the mol % of metal ions and does not include the sulfide.

Table 3.1: Key parameters for the PbS-ZnS and PbS-CdS core-shell QDs: Zn and Cd atomic percent in the PbS-ZnS and PbS-CdS QDs, Zn and Cd; shell thickness, *d*; absorption maxima, λ_{abs}; emission maxima, λ_{ems}; photoluminescence quantum yield, PLQY; QD PL decay lifetime, τ; radiative decay rate, k_r; non-radiative decay rate, k_{nr}; and photon upconversion QY (UCQY);

Sample #	Zn [%]^a	Cd [%]^a	d [Å]	λ_{abs} [nm]	λ_{ems} [nm]	PL QY [%]^b	τ [μs]	k_r [1/s×10^4]	k_{nr} [1/s×10^4]	UCQY [%]^c
PbS core0	0	0	0	983	1103	14.35	3.72	3.86	2.30	0.0004
PbS-ZnS1	1.06	0	0.04		1144	16.89	5.11	3.31	1.63	0.28
PbS-ZnS2	2.12	0	0.08		1156	13.14	4.95	2.65	1.75	0.26
PbS-ZnS3	5.29	0	0.22		1161-1386	11.67				0.11
PbS-CdS4	0	6.95	0.37	956	1138	15.58	4.71	3.31	1.79	0.11
PbS-CdS5	0	11.1	0.60	967	1126	16.81	5.06	3.32	1.64	0.13
PbS-CdS6	0	27.8	1.60	968	1096	21.36				0.04

a)Obtained from ICP-OES elemental analysis. Zn%=(Zn^{2+}/ (Pb^{2+}+ Zn^{2+}))×100 an Cd%=(Cd^{2+}/ (Pb^{2+}+ Cd^{2+}))×100; b)Hexane at RT with ICG in DMSO used as standard; c)2 mM rubrene in toluene at RT; QDs were excited at 680 nm for PLQY and 0.24 W/cm^2 78 nm CW laser was used for photon upconversion QY measurements.

Transmission electron micrograph images in Figure 2 reveal a monodisperse size distribution of QDs. From this, we conclude that the linewidth broadening in Figure 1 is homogenous, i.e. the ICP measured amount of Zn and Cd cations are equally distributed over all the PbS QDs. The presence of CdS adsorbates blue shifts the QD absorption either due to PbS volume contraction from cation exchange or alloy formation[14, 16, 18, 24-25, 32]. PbS-CdS4 to PbS-CdS6 samples correspond to CdS shell thicknesses of 0.37, 0.60, and 1.60 Å respectively. PbS-CdS4 with a 0.37 Å CdS shell has ~27 nm blue shift in the absorption and 35 nm red shift in the PL maxima. PbS-CdS5 has a similar red shift in PL. The red shift in the PL is most likely due to emission from defect states[33]. The small lattice mismatch (1.8%) between the CdS and PbS and similar ionic radii of Cd^{2+} (109 pm) and Pb^{2+} (119 pm) results in a significantly smaller linewidth for the absorption and emission maxima compared to when ZnS is adsorbed.

For the PbS-ZnS core-adsorbate series of QDs, the ZnS shell thicknesses were 0.04, 0.09, and 0.22 Å for samples PbS-ZnS1 to PbS-ZnS3 respectively. Compared to the PbS core, this increase in the shell thickness for PbS-ZnS1 resulted in a large 38 nm red-shift in the PL maxima compared to the PbS core. For PbS-ZnS3, ZnS shells exceeding 0.22 Å resulted in an even broader, red-shifted photoluminescence that is typically associated with trap states. This trap state emission accounted for 74% of the total photoluminescence. The first absorption maxima of these PbS-ZnS core-adsorbate QDs broaden significantly. TEM images in Figure 2g, h, i do not show a drastic ripening, suggesting this extremely broad absorption is due to homogenous broadening. Zinc blende ZnS and rock salt PbS have a large lattice mismatch (8.9%) because the Zn^{2+} crystal ion radius (87 pm) is smaller than the Pb^{2+}(119 pm). At low Zn^{2+} loadings where $[Zn^{2+}/ (Pb^{2+}+Zn^{2+})] < 0.06$, Zn^{2+} very likely occupies the Pb^{2+} sites on the QD surfaces and the lattice distortion is compensated by dislocation and defect formation. However, at higher loading, further addition of Zn^{2+} to the QDs distorts the lattice and generates defects that perturb the electronic absorption and PL spectrum.

Addition of the Cd and Zn enhances the photon upconversion QY by as much as 325 and 700 times respectively, as shown in **Figure 3a** and **3b**. This increases the photon upconversion QY from 0.0004% (PbS) to 0.28% (PbS-ZnS1) and 0.13% (PbS-CdS5) (See SI for details). During photon upconversion, a 785 nm NIR laser excites the QDs. As shown in Figure 1a, energy is transferred from the QDs sensitizer (donor) to the rubrene annihilator (acceptor). Two rubrene triplet excitons fuse to generate one rubrene molecule in its ground state and the other in its singlet excited state. This converts two NIR photons to one visible photon[21, 34]. As we observed before, when the shell is too thick, the photon upconversion QY decreases[21]. Since triplet exciton transfer is best described by the Dexter mechanism[21, 35], submonolayer shells are necessary because thick shells present an insurmountable tunneling barrier for triplet excitons[21]. Figure 3c and 3d show the relationship between PL QY, photon upconversion QY and shell thickness. Upon adsorbing Cd cations, the PLQY of the PbS QDs increase from 14% to 21%, while it is almost unchanged with Zn cations. While PLQY is generally accepted as a marker for the quality of semiconductor QDs, radiative recombination is but one decay pathway for the QD's excitonic state, and no correlation of the PLQY with the photon upconversion QY is observed here.

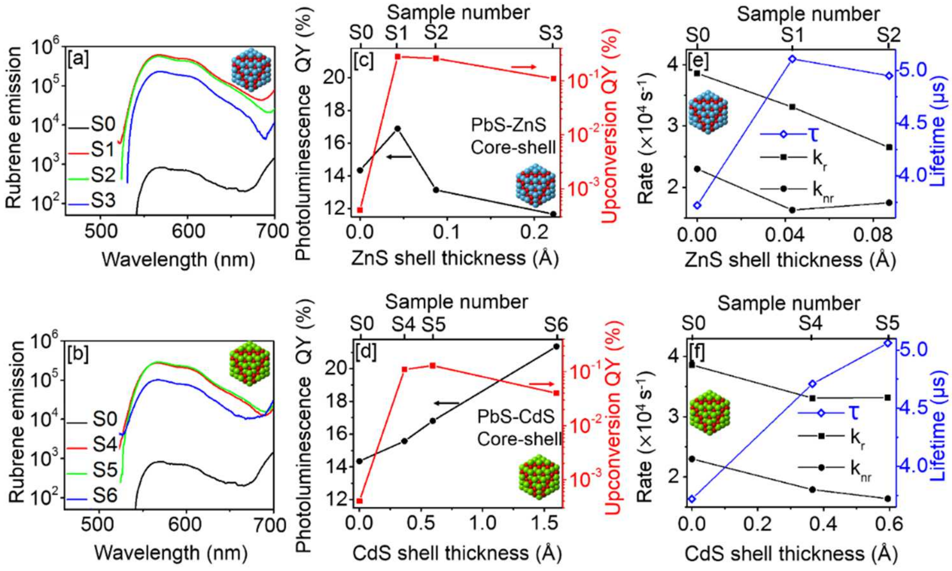

Figure 3.3 The upconverted light emitted by 20 mM rubrene in the presence of [a] PbS-ZnS and [b] PbS-CdS core-adsorbate QDs synthesized from a 3.23 nm diameter PbS QD when excited with a 0.24 W/cm^2 785 nm CW laser. The optical density of the QDs at the excitation wavelength was 0.002. The photon upconversion and QD photoluminescence quantum yield (PLQY) of [c] PbS-ZnS and [d] PbS-CdS core-shell QDs. The PLQY was in hexane while upconversion QY was in toluene. Radiative and non-radiative decay rates, k_r and k_{nr}, and PL decay lifetimes for [e] PbS-ZnS, and [f] PbS-CdS core-shell QDs in hexane. QDs were excited at 800 nm with a 1.43 μW picosecond laser at a repetition rate of 35.7 kHz. All measurements were at RT.

Time correlated single photon counting (TCSPC) (Figure 3) and PLQY (Figure 3c and 3d) measurements were performed to study the effect of the shell on QD lifetime. The same trends in the photon upconversion QYs, PLQYs and lifetimes were obtained for another set of 3.12 and 3.18 nm diameter PbS QDs (see Figure S3). As seen in Figure S4 to S8, the decays were monoexponential. The radiative and non-radiative decay rates, k_r and k_{nr}, can be extracted from the PLQY and the lifetime of the QDs (equation 1)[36]. These values are listed in Table 1.

$$\mathrm{PLQY}=\frac{k_r}{k_r+k_{nr}}=k_r\times\tau \qquad (1)$$

Compared to the PbS core, the core-adsorbate QDs here have comparable radiative recombination rates, k_r, in contrast to previous reports regarding PbS-CdS core-shell QDs[18]. This is because in previous work, CdS shells ranged from 0.2-3.6 nm, but the sub-monolayer growth here (<0.08 nm) does not passivate all the defects completely, resulting in lower radiative rates for all the core-adsorbate structures here compared to the original PbS core. A change in electronic structure due to the core-shell geometry might also explain the slightly reduced radiative rates. Fang et al. report a quasi-type II heterostructure with CdS shell thicknesses less than 0.8 nm synthesized by cation exchange of a 3.5 nm diameter PbS core. Since the electron is delocalized over the entire particle and the hole localized in the PbS core, the radiative rates are diminished compared to the core. Further increase in shell thickness results in a Type I heterostructure for these PbS-CdS core-shell QDs, as expected for the bulk material[37]. Here, the non-radiative recombination rates of core-adsorbate QDs decrease from 2.30×10^4 s^{-1} to 1.75×10^4 s^{-1} and 1.64×10^4 s^{-1} with the addition of ZnS and CdS. This general trend shows that subsets of the surface traps are passivated by the formation of these submonolayer shells.

The photon upconversion QY closely tracks the absorption and PL linewidth of the QDs, i.e., QDs with larger linewidths have a higher upconversion QY. This suggests that defect states mediate energy transfer from PbS QDs to rubrene triplets (**Figure 4**a). This is most clearly seen in Figure 4b for 3.12, 3.18, 3.23 nm diameter PbS QDs, where the PL linewidth of the PbS-CdS core-adsorbate QDs normalized by that of the PbS core only is compared to the photon upconversion QY for different shell thicknesses. Similarly, Zn adsorbates result in an extremely broad absorption and PL, and up to a 700x increase in the photon upconversion QY (Fig. 1b, Fig. S3c and S3d). Trap mediated hole transfer was recently observed from CdSe-CdS core-shell QDs to surface-bound ferrocene derivatives using temperature dependent TCSPC measurements[38]. While it is challenging to characterize the chemical nature of these defect states that result in broader absorption and PL, these adsorbates might create dangling bonds with open-shell character that allow spin to be conserved when the photoexcited QDs transfer triplet excitons to rubrene. Using solution photon-correlation Fourier spectroscopy (S-PCFS), Bawendi et al found evidence of thermally accessible emissive defect states in PbS QDs that are energetically pined with respect to the band-edge[33]. Decreasing QD size or increasing bandgap makes the defect states more thermally accessible. The QDs used in this study are comparable to the QDs that Bawendi et al used (2.1-4.1 nm), which places this emissive defect states at the conduction band or below the conduction band of our 3.2 nm diameter PbS QDs. When CdS is adsorbed, the blue shift in the absorption maxima (> 25 nm) makes these defect states more energetically accessible, as seen by the broadened PL linewidth.

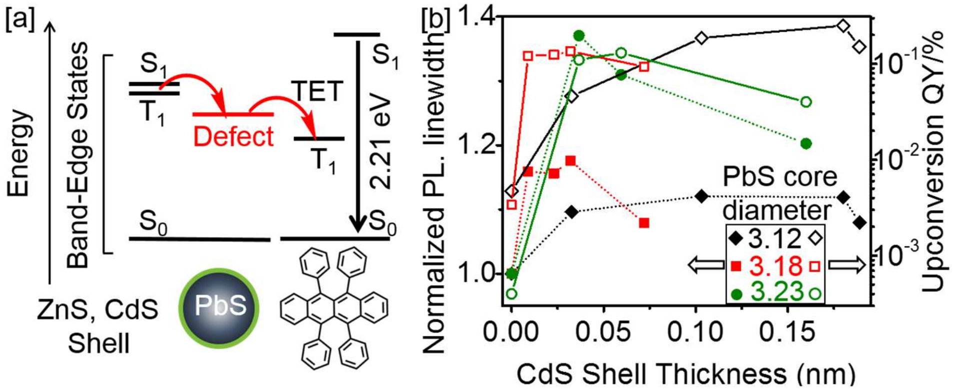

Figure 3.4. [a] Schematic of defect state mediated triplet energy transfer (TET) from PbS-CdS and PbS-ZnS core-adsorbate quantum dots (QDs) to the rubrene triplet state. [b] The normalized photoluminescence (PL) linewidth and upconversion QY of PbS-CdS core-adsorbate QDs with various shell thicknesses synthesized from differently sized PbS QDs.

3.3 Conclusion

In summary, as light-absorbers, PbS-ZnS and PbS-CdS core-adsorbate QDs with sub angstrom shell thicknesses enhance the photon upconversion QYs by 700 and 325 times respectively despite the fact that both the radiative and non-radiative recombination rates decrease and QD PL remains about the same. Significantly, the absorption and photoluminescence linewidths follow the trend in the photon upconversion QYs, where the core-shell QDs with the broadest PL maxima with respect to the PbS core QD gives the highest photon upconversion QY, up to 0.25%. While these submonolayer Cd and Zn shells may chemically passivate certain trap states, the other defects introduced enhance triplet energy transfer and thus the linear photon upconversion QY. This work suggests that thermally accessible mid-gap states created by surface bound adsorbates contribute to molecular triplet sensitization by QDs. It provides a framework for optimizing triplet energy transfer between QDs and molecules, important for energy conversion, imaging, and optogenetics[39].

3.4 References

1. Bruchez, M.; Moronne, M.; Gin, P.; Weiss, S.; Alivisatos, A. P. *Science* **1998,** *281*, 2013-2016.

2. Klimov, V. I.; Mikhailovsky, A. A.; Xu, S.; Malko, A.; Hollingsworth, J. A.; Leatherdale, C. A.; Eisler, H.-J.; Bawendi, M. G. *Science* **2000,** *290*, 314-317.

3. Klimov, V. I.; Ivanov, S. A.; Nanda, J.; Achermann, M.; Bezel, I.; McGuire, J. A.; Piryatinski, A. *Nature* **2007,** *447*, 441.

4. Wood, V.; Bulović, V. *Nano Rev* **2010,** *1*.

5. Tang, J.; Sargent, E. H. *Advanced Materials* **2011,** *23*, 12-29.

6. Koleilat, G. I.; Levina, L.; Shukla, H.; Myrskog, S. H.; Hinds, S.; Pattantyus-Abraham, A. G.; Sargent, E. H. *ACS Nano* **2008,** *2*, 833-840.

7. Chuang, C.-H. M.; Brown, P. R.; Bulović, V.; Bawendi, M. G. *Nature Materials* **2014,** *13*, 796.

8. Zhao, N.; Osedach, T. P.; Chang, L.-Y.; Geyer, S. M.; Wanger, D.; Binda, M. T.; Arango, A. C.; Bawendi, M. G.; Bulovic, V. *ACS Nano* **2010,** *4*, 3743-3752.

9. Ren, S.; Chang, L.-Y.; Lim, S.-K.; Zhao, J.; Smith, M.; Zhao, N.; Bulović, V.; Bawendi, M.; Gradečak, S. *Nano Letters* **2011,** *11*, 3998-4002.

10. Meinardi, F.; McDaniel, H.; Carulli, F.; Colombo, A.; Velizhanin, K. A.; Makarov, N. S.; Simonutti, R.; Klimov, V. I.; Brovelli, S. *Nature Nanotechnology* **2015,** *10*, 878.

11. Meinardi, F.; Colombo, A.; Velizhanin, K. A.; Simonutti, R.; Lorenzon, M.; Beverina, L.; Viswanatha, R.; Klimov, V. I.; Brovelli, S. *Nature Photonics* **2014,** *8*, 392.

12. Bradshaw, L. R.; Knowles, K. E.; McDowall, S.; Gamelin, D. R. *Nano Letters* **2015,** *15*, 1315-1323.

13. Erickson, C. S.; Bradshaw, L. R.; McDowall, S.; Gilbertson, J. D.; Gamelin, D. R.; Patrick, D. L. *ACS Nano* **2014,** *8*, 3461-3467.

14. Clark, P. C. J.; Radtke, H.; Pengpad, A.; Williamson, A. I.; Spencer, B. F.; Hardman, S. J. O.; Leontiadou, M. A.; Neo, D. C. J.; Fairclough, S. M.; Watt, A. A. R.; Pis, I.; Nappini, S.; Bondino, F.; Magnano, E.; Handrup, K.; Schulte, K.; Silly, M. G.; Sirotti, F.; Flavell, W. R. *Nanoscale* **2017,** *9*, 6056-6067.

15. Kovalenko, M. V.; Schaller, R. D.; Jarzab, D.; Loi, M. A.; Talapin, D. V. *Journal of the American Chemical Society* **2012,** *134*, 2457-2460.

16. Neo, D. C. J.; Cheng, C.; Stranks, S. D.; Fairclough, S. M.; Kim, J. S.; Kirkland, A. I.; Smith, J. M.; Snaith, H. J.; Assender, H. E.; Watt, A. A. R. *Chemistry of Materials* **2014,** *26*, 4004-4013.

17. Supran, G. J.; Song, K. W.; Hwang, G. W.; Correa, R. E.; Scherer, J.; Dauler, E. A.; Shirasaki, Y.; Bawendi, M. G.; Bulović, V. *Advanced Materials* **2015,** *27*, 1437-1442.

18. Zhao, H.; Chaker, M.; Wu, N.; Ma, D. *Journal of Materials Chemistry* **2011,** *21*, 8898-8904.

19. Bae, W. K.; Padilha, L. A.; Park, Y.-S.; McDaniel, H.; Robel, I.; Pietryga, J. M.; Klimov, V. I. *ACS Nano* **2013,** *7*, 3411-3419.

20. Eshet, H.; Baer, R.; Neuhauser, D.; Rabani, E. *Nature Communications* **2016,** *7*, 13178.

21. Mahboub, M.; Huang, Z.; Tang, M. L. *Nano Letters* **2016,** *16*, 7169-7175.

22. Wu, M.; Congreve, D. N.; Wilson, M. W. B.; Jean, J.; Geva, N.; Welborn, M.; Van Voorhis, T.; Bulović, V.; Bawendi, M. G.; Baldo, M. A. *Nat Photon* **2016,** *10*, 31-34.

23. Wu, M.; Jean, J.; Bulović, V.; Baldo, M. A. *Applied Physics Letters* **2017,** *110*, 211101.

24. Thon, S. M.; Ip, A. H.; Voznyy, O.; Levina, L.; Kemp, K. W.; Carey, G. H.; Masala, S.; Sargent, E. H. *ACS Nano* **2013,** *7*, 7680-7688.

25. Lai, L.-H.; Protesescu, L.; Kovalenko, M. V.; Loi, M. A. *Physical Chemistry Chemical Physics* **2014,** *16*, 736-742.

26. Speirs, M. J.; Balazs, D. M.; Fang, H. H.; Lai, L. H.; Protesescu, L.; Kovalenko, M. V.; Loi, M. A. *Journal of Materials Chemistry A* **2015,** *3*, 1450-1457.

27. Neo, D. C. J.; Stranks, S. D.; Eperon, G. E.; Snaith, H. J.; Assender, H. E.; Watt, A. A. R. *Applied Physics Letters* **2015,** *107*, 103902.

28. Marshall, A. R.; Young, M. R.; Nozik, A. J.; Beard, M. C.; Luther, J. M. *The Journal of Physical Chemistry Letters* **2015,** *6*, 2892-2899.

29. Hachiya, S.; Shen, Q.; Toyoda, T. *Journal of Applied Physics* **2012,** *111*, 104315.

30. Mahboub, M.; Maghsoudiganjeh, H.; Pham, A. M.; Huang, Z.; Tang, M. L. *Advanced Functional Materials* **2016**, *26*, 6091-6097.

31. Moreels, I.; Lambert, K.; Smeets, D.; De Muynck, D.; Nollet, T.; Martins, J. C.; Vanhaecke, F.; Vantomme, A.; Delerue, C.; Allan, G.; Hens, Z. *ACS Nano* **2009,** *3*, 3023-3030.

32. Neo, M. S.; Venkatram, N.; Li, G. S.; Chin, W. S.; Ji, W. *The Journal of Physical Chemistry C* **2010,** *114*, 18037-18044.

33. Caram, J. R.; Bertram, S. N.; Utzat, H.; Hess, W. R.; Carr, J. A.; Bischof, T. S.; Beyler, A. P.; Wilson, M. W. B.; Bawendi, M. G. *Nano Letters* **2016,** *16*, 6070-6077.

34. Huang, Z.; Li, X.; Mahboub, M.; Hanson, K. M.; Nichols, V. M.; Le, H.; Tang, M. L.; Bardeen, C. J. *Nano Letters* **2015,** *15*, 5552-5557.

35. Li, X.; Huang, Z.; Zavala, R.; Tang, M. L. *The Journal of Physical Chemistry Letters* **2016,** *7*, 1955-1959.

36. Albrecht, C.; Lakowicz, J. R. 3rd Edition. Analytical and Bioanalytical Chemistry **2008,** 390, 1223-1224

37. Fang, H. H.; Balazs, D. M.; Protesescu, L.; Kovalenko, M. V.; Loi, M. A. *The Journal of Physical Chemistry C* **2015,** *119*, 17480-17486.

38. Olshansky, J. H.; Balan, A. D.; Ding, T. X.; Fu, X.; Lee, Y. V.; Alivisatos, A. P. *ACS Nano* **2017,** *11*, 8346-8355.

39. Chen, S.; Weitemier, A. Z.; Zeng, X.; He, L.; Wang, X.; Tao, Y.; Huang, A. J. Y.; Hashimotodani, Y.; Kano, M.; Iwasaki, H.; et al., Science **2018,** 359, 679-684.

Chapter 4 The tale of two lead chalcogenides: PbSe nanocrystals are better triplet photosensitizers than PbS

In 2015, we showed that native PbSe nanocrystal (NC) light absorbers are better for photon upconversion compared to their PbS counterparts. At that time, the oleic acid capped NCs were directly mixed with the rubrene emitter without further functionalization. The goal of this chapter is to get to the bottom of this observation, and to investigate if this robust and reproducible difference in PbS and PbSe nanocrystals is electronic or structural. The fact that PbSe has almost double the Bohr radius at 44 nm means that for similarly sized NCs, the PbSe exciton wavefunction leaks out further beyond the physical confines of the particle, compared to PbS with a 19 nm Bohr radius. However, interfacial properties, e.g. capping ligand density or surface defects, etc., may also alter the efficiencies of triplet energy transfer. The insulating long chain oleic acid aliphatic ligand serves as a physical barrier to Dexter transfer and the differences in ligand density may affect the ability of the rubrene acceptor to approach the PbX NC donor. Unfortunately, surface defects are difficult to characterize, but may be reflected in time-resolved lifetime measurements.

In order to systematically study these differences in this NIR to visible hybrid photon upconversion system, we studied a whole range of PbS and PbSe NCs with bandgaps at or above the lowest triplet excited state in tetracene (1.1 eV). The photon upconversion QY utilizing these NCs as light absorbers in the presence and absence of the 5-CT transmitter ligand was measured, in tandem with TCSPC, FTIR and NMR measurements to fully characterize the lifetime, ligand binding geometry and density in the NCs.

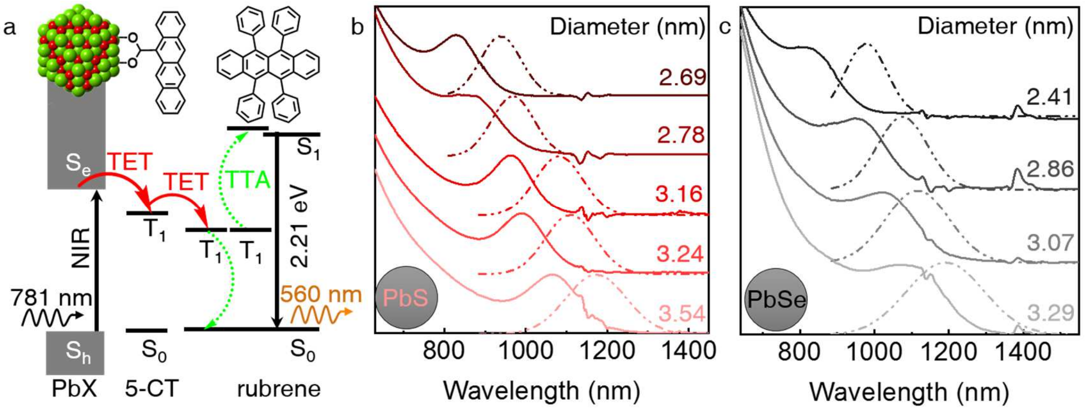

Figure 4.1. PbX (X=S and Se) nanocrystals (NCs), 5-CT, and rubrene serve as the sensitizer, transmitter, and annihilator respectively in this hybrid photon upconversion system. (a) Schematic of the energy transfer. The absorption (solid line) and emission spectrum (dashed-dotted line) of b) PbS NCs and c) PbSe NCs of different sizes in toluene at room temperature.

As shown in Fig. 1a, the PbX NCs absorb the near-infrared photons. 5-CT is the transmitter ligand bound to the surface of the NCs that mediates TET from the NC to the rubrene emitter. Rubrene then undergoes TTA to upconvert light, producing high-energy photons in the visible. Fig. 1b and 1c show the absorption and photoluminescence spectra of all the NCs used in this study.

Here, all the NCs were synthesized under air-free conditions with the hot injection method, using the bis(trimethylsilyl) chalcogenide precursors, TMS_2S and TMS_2Se in combination with PbO. The exception is the smallest PbS NCs, which was synthesized with a thiourea sulfur precursor in the presence of lead oleate. All the particles were cleaned and stored in air-free gloveboxes. Here the photon upconversion experiments are performed within a month of NC synthesis to minimize particle degradation.

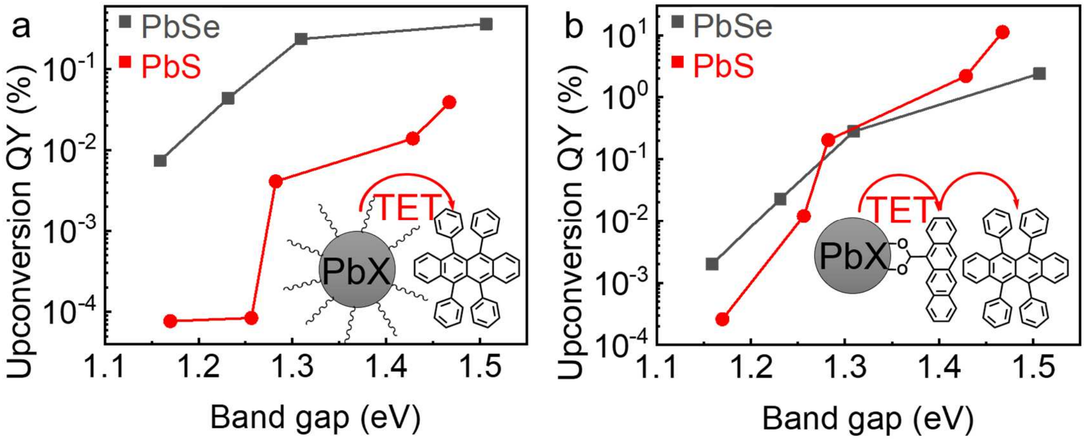

Figure 4.2. The effect of nanocrystal (NC) composition and size (a) before and (b) after 5-CT ligand exchange on the photon upconversion QY of NIR light to visible light. NCs were excited with 781 nm laser. Rubrene and NC concentration were 20 mM and 10 μM respectively. All measurements were performed in toluene at RT.

In the absence of the transmitter ligand, the oleic acid-only capped PbSe NCs shows significantly higher uponcversion QY than PbS NCs when combined with rubrene. We find that the ligand density and surface binding geometry are around the same, and no significant differences in lifetime were detected by TCSPC measurements. When the 5-CT transmitter ligand is bound to the NC surface, both NCs perform equally well. Thus, we conclude that the larger Bohr radius for PbSe NCs makes them better triplet photosensitizers compared to PbS in the absence of the transmitter ligands.

4.1 Photophysical and electronic observations:

Photophysical properties of the NCs were studied by performing time correlated singlet photon counting (TCSPC), PL QY, and photon upconversion QY measurements on the nanocrystals in the presence and absence of the triplet acceptor rubrene, in toluene at

RT. In follow we present the different decay model for dynamics of the PbS decay at different situations:

4.1.1 Native Oleic Acid (OA) capped QDs

The PL lifetime of the largest diameter PbS (3.54 nm) and PbSe NCs (3.29 and 3.07 nm) decay biexponential with short ns and long μs lifetimes (Fig. 3). The rest of the QDs decay monoexponentially. The TCSPC lifetimes fit to single monoexponentials for the smaller NCs and biexponentials for the larger NCs are given in Table 1. We calculated radiative (k_r) and nonradiative (k_{nr}) decay rates using the steady-state PL QY measured with an ICG standard (Equation 1) and the intensity weighted lifetime (Equation 2):

(1) PL QY%$=\frac{k_r}{k_r+k_{nr}}=k_r.<\tau_{NC}>$

(2) $<\tau_{NC}>=\frac{a_1.{\tau_1}^2+a_2.{\tau_2}^2}{a_1\tau_1+a_2\tau_2}$

The intensity weighted lifetimes of these PbS and PbSe NCs decrease by a factor of 2 as the NC size increases from 2.69 to 3.54 and 2.41 to 3.29 nm in diameter respectively. On the other hand, the PL QY of these NCs decrease by 2.1 and 2.6 times as the NCs size increases. PL QY of the PbS NCs are comparable to the PL QY of the PbSe NCs, hovering around 10-24%.

Table 4.1. Parameters obtained from steady state and TCSPC photoluminescence (PL) measurements of oleic acid capped NCs. $<\tau_{NC}>$= intensity weighted lifetime, PL QY= PL quantum yield, k_r = radiative decay rate, k_{NC}= NC decay rate= k_r+ k_{nr}. a. In toluene at RT. b. Calculated from $<\tau_{NC}>$ and steady state PL QY measurement (Equation 1) with excitation at 700 nm and ICG in DMSO as standard.; c. PL QY of the NCs when mixed with rubrene.

Sample	τ_1 (μs)	a_1	τ_2 (μs)	a_2	$<\tau_{NC}>$ (μs)	k_r^a (1/s×10^6)	k_{NC}^a (1/s×10^6)	PL QY^b (%)	PL QY^c (%)
PbS-845-Owen	7.36	1			7.36	0.012	0.136	8.8	9.9
PbS-967	5.42	1			5.42	0.0439	0.185	23.8	22.9
PbS-987	3.54	1			3.54	0.04	0.282	14.2	14.6
PbS-1060	3.46	0.643	0.512	0.329	3.25	0.035	0.308	11.4	10.8
PbSe-823	6.04	1			6.04	0.0394	0.166	23.8	16.5
PbSe-947	3.87	1			3.87	0.0265	0.258	10.3	12.2
PbSe-1007	3.52	0.679	0.0447	12	2.88	0.0338	0.347	9.7	8.5
PbSe-1070	3.31	0.698	0.0638	3.9	2.99	0.0306	0.334	9.2	7.8

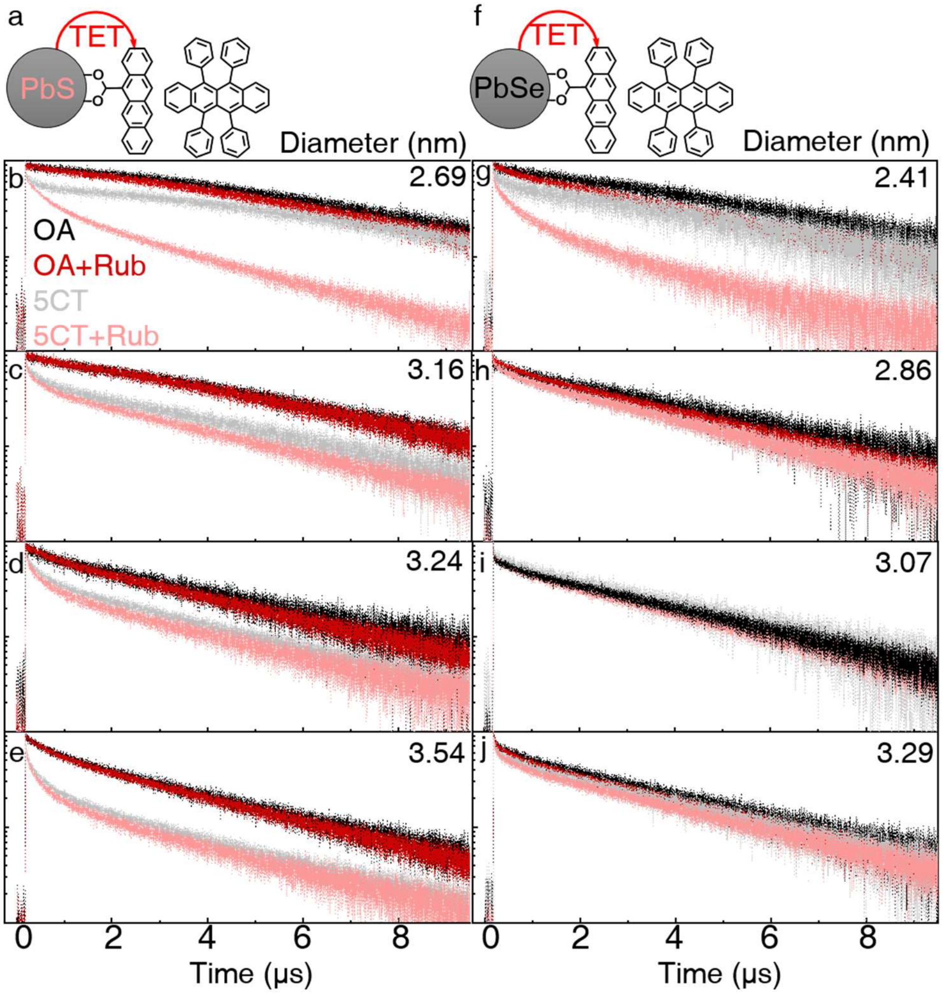

Figure 4.3. Schematic of triplet energy transfer (TET) in this hybrid photon upconversion platform when (a) PbS (f) PbSe serve as triplet photosensitizers. The PL decay lifetime from TCSPC measurements of differently sized PbS (b, c, d, e) and PbSe QDs (g-h-i-j). QD diameter varies from 2.69 to 3.54 nm for PbS and 2.41 to 3.29 nm for PbSe (labelled). The red and black traces correspond to oleic acid capped NCs PL decay with and without rubrene respectively, while the gray and pink curves corresponds to 5-CT ligand exchanged NCs with and without rubrene. All measurements were performed in toluene at RT. QDs were excited at 781 nm with 1.43 µW picosecond laser. The repetition rate was set to 31.3 kHz. The optical density of the QDs at the excitation wavelength was between 0.2 and 0.6.

4.1.2 Native Oleic Acid (OA) capped QDs mixed with rubrene

We calculated the rate of TET from 3 distinct models: 1) The photon upconversion QY measurements; 2) The steady-state NC PL quenching in the presence of rubrene; and 3) The changes in NC lifetime as reflected by TCSPC measurements in the presence and absence of rubrene. The results of these models are given in Table 2. Note that here, when the OA capped NCs are mixed with 20 mM rubrene, no additional decay pathways rather than the intrinsic radiative and non-radiative decay and TET after mixing with rubrene is considered. In contrast, in Section 1.3, in the presence of the 5-CT transmitter ligand, an additional decay pathway reflecting the surface reconstruction is included.

4.1.2.1 The rate of TET from the Photon Upconversion QY

The efficiency of TET, Φ_{TET}, can be calculated from the steady state photon upconversion QY measurement (Equation 3). Here Φ_{TTA}=0.33, and Φ_{Rub}=0.98.

(3): $\Phi_{\mathrm{Upconversion}}=\Phi_{\mathrm{TET}}\cdot\Phi_{\mathrm{TTA}}\cdot\Phi_{\mathrm{Rub}}$

The rate of TET can be calculated from Equation 4 below, assuming the presence of rubrene doesn't affect the intrinsic lifetime of the NC triplet photosensitizers, calculated in Table 1 from the NC PL QY and TCSPC measurements.

(4): $\Phi_{\mathrm{TET}}=\frac{k_{\mathrm{TET}}}{k_{r}+k_{nr}+k_{\mathrm{TET}}}$

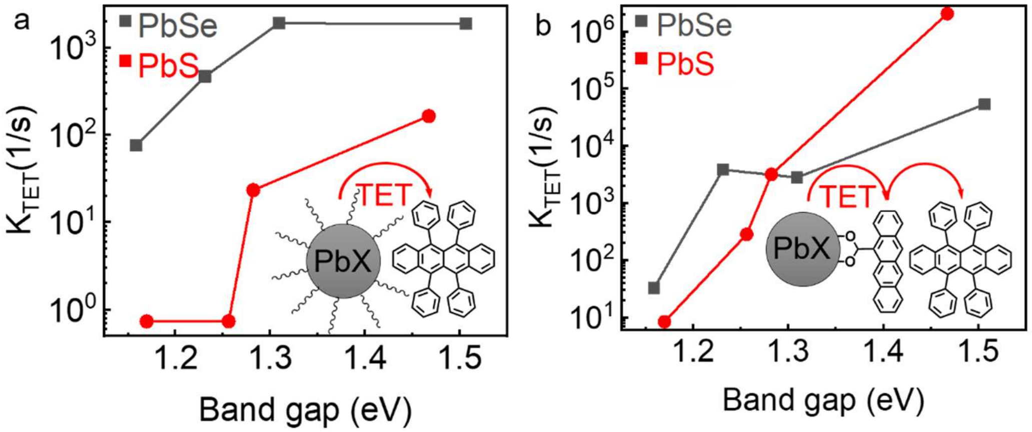

Figure 4.4. The logarithmic rate of triplet energy transfer (k_{TET}) from (a) oleic acid capped and (b) 5-CT ligand exchanged PbX (X=S and Se) NCs to rubrene versus the NCs band gap (calculated from absorption maxima). For oleic acid capped NCs, k_{TET} is calculated from Equation 3 and 4 (Model 1). For the 5-CT ligand exchanged NCs, k_{TET} is measured from upconversion QY and PL QY of the 5-CT ligand exchanged NCs.

4.1.2.2 TET rate from NC PL quenching

k_{TET} and hence the photon upconversion QY can also be calculated from the decrease in NC PL in the presence of 20 mM rubrene as follows:

(5): $\mathrm{PL\ QY\%}=\frac{k_r}{k_r+k_{nr}+k_{TET}}$

Here, PLQY is from the PL of the NCs after mixing with rubrene and k_r and k_{nr} are the intrinsic radiative and non-radiative decay obtained from Table 1. As can be seen from Table 1 and Fig. S9. The presence of rubrene does not affect PbS, but quenches PbSe PL significantly, with up to 30% quenching for the smallest PbSe NC photosensitizers.

Table 4.2. Lifetimes obtained from TCSPC photoluminescence (PL) measurements of oleic acid capped NCs with 0 and 20 mM rubrene. k_{TET} from oleic acid capped NCs to rubrene calculated following different models stated in section 1.2. All measurements were performed in toluene at RT.

Sample	No rubrene		With rubrene		k_{TET} calculated by different models		
	τ_1 (μs)	τ_2 (μs)	τ_1 (μs)	τ_2 (μs)	Sec. 1.2.1 ($\times 10^4$ 1/s)	Sec. 1.2.2 ($\times 10^6$ 1/s)	Sec. 1.2.3 ($\times 10^6$ 1/s)
PbS-845-O	7.36		6.190		0.01641		0.0257
PbS-967	5.42		5.055		0.00234	0.00683	0.0133
PbS-987	3.54		3.152		7.32×10^{-5}	0.00250	0.0348
PbS-1060	3.46	0.512	3.37	0.467	7.31×10^{-5}	0.01744	0.686
PbSe-823	6.04		6.037		0.18771	0.07239	8.23×10^{-5}
PbSe-947	3.87		3.865		0.18925	0.03015	3.34×10^{-4}
PbSe-1007	3.52	0.0447	2.938	0.0437	0.04674	0.05245	22.5
PbSe-1070	3.31	0.0638	3.043	0.0722	0.00764	0.05728	12.1

4.1.2.3 TET rate from NC PL decay with and without rubrene

The smaller OA capped PbSe and PbS NCs decay monoexponentially while the larger ones biexponentially. In the presence of 20 mM of rubrene no additional decay is added and QDs decay lifetime does not change considerably (see figure 3. and Table 2). This is due to very low TET efficiency from oleic acid capped QDs to rubrene.

The decay of NCs mixed with rubrene can be fit as follow:

(6): $f(t) = b_1.\exp[-(1/\tau_1)t]+b_2.\exp[-(1/\tau_2)t]$

Where:

$1/\tau_1 = k_r + k_{nr} + k_{TET1}$, and $1/\tau_2 = k_r + k_{nr} + k_{TET2}$, $<\tau_{NC}> = \frac{b_1.\tau_1+b.\tau_2}{b_1+b_2}$

The amplitude averaged rate of TET, $<k_{TET}>$ can be calculated as follow and is given in Table 2.

(7): $<k_{TET}>=(b_1 .\ k_{TET1}+ b_2 .\ k_{TET2}) (\frac{1}{b_1+b_2})$

Table 4.3. Upconversion QY and parameters obtained from fitting kinetics traces of oleic acid capped NCs mixed with 20 mM rubrene.

Sample	τ_1 (μs)	b_1	τ_2 (μs)	b_2	$<\tau_{NC}>$ (μs)	UC QY (%)
PbS-845-O	6.190	1			6.190	0.039
PbS-967	5.055	1			5.055	0.0041
PbS-987	3.152	1			3.152	0.000084
PbS-1060	3.37	0.649	0.467	0.394	2.273	0.0000768
PbSe-823	6.037	1			6.037	0.3616
PbSe-947	3.865	1			3.865	0.2355
PbSe-1007	2.938	0.654	0.0437	186.2	0.054	0.0435
PbSe-1070	3.043	0.670	0.0722	5.637	0.388	0.0074

We note that the k_{TET} calculated from upconversion QY is lower than the k_{TET} calculated from PL quenching. Perhaps the value of Φ_{TTA}=0.33 used here obtained from literature is not appropriate. The k_{TET} calculated for small PbS and PbSe to rubrene are 164 1/s and 1877 1/s from Model 1 (Section 1.2.1). A comparable method for obtaining k_{TET} from the photon upconversion QY and NCs PL lifetime decay for visible upconversion using ODPA capped CdSe QDs as the absorber and DPA as the annihilator is around 445.8 1/s ($\ln k_{TET}$~6.1). This value is obtained from time-resolved photoluminescence measurements of CdSe NCs.

4.1.3 5-CT ligand exchanged QDs

4.1.3.1 TET rate calculated using 5-CT ligand exchanged capped NCs PL decay lifetime

After 5-CT ligand exchange, the 3.16, 3.24, 3.54 nm diameter PbS QDs decays are best fit with a triexponential while rest of the QDs after ligand exchange decay biexponentially. Thus after ligand exchange, we assume there are 2 or 3 different TET rates of k_{TET1}, k_{TET2}, and k_{TET3} from NC to 5CT. Decay of the ligand exchanged QDs can be expressed as follows:

(8): $f(t) = c_1.\exp[-(k_r + k_{nr} + k_{TET1})t]+c_2.\exp[-(k_r + k_{nr} + k_{TET2})t]+c_3.\exp[-(k_r + k_{nr} + k_{TET3})t]$

k_r and k_{nr} are the intrinsic radiative and non-radiative decay rates obtained from Table 1. TET efficiency can be calculated considering the amplitudes obtained from the biexponential or triexponential PL decay of 5-CT ligand exchanged NCs as follows:

(9): $\Phi_{TET}= (c_1\frac{k_{TET1}}{k_r+k_{nr}+<k_{TET}>}+c_2\frac{k_{TET2}}{k_r+k_{nr}+<k_{TET}>}+c_3\frac{k_{TET3}}{k_r+k_{nr}+<k_{TET}>})(\frac{1}{c_1+c_2+c_3})$

$<k_{TET}>$ is the amplitude averaged rates of TET. In this model we assume k_r and k_{nr} of NCs after ligand exchange is constant and no additional decay rate rather than TET is introduced or in other words ligand exchange does not introduces any trap states.

QDs are indeed sensitive to the ligand exchange and this model cannot appropriately explain the kinetic traces of 5-CT functionalized QDs. For example k_{TET1} is either negative or it is very small for most of the QDs (see following Table). Also, the upconversion QY calculated by this model is higher than the measured upcpnversion QY. Thus it is essential to consider an additional intrinsic non-radiative decay rate, k_{COOH}, for 5-CT ligand containing QDs that does not contribute to TET.

Table 4.4. Parameters obtained from fitting of photoluminescence (PL) kinetics traces of 5-CT ligand exchanged QDs and TET rate and upconversion QY calculated from NCs PL decay fits (equation 8 and 9).

Sample	τ_1 (μs)	c_1	τ_2 (μs)	c_2	τ_3 (μs)	c_3	k_{TET1} (1/s×10^6)	k_{TET2} (1/s×10^6)	k_{TET3} (1/s×10^6)	$<k_{TET}>$ (1/s×10^6)	UC QY (%)
PbS-845-O	8.60	0.667	0.057	3.955			-0.0196	17.3		14.8	32.0
PbS-967	4.19	0.491	0.297	0.338	0.0280	30.1	0.0542	3.18	35.6	34.7	32.2
PbS-987	3.51	0.394	0.345	0.343	0.0283	3.1	0.00218	2.62	35.1	28.5	32.0
PbS-1060	2.80	0.268	0.304	0.527	0.0236	715	0.0496	2.98	41.9	41.9	32.1
PbSe-823	5.06	0.714	0.233	0.444			0.0319	4.13		1.6	29.3
PbSe-947	4.80	0.642	0.638	0.257			-0.0501	1.31		0.338	18.3
PbSe-1007	3.66	0.632	0.230	0.273			-0.0739	3.99		1.15	24.9
PbSe-1070	3.38	0.608	0.222	0.460			-0.0383	4.18		1.78	27.2

τ_1, τ_2, τ_3 are the decay lifetimes obtained from PL decay of 5-CT ligand exchange QDs following equation 8 decay model where, $\tau_i=\frac{1}{k_r+k_{nr}+k_{TETi}}$, c_1, c_2, and c_3 are the amplitudes lifetime; k_{TET1}, k_{TET2}, and k_{TET3} are the triplet energy transfer decay rates obtained from PL decay fitting of 5-CT ligand exchanged QDs following equation 8; UC QY= upconversion quantum yield calculated from $<k_{TET}>$ following Model 3 (section 1.2.3). All measurements were in toluene at RT.

4.1.3.2 The rate of TET calculated from steady state measurements

The PL QY of the QDs after 5-CT ligand exchanged can be expressed by following equation (10)

(10): $\text{PL QY\%}=\frac{k_r}{k_r+k_{nr}+k_{TET}+k_{COOH}}$

k_{TET} is the TET rate from NCs to 5-CT. k_r, k_{nr} are the intrinsic radiative and nonradioactive decay rates of the NCs obtained from Table 1. Due to introduction of the trap states during ligand exchange, an additional decay rate of k_{COOH} is introduced. This additional decay rate does not contribute to the TET from NC to 5-CT, hence TET efficiency can be written as follows:

(11): $\Phi_{TET}=\frac{k_{TET}}{k_r+k_{nr}+k_{TET}+k_{COOH}}$

Φ_{TET} can be calculated from the photon upconversion QY (equation 3) assuming 100% TET from 5-CT to rubrene. Since we measured the PL QY of the NCs after ligand exchange, k_{TET} and k_{COOH} can be calculated from equation 10 and 11. The results is given in Table 5.

Table 4.5. Key parameters for 5-CT ligand exchanged QDs obtained from steady state photoluminescence (PL) quantum yield (QY), upconversion QY and intrinsic decay lifetime measurement.

Sample	PL QY[a] (%)	PL Quenching (%)	UC QY[a] (%)	k_{TET} ($1/s\times10^6$)	k_{COOH} ($1/s\times10^6$)
PbS-845-O	0.20	97.8	11.2	2.040444	3.8235
PbS-967	8.5	64.1	0.203	0.0031834	0.328
PbS-987	5.2	63.6	0.012	0.0002803	0.487
PbS-1060	3.3	71.0	0.00026	0.0000084	0.753
PbSe-823	5.4	77.2	2.398	0.0531260	0.510
PbSe-947	8.0	22.8	0.2794	0.0028102	0.070
PbSe-1007	6.1	37.2	0.0228	0.0038359	0.207
PbSe-1070	5.7	37.3	0.002	0.0000326	0.203

[a)] In toluene and room temperature. PL QY= photoluminescence quantum yield (QY) of the 5-CT ligand exchanged QDs. QDs were excited at 700 nm in toluene at RT with ICG in DMSO used as standard. PL Quenching= percent ratio of PL QY of the QDs before and after 5-CT ligand exchange, UC QY= upconversion QY of 5-CT ligand exchanged QDs, k_{TET} = triplet energy transfer rate, k_{COOH}= additional intrinsic non-radiative decay rate induced due to 5-CT ligand exchanged. k_{TET} and k_{COOH} calculated from equation 10, 11, knowing upconversin QY and PL QY of the QDs after 5-CT ligand exchange.

As shown in Fig. 2 and Table 5, upon functionalization with 5-CT, the photon upconversion QYs are comparable for both PbS and PbSe NC photosensitizers. The highest photon upconversion QY of 2.4% is obtained for the smallest PbSe NCs. The higher covalency in the PbSe compared to PbS translates into a lower stability in the laboratory, as reflected in more substantial drops in photoluminescence QYs and particle ripening. perhaps because the surface of the PbSe NCs are more reactive. Furthermore, Table 5 shows that the ligand exchange procedure does induce a large non-radiative decay pathway, even though both OA and 5-CT share the same carboxylic acid functional group for binding to the NC. More work needs to be done to decreases k_{COOH} to improve the photon upconversion QY.

4.2 FTIR study of the NCs

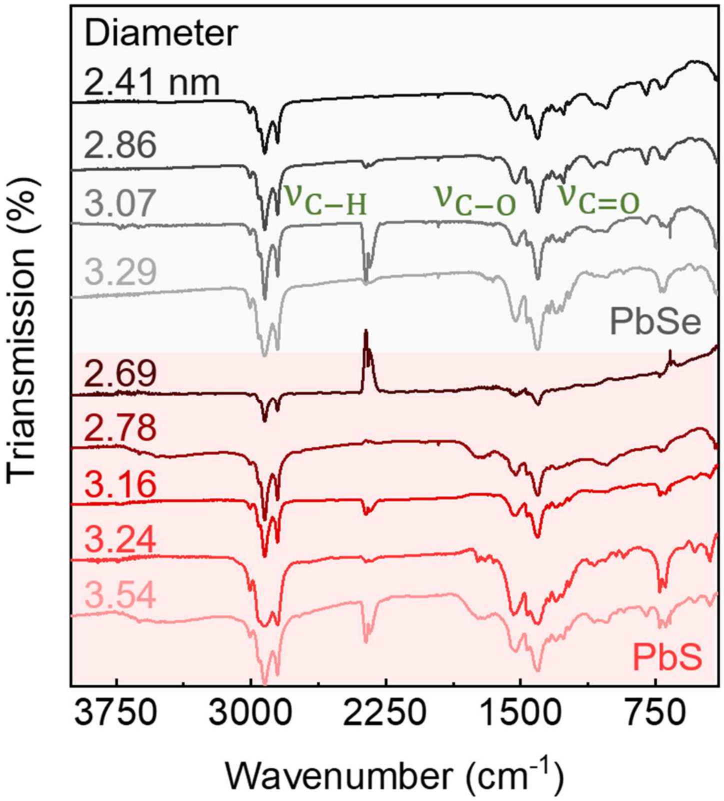

Figure 5.5. Infrared spectra of differently sized oleic acid capped PbS and PbSe NCs. NCs were cleaned 3 times with hexane and ethanol mixture after synthesis for FTIR and all other measurements. FTIR of the NCs were taken air free in solid state on KBr plates.

4.3 NMR study of the NCs

4.3.1 Ligand identification and quantification

We used proton NMR in solution to investigate the OA ligands on the NCs. This data shows that the OA ligand densities obtained here by NMR here vary from 1 to 50 nm^{-2}. On average, these ligand densities are a little higher than the reported oleic acid ligand densities for PbSe and PbS at 4.2 nm^{-2} and 3 to 5.3 nm^{-2} respectively.

The surface density of oleic acid ligand on PbS845 synthesized with Owen's method is 6 times higher than the PbSe820 NCs. When the ligand density is high rubrene cannot diffuse through the ligand shell and ligand shell is a barrier for energy transfer from NCs to rubrene. Since the efficiency of Dexter energy transfer decreases exponentially with increasing donor-acceptor distance, excess ligand may dramatically affect the upconversion QY. This may explain why oleic acid capped PbSe NCs show higher upconversion QY.

No size dependence is observed with surface ligand density. First, though these particles are cleaned more than three times, both free and bound ligands are still in solution. Second, estimations of the NC size is not accurate for the range studied and thus the sizing curves use to determine surface area have large errors in this size regime. While cleaning for both PbS and PbSe is the same (hexane: ethanol (1:1 volume)), the different amounts of OA added during PbSe NC synthesis, and the different temperatures used for PbS synthesis means different amounts of polymerization of OA might occur, and thus be differently removed.

Table 4.6. Ligand density for the PbS and PbSe QDs used for upconversion Quantum yield measurement was measured by 1H NMR.

QD-Abs maxima[a] (nm)	Synthesis method	NC diameter (nm)	Upconversion QY[a] (%)		Density ($1/nm^2$)
			Oleic acid	5-CT	
PbS- 845	(1)	2.69	0.039	11.2	51.0
PbS-868	(2)	2.78	0.0139	2.191	1.0
PbS-967	(2)	3.16	0.0041	0.203	9.8
PbS-987	(2)	3.24	0.000084	0.012	12.8
PbS-1060	(2)	3.54	0.0000768	0.00026	14.8
PbSe-823	(3)	2.41	0.3616	2.398	8.2
PbSe-947	(3)	2.86	0.2355	0.2794	10.3
PbSe-1007	(3)	3.07	0.0435	0.0228	9.5
PbSe-1070	(3)	3.29	0.0074	0.002	34.2

[a)] In toluene and room temperature. Ligand density was measured by solution 1H NMR with ferrocene standard in toluene-d_8.

In conclusion, our NMR study on the PbS and PbSe NCs shows that there is no direct correlation between the upconversion QY and ligand density of the PbSe NCs and PbS NCs. For example both oleic acid capped PbS synthesized with different method (2.69 and 2.78 nm in diameter) shows lower upconversion QY than the 2.42 nm in dimeter oleic acid capped PbSe NCs while 2.69 nm in diameter PbS synthesized following Owen et al. has 6 times higher ligand density and 2.78 nm in diameter PbS synthesized following Scholes et al. has 8 times lower ligand density compared to 2.42 nm in dimeter PbSe.

4.4. Experimental section

4.4.1 Materials

Lead oxide (PbO, 99.999%), oleic acid (OA, tech. grade, 90%), and 1-octadecene (ODE, 90%), bis(trimethylsilyl) sulfide ($(TMS)_2S$), dibutylamine (99.5%), dodecylamine (98%), Diethylene glycol dimethyl ether ("diglyme", anhydrous, 99.5%) were purchased from Aldrich. Bis(trimethylsilyl) selenide ($(TMS)_2Se$) was acquired from Gelest Inc. Dry ethanol was obtained from Sigma-Aldrich, while dry and degassed toluene was obtained from JC Meyer's solvent purification system.

4.4.2 FTIR sample preparation of oleic acid capped PbX (X=S and Se) QDs

About 10 ul of the NCs in toluene with concentration of around 200 μM were drop casted on 4mm KBr windows (Pike Technologies) and were let to dry. Then NCs were sandwiched between two KBr windows in a glovebox and measured air free in solid state.

4.4.3 NMR of oleic acid capped PbX (X=S and Se) QDs

NMR samples were prepared by addition of known amount of PbS and PbSe QDs of approximately 8×10^{-8} moles to 10 μl of 8.239 mM ferrocene as an ^1H NMR internal standard with a peak at 4.00 ppm in acetone. Solvents evaporated by 150 millitorr vacuum. Then toluene-d_8 added to redisperse the NCs in toluene. Proton NMR (1H) spectra was recorded on Bruker Advance NEO 400 MHz.

4.4.4. Photon Upconversion

4.4.4.1 Instrumentation

Absorption spectra were recorded on a Jasco-V670 UV-Vis absorption spectrophotometer. Fluorescence spectra were recorded on a QuantaMaster 400– HORIBA at the usual 90 degrees, or in a front face setup at a 70 degree angle to the excitation with a NIRS-0900-1700 Bayspec fluorometer. When using the front face setup, a Coherent Sapphire 781 nm laser (OBIS) with an output power of 10.0 mW was used for excitation. For the QuantaMaster 400– HORIBA, the excitation wavelength was set to 700nm. NMR spectra were recorded on a Bruker Advance NEO 400 MHz at room temperature.

4.4.4.2 Upconversion QY measurement and calculation

Photon upconversion spectra were recorded in the front face geometry at 70 degrees to the excitation. The Coherent Sapphire 781 nm laser is focused by a lens (focal length of 10 cm) to a spot size with radius of 374.1 μm. A 745 nm short-pass filter (FF01-745/SP-25 Semrock BrightLine multiphoton) and 488 nm notch filter (NF01-488U-25 Semrock) were used to block the scattered laser light. The upconverted light is focused by a lens (focal length of 25.4 mm N-BK7 plano-convex lens) into a PAF-SMA-11-A (Thor Laboratories) fiber port connected to an Ocean Optics QP600-2-VIS-NIR fiber. Finally, the upconverted light was detected by Maya2000Pro-Ocean Optics. A 100 μm thick capillary tube (LRT-010–2–10 Friedrich & Dimmock, Inc.) inside an air-free cuvette for holding the sample was used for front face detection. This prevents the parasitic reabsorption of the upconverted light. We calculated the upconversion QY from the following equation:

$$\Phi_{\text{upconversion}}=2\Phi_{\text{ref}}\times\frac{\text{Photons absorbed by reference}}{\text{photons absorbed by sample}}\times\frac{\text{Photons emitted by sample}}{\text{Photons emitted by reference}}$$

$$\text{Photon absorbed/s}=\frac{P\lambda}{hc}(1\text{-}10^{\text{-Abs}})$$

488 nm Coherent Sapphire (OBIS) and 785 nm Coherent Sapphire (OBIS) lasers were used for exciting the reference sample (here rubrene) and upconversion samples. Note

that absorption at the excitation wavelength for both the reference and upconversion samples is kept same.

If we consider the possible errors in upconversion detection, laser power and background, the error in upconversion QY can be roughly calculated to be 0.5×10^{-5} %.

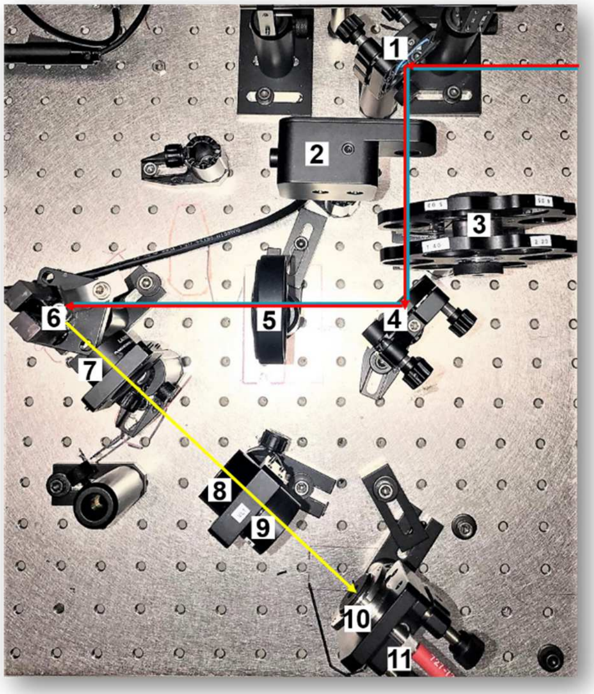

Figure 4.6. Photo of the near-infrared photon upconversion setup

Table 4.7. The optical parts used in the near-infrared photon upconversion setup

Numbers[1]	Part number	Product name
1	BB1-E02	broadband dielectric mirror[2]
2	SH05	optical beam shutter[2]
3	FW2A	filter wheel station with ND filters[2]
4	BB1-E02	broadband dielectric mirror[2]
5	LA1050	plano-convex lens[2]
6	Hand made	sample holder
7	N-BK7	plano-convex lens[2]
8	FF01-745/SP-25	745 nm short-pass filter[3]
9	NF01-488U-25	488 nm notch filter[3]
10	PAF-SMA-11-A	SMA fiber port[2]
11	QP600-2-VIS-NIR	optical fiber[4]

[1] Numbers from figure1. [2]Thorlabs. [3]Semrock. [4]Ocean Optics.

4.4.4.3 Time correlated single photon counting (TCSPC) measurements

PL decay lifetimes were recorded with the Picoharp 300. The QDs were excited by femtosecond laser system (PHAROS, Light Conversion) pumping an optical parametric amplifier and second harmonic generator (ORPHEUS/LYRA, Light Conversion) at 480 nm with a 1.437 μW pump at a repetition rate of 35.7 kHz. We controlled the excitation intensity variable neutral density filters. The excess bias, gate width, gate frequency, hold-off time, and time resolution was set to 2.0V, 230.00 ns, 2 MHz, 30 μs, and 512 ps respectively. The rising point was assigned to zero. Signal was detected by a 512 channel

InGaAs/InP Single-Photon Avalanche Diode (quasi free-running mode with gated module, Micro Photon Devices S.r.l.). For sample preparation, we dissolved QDs in oxygen-free anhydrous toluene. The optical density of the QDs samples at excitation wavelength was between 0.2 and 0.6. The decay lifetimes were fitted either monoexponential or biexponential decay function

4.4.4.4 Relative PL QY measurements and calculations

For PL QY measurements we either excite the samples with 700 nm and record the PL with PTI QuantaMaster 400– HORIBA in 90 degree detection or we excite them with 781 nm laser and record with Bayspec fluorometer in front face PL measurement.

NCs were measured in anhydrous oxygen-free toluene in 3.5 mL air-free, quartz Starna cuvettes and 5.4 μM indocyanine green (ICG) dye in anhydrous dimethyl sulfoxide was used as a PL QY reference. At this concentration ICG has a known PL QY of 12 % in dimethyl sulfoxide. Note that the PL QY of the ICG depends on the ICG concentration. Excitation wavelength was set to 781 or 700 nm. For right angle detection with the PTI QuantaMaster 400– HORIBA, absorption at excitation wavelength (700 nm) for ICG and all the QD samples were less than 0.1 while for front face measurement and detection with the Bayspec fluorometer, absorption at excitation wavelength (781 nm) of ICG samples and QDs were similar and less than 0.4. For calculation of the relative PL QY, the area under the curve for the PL normalized by number of absorbed photon as follows:

Photon absorbed/s= $\frac{P\lambda}{hc}(1\text{-}10^{-Abs})$

Where P is the laser power, λ is the excitation wavelength, h is Planck's constant, c is the speed of light, and Abs is the sample absorption at excitation wavelength.

Chapter 5 High quality QDs are essential for efficient triplet photosensitization

Quantum dots are typically depicted as nanostructures with a perfect single crystalline domain. The colloidal synthesis of such nanostructures, in combination with transmission electron microscopy, have allowed the quantum confined excitonic states to be correlated with size. It has been argued that these colloidal syntheses expel impurities to the surface and thus induce a self-purification of the QD, resulting in a kinetically stable structure. However, it is also well-established that chemical perturbations to the QD surface drastically modify QD photophysics, not by changing the electronic band structure but by introducing surface defects, quenching sites or trap states.

In this chapter, we attempt to explain our observation that PbS NCs synthesized with thiourea sulfur precursors give the highest photon upconversion QYs of 12-15 % thus far for the NIR to yellow photon upconversion, a factor of two higher than with sulfide precursors. We were compelled to use Owen's thiourea based sulfur precursor in combination with lead oleate due to the fact that Sigma Aldrich could no longer supply 99.999% purity PbO, and that the synthesis of PbS QDs with PbO from other chemical suppliers with the same nominal purity failed. Here, we try to isolate the physical reasons for the disparities in what is ostensibly the same material with x-ray photoelectron spectroscopy and FTIR.

In addition, we also show that the threshold intensity between the quadratic and linear regime, a parameter used to describe the efficiency of energy transfer between molecular triplet photosensitizers and acceptors, is no longer a good metric for QDs. This is because the small exchange energy far less than kT of 26 meV at RT results in rapid equilibration between excitons with singlet and triplet character on Cd and Pb chalcogenide QDs, and thus triplet energy transfer competes with radiative decay.

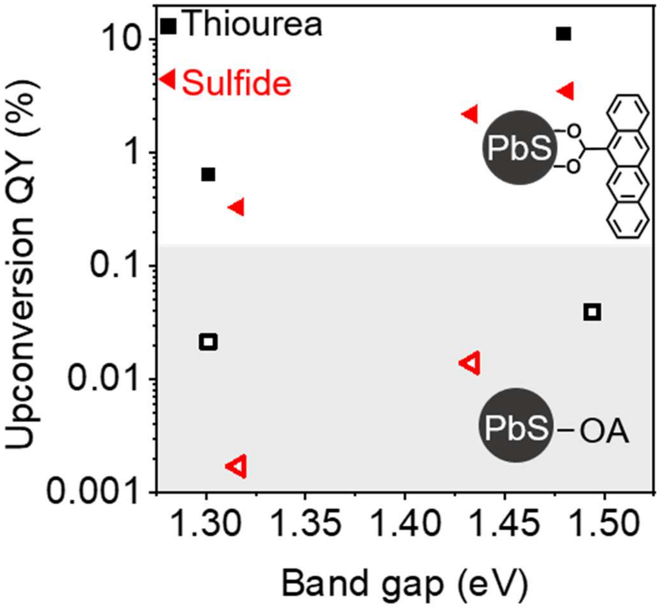

Figure 5.1. The effect of nanocrystal (NC) synthesis precursor on the upconversion of NIR light to visible light is shown. For both oleic acid capped and 5-CT ligand exchanged NCs using thiourea precursors (black squares), a higher photon upconversion quantum yield is obtained as compared to sulfide precursors (red triangles). All measurements were performed in toluene at RT. Rubrene and NCs concentration was kept 20 mM and 10 µM respectively. NCs were excited with 40 W/cm^2 781 nm laser.

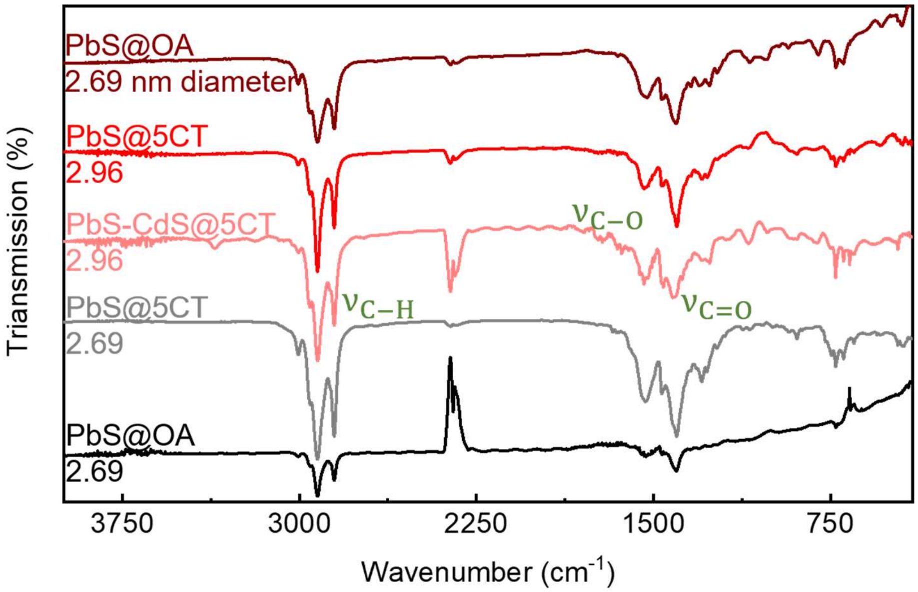

Figure 5.2. Infrared spectra of 2.69 nm diameter PbS core NCs synthesized using thiourea precursors and 2.96 nm in diameter PbS core and PbS-CdS core-shell NCs using sulfide precursor before and after 5-CT ligand exchange. All PbS core NCs were cleaned 3 times with hexane and ethanol mixture after synthesis while PbS-CdS core-shell NCs were cleaned 1 time with acetone and 3 times with methanol. After 5-CT ligand exchange PbS cores were cleaned with acetone while PbS-CdS core-shell were cleaned with methanol. FTIR of the NCs were taken air free in solid state on KBr plates at RT.

5.1 XPS composition analysis

After ligand exchange with 5-CT, the ratio of oxygen to lead increases. We believe the introduced oxygen is due to the addition of more than one 5-CT to the NC surface per removal of one oleic acid from the NCs surface during ligand exchange because the elemental analysis showed that 5-CT and OA have around the same proportions of oxygen to carbon, e.g. 5-CT has O:C = 11.75: 83.81 and OA has O:C = 11.33: 76.54. One 5-CT introduces the same amount of oxygen as OA. Therefore, during ligand exchange addition of 5-CT is more than the number of oleic acid removed from the NCs surface. Note that all the NCs were treated similarly in glovebox with oxygen less than 1 ppm. For ligand exchange, 15μl of 5 mM 5-CT in THF: toluene (volume 1:10) added to the NCs solution and after ligand exchange NCs cleaned with acetone. Knowing that additional cleaning steps will remove excess free oleic acid ligand in the solution. After cleaning with acetone NCs were dissolved in toluene and were spin coated and then dried by solvent evaporation. Also due to high vacuum during XPS measurement any solvents will evaporate. All in all, we believe the only introduced oxygen is due to 5-CT addition.

Table 5.1. Elemental composition of the oleic acid capped and 5-CT ligand exchanged PbS NCs synthesized using thiourea and sulfide precursor.

Abs maxima (nm)	Precursor	Ligand	XPS composition (atomic %)				
			Pb	S	C	O	O/Pb
838	Sulfide	5-CT	7.43	6.28	75.97	10.32	1.39
865	Thiourea	5-CT	7.04	5.80	69.89	14.28	2.03
953	Sulfide	5-CT	6.63	5.45	76.53	11.38	1.72
830	Sulfide	Oleic acid	7.81	7.85	77.54	6.79	0.87
865	Thiourea	Oleic acid	6.62	6.33	80.62	6.43	0.97
953	Sulfide	Oleic acid	7.56	6.47	79.18	6.69	0.88
942	Thiourea	Oleic acid	7.23	5.75	81.1	5.93	0.82

5.2 Hybrid molecule–nanocrystal photon upconversion dynamics

The dynamics of hybrid molecule–nanocrystal photon upconversion can be described as follow (see figure 2a):

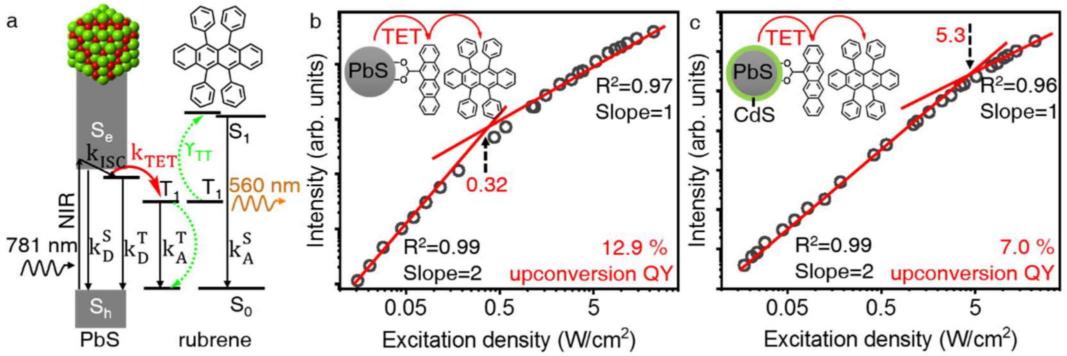

Figure 5.3. (a) Schematic of the energy transfer in this hybrid photon upconversion platform. Log–log plot of the upconversion signal measured in capillary tube versus excitation power density for (b) 2.69 nm in diameter PbS core synthesized with thiourea precursors, and (c) 2.96 nm in diameter PbS-CdS core-shell with absorption maxima of 890 nm synthesis from PbS core with absorption maxima of 915 nm synthesized using sulfide precursors. These graphs show the transition from the quadratic (slope = 2) to the linear (slope = 1) regime. Optical density (OD) of the NCs at excitation wavelength for (b) was 0.07182 while OD for (c) was 0.00326. NCs were excited with a 781 nm laser in toluene at RT. Rubrene concentration was kept 20 mM. The native long chain aliphatic oleic acid ligands were partially replaced with the 5-CT transmitter ligand.

Since the intersystem crossing (ISC) efficiency in the NCs is not 100%, we cannot assume that all the photogenerated singlets are converted to triplet-like excitons, e.g. in the palladium porphyrin triplet photosensitizers. The exchange energy for PbS is 1-10 meV. The rate of change of S_D, the population of NCs at the singlet excited state, is given by the number of photons per second arriving on the sample (I_{exc}) multiplied by the NC absorption coefficient α(E).

$$\frac{\partial S_D}{\partial t} = \alpha(E) I_{exc} - k_D^S S_D - k_{ISC} S_D \tag{1}$$

k_D^S and k_{ISC} are the rates of decay for the singlet exciton on the NC and ISC respectively.

The spin-triplet NCs excitons can decay with a rate k_D^T, or transfer energy to rubrene with a rate k_{tr}. Here, T_D, is NC population at excited triplets.

$$\frac{\partial T_D}{\partial t} = k_{ISC}S_D - k_D^T T_D - k_{tr}T_D \tag{2}$$

Rubrene triplet states can decay non-radiatively with a rate k_A^T or annihilate with a probability proportional to γ_{TT}. Note that TTA is the second-order rate process hence annihilation probability is proportional to the square of rubrene population at excited triplet, T_A.

$$\frac{\partial T_A}{\partial t} = k_{tr}T_D - k_A^T T_A - \gamma_{TT}T_A^2 \tag{3}$$

Then rubrene singlet states formed from the TTA process with probability depend on γ_{STT}. Note that γ_{STT}, is proportional to γ_{TT}. ***f*** is the spin-statistical weight of the singlet excited-state generation from a TTA process. Finally, the singlet excited state on rubrene, S_A, decays with rate k_A^S to generate upconversion emission.

$$\frac{\partial S_A}{\partial t} = 0.5\gamma_{TT}^S T_A^2 - k_A^S S_A = 0.5f\gamma_{TT}T_A^2 - k_A^S S_A \tag{4}$$

5.3 Photon upconversion dependence on excitation density under steady-state conditions.

At low excitation densities rubrene triplet decay becomes the main deactivation channel while at high excitation TTA which is a second order process becomes the main deactivation channel for rubrene triplet. Hence, the logarithmic plot of $I_{rubrene}$ vs I_{exc} changes the slope from 2 to 1. The threshold excitation density (I_{th}) at which $k_A^T T_A \ll \gamma_{TT}T_A^2$ is interesting as it denotes the threshold for maximum upconversion QY. I_{th} can be calculated as follow:

The upconverted PL signal is proportional to the population of rubrene excited singlet states. Hence in order to calculate I_{th}, we will find S_D in terms of I_{exc}:

At steady state:

$$\frac{\partial S_D}{\partial t} = \frac{\partial T_D}{\partial t} = \frac{\partial T_A}{\partial t} = \frac{\partial S_A}{\partial t} = 0 \tag{5}$$

hence, S_D can be found from equation 1 in terms of $\alpha(E)$, I_{exc}, k_{ISC}, k_D^S.

$$S_D = \frac{\alpha(E) I_{exc}}{k_D^S + k_{ISC}} \tag{6}$$

Then population of NC in the spin-triplet excited state can be found from equation (2), (5), and (6)

$$k_{ISC} S_D - k_D^T T_D - k_{tr} T_D = 0 \rightarrow T_D = \frac{k_{ISC} S_D}{k_D^T + k_{tr}} = \frac{k_{ISC}}{k_D^T + k_{tr}} \times \frac{\alpha(E) I_{exc}}{k_D^S + k_{ISC}} \tag{7}$$

a) When rubrene TTA is much more probable than the triplets decay ($k_A^T T_A \gg \gamma_{TT} T_A^2$)

From (3), and (5)

$$k_{tr} T_D - k_A^T T_A = 0 \rightarrow T_A^2 = [\frac{k_{tr} T_D}{k_A^T}]^2$$

Then from equation 7, T_A^2 can be calculated:

$$T_A^2 = [\frac{k_{tr}}{k_A^T} \frac{k_{ISC}}{k_D^T + k_{tr}} \times \frac{\alpha(E) I_{exc}}{k_D^S + k_{ISC}}]^2 \tag{8}$$

The S_A population can be expressed in terms of T_A using equation (4) and (5)

$$0.5 f \gamma_{TT} T_A^2 - k_A^S S_A = 0 \rightarrow S_A = \frac{0.5 f \gamma_{TT} T_A^2}{k_A^S} \rightarrow$$

Finally from (8) $S_A = \frac{0.5 f \gamma_{TT}}{k_A^S} \times [\frac{k_{tr}}{k_A^T} \frac{k_{ISC}}{k_D^T + k_{tr}} \times \frac{\alpha(E) I_{exc}}{k_D^S + k_{ISC}}]^2$ (9)

b) When $k_A^T T_A \ll \gamma_{TT} T_A^2$

From 3 and 5

$$k_{tr} T_D - \gamma_{TT} T_A^2 = 0 \rightarrow T_A^2 = \frac{k_{tr} T_D}{\gamma_{TT}}$$

T_D is replaced from equation 7 and hence

$$T_A^2 = \frac{k_{tr}}{\gamma_{TT}} \times \frac{k_{ISC}}{k_D^T + k_{tr}} \times \frac{\alpha(E) I_{exc}}{k_D^S + k_{ISC}} \tag{10}$$

Using equation 4 and 5:

$$0.5 f \gamma_{TT} T_A^2 - k_A^S S_A = 0 \rightarrow S_A = \frac{0.5 f \gamma_{TT} T_A^2}{k_A^S} \tag{11}$$

Finally S_A can be calculated in terms of I_{exc} using equation 10 and 11,

$$S_A = \frac{0.5 f \gamma_{TT}}{k_A^S} \times \frac{k_{tr}}{\gamma_{TT}} \times \frac{k_{ISC}}{k_D^T + k_{tr}} \times \frac{\alpha(E) I_{exc}}{k_D^S + k_{ISC}} \tag{12}$$

For I_{th} calculation equation 12 and 9 can be solved simultaneously. Therefore, at threshold:

$$\frac{0.5 f \gamma_{TT}}{k_A^S} \times \left[\frac{k_{tr}}{k_A^T} \frac{k_{ISC}}{k_D^T + k_{tr}} \times \frac{\alpha(E) I_{th}}{k_D^S + k_{ISC}}\right]^2 = \frac{0.5 f \gamma_{TT}}{k_A^S} \times \frac{k_{tr}}{\gamma_{TT}} \times \frac{k_{ISC}}{k_D^T + k_{tr}} \times \frac{\alpha(E) I_{th}}{k_D^S + k_{ISC}}$$

and finally I_{th} can be calculated as follow:

$$I_{th} = \frac{1}{\alpha(E) \gamma_{TT}} \times \frac{k_D^T + k_{tr}}{k_{tr}} \times {k_A^T}^2 \times \frac{k_D^S + k_{ISC}}{k_{ISC}} = \frac{{k_A^T}^2}{\alpha(E) \gamma_{TT} \varphi_{tr} \varphi_{ISC}} \tag{13}$$

where φ_{tr} and φ_{ISC} are TET and ISC efficiency. The $\varphi_{tr}\varphi_{ISC}$ product can be calculated from the upconversion QY as follow knowing that the TTA efficiency (Φ_{TTA}) and rubrene PL QY (Φ_{Rub}) are 0.33 and 0.98 respectively.

$$\Phi_{\mathrm{Upconversion}} = \Phi_{\mathrm{ISC}} . \Phi_{\mathrm{tr}} . \Phi_{\mathrm{TTA}} . \Phi_{\mathrm{Rub}} \tag{14}$$

γ_{TT} can also simply be calculated as follow:

$$\gamma_{TT} = 8\pi D a_0 \tag{15}$$

where D is the triplet diffusion coefficient and a_0 is the effective triplet-triplet interaction distance of the annihilator here rubrene. Since D in solution depends on the molecular diffusion, it can be easily calculated from the viscosity of the solvent:

$$D = \frac{kT}{6\pi r_0 \eta} \tag{16}$$

Here k is the Boltzmann constant, r_0 is molecular radius, T is temperature.

Therefore calculating γ_{TT} from equation 15 and $\Phi_{\mathrm{ISC}}.\Phi_{\mathrm{TET}}$ product from equation 14, one can calculate the I_{th}.

Note that this calculation is when a transmitter ligand is not involved in the energy transfer. However, in the presence of the 5-CT transmitter ligand, if we assume 100% TET from transmitter to annihilator this equation is still valid. This is experimentally achieved in our 20 mM rubrene solutions. If the rubrene annihilator concentration is too low, then another Φ_{tr} for TET from 5-CT to rubrene needs to be considered in the I_{th} calculation.

5.4 Experimental section

5.4.1 XPS of PbS QDs

XPS of the oleic acid capped and 5CT ligand exchanged PbS QDs were measured air-free at University of Kentucky directly transferred from the nitrogen filled glovebox into the ultra-high vacuum system so that the QDs were not ever exposed to the atmosphere.

5.4.1.1 XPS sample preparation

ITO substrates were cleaned in 2 mM sodium dodecyl sulfate (SDS) in water. The ITO was washed and sonicated in water for 15 min several times. Then the ITO was washed with first acetone and the isopropanol, sonicated for 15 mins each time. The substrates were dried with nitrogen flow and ozone cleaned for 10 min. PEDOT:PSS was spin coated on the substrate for 30s with 5000 rpm and 1s ramp. Then substrates were annealed for 10 min at 130□ in air. 120 µl of 120 µM NCs were spin coated on the annealed substrates in nitrogen filled glovebox. The substrates were then allowed to dry in the glovebox and were shipped in nitrogen filled packaging overnight for air-free XPS measurements

Chapter 6 Supporting information

6.1 Stern-Volmer quenching experiment

6.1.1 Error in estimating [rubrene]

The error in estimating the rubrene concentrations was calculated based on (i) the error in volume and mass measurements when making the rubrene stock solution, and (ii) the error in volume measurements during the dilutions when preparing the final PbSe/rubrene solutions. The maximum estimated error for all PbSe/rubrene samples was less than ± 0.02 mM.

6.1.2 Error in estimating Stern-Volmer constant

The error for each Stern-Volmer constant was estimated from standard error of the slope when fitting a simple linear regression to the Stern-Volmer graph for each nanocrystal (NC).

6.1.3 PbSe NCs PL with various rubrene concentrations

We used five different batches of PbSe NCs in this study, with sizes from 2.5 nm to 3.2 nm. We varied the concentration of rubrene and fixed the concentration of PbSe NCs by adding various volumes from the stock solutions of rubrene to a fixed amount of NCs and diluting with toluene where necessary. The PbSe NCs photoluminescence (PL) of the samples with various rubrene concentrations from 0.5 to ~7.0 mM is shown in Figure S1. The PL is quenched with increasing concentrations of rubrene.

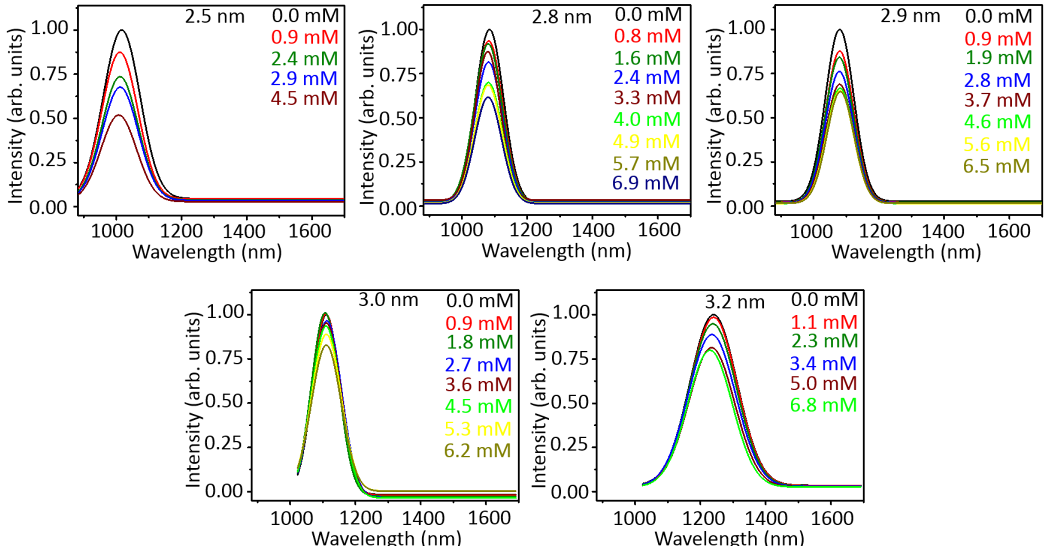

Figure S1.1 Evolution of PbSe NC (2.5 to 3.2 nm in diameter) photoluminescence spectra with different rubrene concentrations. Dexter energy transfer is observed between the PbSe NCs and rubrene. The concentration of the NCs was fixed at 0.5 μM. More PbSe NC PL quenching is observed for smaller NCs in the presence of the same amount of rubrene. Samples were dissolved in dry and degassed toluene, excited at 808 nm at RT.

6.2 PbS-CdS core-shell synthesis

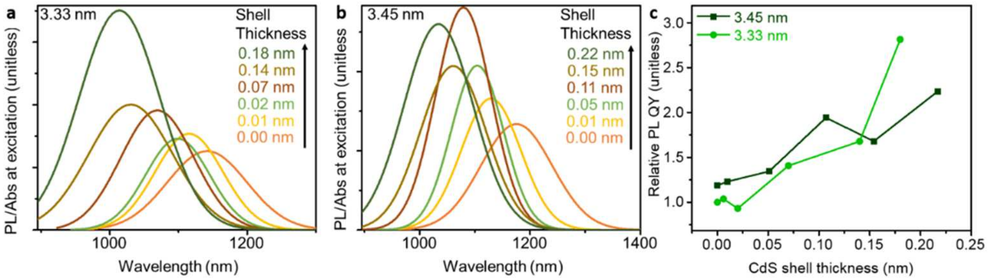

Figure S1. Photoluminescence (PL) spectrum of PbS-CdS core-shell NCs made from **a**, 3.33 nm and **b**, 3.45 nm PbS cores normalized by the optical density of the NCs at the excitation wavelength. As the CdS shell increases, there is a blue shift, and the PL quantum yield (QY) increases. **c**, PbS-CdS core-shell NCs PL QYs from **a** and **b** normalized by the PL QY of 3.33 nm PbS core as the CdS shell thickness increases. All measurements were carried out in toluene and at RT, and a 22 mW/cm^2 808 nm laser diode were used to excite the NCs.

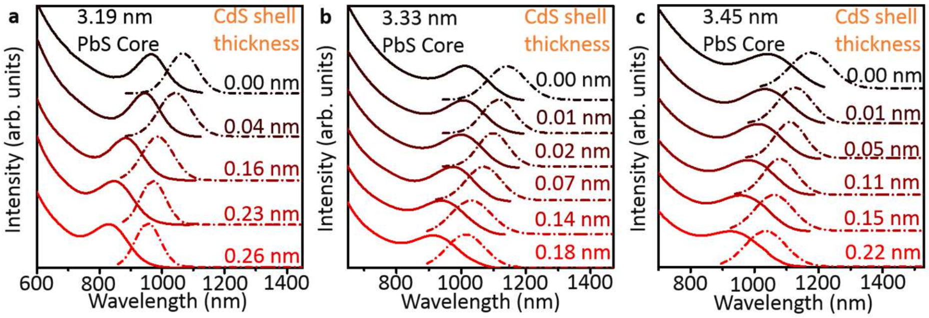

Figure S2. The absorption (solid line) and emission spectrum (dashed-dot line) of PbS-CdS core-shell NCs arising from **a**, 3.19 **b**, 3.33 **c**, 3.45 nm diameter PbS NC cores synthesized via cation exchange. The PbS core contracts as the CdS shell thickness increases, as indicated by the blue shift in the absorption and emission spectra.

Table S1. Results of PbS-CdS core-shell nanocrystals (NCs) synthesized from 3.19 and 3.26 nm PbS NC cores with different reaction times and cadmium acetate concentrations.

3.19 nm PbS core			3.26 nm PbS core		
CdS shell thickness [nm]	Cd-oleate [µl]	Time [min]	CdS shell thickness [nm]	Cd-oleate [µl]	Time [min]
0.04	15	6	0.04	31	7.5
0.16	52	9	0.11	72	10
0.23	152	17	0.2	127	15
0.26	176	19	0.27	200	18
			0.33	303	19

For all synthesis, the PbS core was injected into the specified volume of Cd-oleate solution at 90 °C. After the specified reaction time, the PbS-CdS core-shell NCs were quenched by addition of hexane.

Table S2. Results of PbS-CdS core-shell QDs synthesized from 3.33 and 3.45 nm PbS core with different reaction time and cadmium acetate concentrations.

3.33 nm PbS core			3.45 nm PbS core		
CdS shell thickness [nm]	Cd-oleate [µl]	Time [min]	CdS shell thickness [nm]	Cd-oleate [µl]	Time [min]
0.01	14	6	0.01	29	7
0.02	30	7	0.05	66	10
0.07	69	10	0.11	114	15
0.14	12	15	0.15	175	18
0.18	190	18	0.22	260	19
For all synthesis, the PbS core was injected into the specified volume of Cd-oleate solution at 90 ℃. After the specified reaction time, the PbS-CdS core-shell NCs were quenched by addition of hexane.					

6.3 Determining the number of bound 5-CT transmitter ligands per PbS-CdS core-shell NC

The **5-CT**/ PbS-CdS transmitter/ NC complex was isolated as described in Section 4.2 above, then redispersed in toluene. Figure S4a shows the absorption spectrum of these NCs as the **5-CT** concentration in the ligand exchange solution in toluene increases. Due to the fact that the absorption spectrum of **5-CT** and PbS NCs overlap in the visible, in order to calculate the number of bound ligands, the contribution of the NCs must be taken into account. As a result, the number of bound **5-CT** ligands was estimated by subtracting the absorption spectrum of the NCs from that of the **5-CT**/ PbS-CdS complex (Fig. S4a) to give Figure S4b. Interestingly, these surface bound **5-CT** ligands show a 7 nm red shift in their absorption spectrum, an indication of successful ligand exchange (Figure S3). Finally, the number of bound ligands per NC were calculated from the measured optical density at 482 nm in Figure S4b, the extinction coefficient of **5-CT** at 482 nm, and knowledge of the NC concentration.

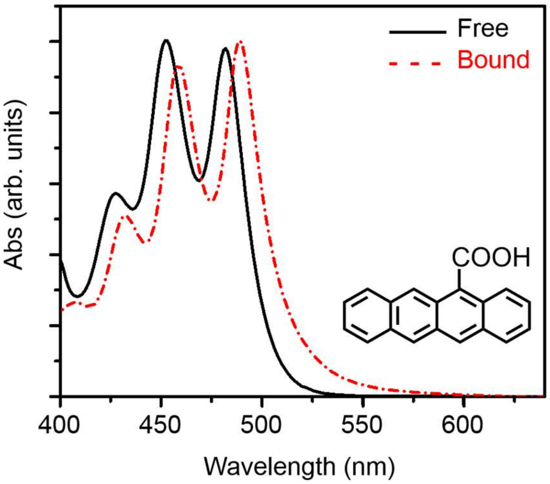

Figure S3. The absorption spectrum of free **5-CT** molecules (black solid line) and **5-CT** transmitter ligands (red dashed-dotted line) bound to PbS-CdS core-shell NCs with 2.7 nm core diameter and 0.24 nm shell thickness, in toluene at RT. The red shift of the bound **5-CT** ligands indicates a change in its dielectric environment.

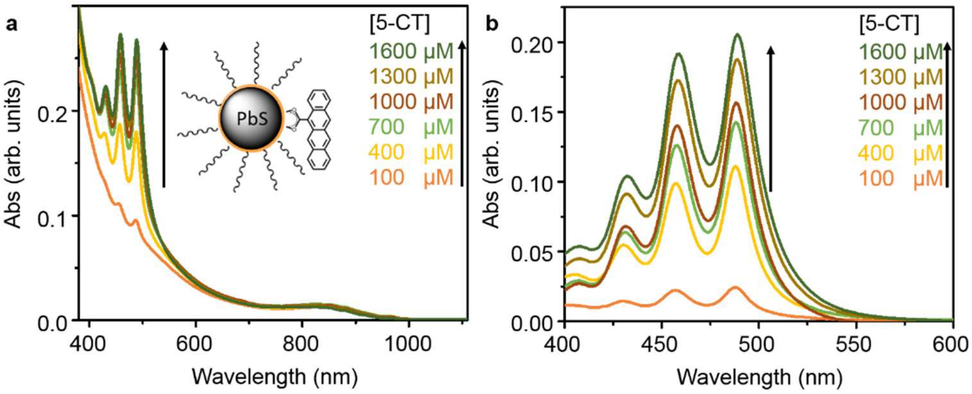

Figure S4. Evolution in the absorption spectrum of **a**, ligand exchanged PbS-CdS core-shell NCs with bound **5-CT** transmitter ligands and **b**, As in part (a) but with the NC contribution removed. The average number of **5-CT** molecules bound to the PbS-CdS core-shell NCs surface increases as the concentration of **5-CT** in the ligand exchange solution increases. This **5-CT** absorption spectrum were calculated by subtracting the contribution of NCs in the absorption spectrum obtained in Fig. S4a (see Section 5). All measurements are in toluene at RT. The PbS-CdS core-shell NCs have a 2.7 nm core diameter and 0.24 nm shell thickness.

6.4 Molar extinction coefficient of 5-CT

Extinction coefficient of **5-CT** at 482 nm is 5.3×10^3 $M^{-1}cm^{-1}$. **5-CT** ligands were dissolved in a 10:1 volume toluene/THF mixture. Then the extinction coefficient of **5-CT** at 482 nm were calculated by measuring the absorption of the 5 different **5-CT** solutions in toluene made by dilution of the stock **5-CT** solution, and linear fit to the absorption vs concentration plot. All the absorptions were less than 0.1 for the optical density at the absorption maxima to prevent excimer formation.

6.5 Linear relation between Φ_{TET} and k_{et}

We can relate Φ_{TET} to the rate of energy transfer (k_{et})

$$\Phi_{TET} = \frac{n k_{et}}{k_r + k_{nr} + n k_{et}} \quad (2)$$

k_r, and k_{nr} are the intrinsic radiative and nonradiative decay rates of the NCs. The average number of rubrene molecules involved in the energy transfer from the NC to rubrene is denoted by *n*. We can assume *n*, the number rubrene acceptors is constant since an increase in CdS shell thickness from 0.11 to 0.22 nm merely leads to a 1.05 times increase in overall NC volume (see section 6.1). Upon cw excitation, the excited state of the NC can decay radiatively or non-radiatively via energy transfer to rubrene. Therefore $k_r+k_{nr}+nk_{et}$ is constant and is proportional to the absorption cross-section of the NC. Considering that *n* and $k_r+k_{nr}+nk_{et}$ are constant, Φ_{TET} is linearly related to k_{et}.

6.6 Estimation of number of available rubrene molecules for energy transfer

For the oleic acid PbS-CdS core-shell NCs that did not undergo ligand exchange (i.e. no **5-CT** transmitter ligand on the surface), *n*, the average number of rubrene molecules involved in energy transfer is approximately constant as the PbS-CdS core-shell NC's diameter is increased from 3.26 to 3.45 nm. Considering the NC's radius and the molecular dimensions of oleic acid (1.79 nm), the NC volume varies from 167.6 to 173.5 nm^2. With a rubrene concentration of 20 mM, the average number of rubrene per 1 nm^3 is about 0.012. Hence, for all the NCs, the number of available rubrene molecules inside of a 10 nm×10 nm× 10 nm box is similar and approximately equal to 10.

6.7 Estimation of solar photon flux

To estimate the solar flux that can excite the 850 nm PbS-CdS core-shell NCs, we integrate the area under the curve of the AM 1.5 solar spectrum (Fig. S5a) from 750 nm to 850 nm (the NC absorption edge). The available solar power flux from 750 to 850 nm (10.2 mW/cm^2) is three times higher than threshold excitation density in our system (3.2

mW/cm^2) marking the transition from the quadratic to the linear regime. Similarly, the available photon flux is calculated by integrating the photon flux in AM1.5 from 750 to 850 nm (Fig. S5b).

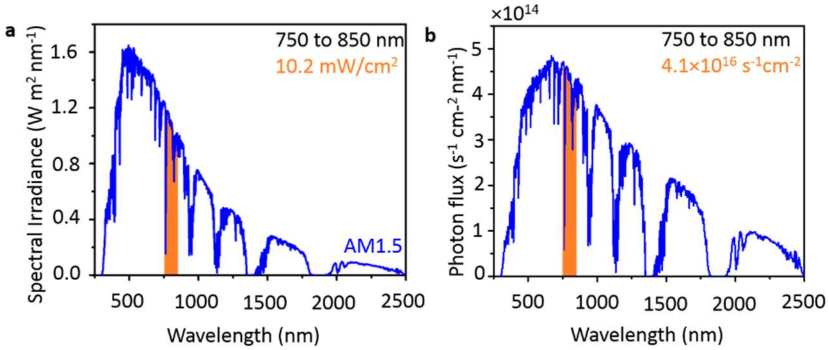

Figure S5. Available solar and photon flux from the absorption tail of rubrene (750 nm) to the absorption tail of the PbS-CdS core-shell NCs (λ_{abs}=850 nm) that gave the 8.4% upconversion quantum yield. **a,** Spectral irradiance of the AM 1.5 solar spectrum. The available solar flux is calculated from integrating from 750 to 850 nm. **b**, Photon flux of the AM 1.5. The available solar photon flux is calculated from integrating from 750 to 850 nm.

5.8. Ionic radii and redox potential of exchangeing cation

Table S3. Ionic radii and redox potential for Zn^{2+},Cd^{2+}, In^{2+},Ni^{2+}, Sn^{2+}, Pb^{2+}, Bi^{2+} cations

Compound	Crystal ion radii (pm)	Redox potential (V)
$Zn^{2+}(aq)+2\ e^{-} \rightarrow Zn\ (s)$	87	-0.76
$Cd^{2+}(aq)+2\ e^{-} \rightarrow Cd\ (s)$	109	-0.40
$In^{2+}(aq)+2\ e^{-} \rightarrow In\ (s)$	94	-0.34
$Ni^{2+}(aq)+2\ e^{-} \rightarrow Ni\ (s)$	83	-0.26
$Sn^{2+}(aq)+2\ e^{-} \rightarrow Sn\ (s)$	118	-0.14
$Pb^{2+}(aq)+2\ e^{-} \rightarrow Pb\ (s)$	119	-0.13
$Bi^{2+}(aq)+2\ e^{-} \rightarrow Bi\ (s)$	117	+0.31

6.8 Core-shell QDs synthesis

6.8.1 Materials

Lead oxide (PbO, 99.999%), oleic acid (OA, tech. grade, 90%), 1-octadecene (ODE, 90%), bis(trimethylsilyl) sulfide ($(TMS)_2S$), cadmium acetate hydrate ($Cd(OAc)_2 \cdot H_2O$, 99.99%), zinc acetate ($Zn(OAc)_2$, 99.99 %), cobalt (II) acetate ($Co(OAc)_2$, 99.995 %), sodium dodecyl sulfate (SDS), dry ethanol, methanol, hexane, dimethyl sulfoxide (DMSO) were purchased from Sigma-Aldrich. Tin (II) acetate ($Sn(OAc)_2$, 99 %) and nickel (II) acetate ($Ni(OAc)_2$, 99.999 %) were purchased from Strem Chemical, Inc.

and bismuth (III) acetate ($Bi(OAc)_3$, 99.99 %) were obtained from Alfa Aesar. Dry and degassed toluene, acetone, were obtained from JC Meyer's solvent purification system.

6.8.2 Adsorbing cations to the PbS QDs

3.12, 3.18 and 3.23 nm diameter PbS QDs was synthesized following our previous work[1]. Then the PbS core was subjected to the following conditions to produce PbS-CdS and PbS-ZnS core-adsorbate QDs.

Varying amounts of metal-acetate salts were dissolved in oleylamine, and then injected into the PbS core QDs in toluene at 90°C. Oleylamine was used instead of oleic acid because we observed an enhancement in the upconversion QY of a 3.12 nm diameter PbS QDs by a factor of 10 when treated with zinc acetate in oleylamine rather than in oleic acid. Note the solubility of cations in oleylamine is higher due to the higher basicity of the amine functional group. This means reaction at relatively lower temperatures (90°C) and thus allowing better control of the process[2]. Reaction with oleylamine at the higher temperature of 120°C resulted in a lower upconversion QY. However when using oleylamine, the PbS-ZnS core-shell QDs with shell thickness of more than 0.23 Å agglomerated and could not be resuspended. Colloidally stable QDs were obtained when the cation exchange reaction was quenched with oleic acid.

6.8.3 PbS-CdS and PbS-ZnS core-shell QD Synthesis

PbS–CdS and PbS-ZnS core–shell QDs were synthesized as follows. The cadmium precursor was made by addition of 69.8 mg of cadmium acetate hydrate into 0.814 and 0.187 ml of ODE and oleylamine. The zinc precursor was made by addition of 46.1 mg of zinc acetate into 1.972 ml oleylamine. These precursor solutions were heated at 120 ℃ for about 30 minutes until a clear solution formed. Then different aliquots of cadmium and zinc precursors was transferred into a 4 ml vial followed by 237.5 µl of 17.2 mg/ml PbS solution while stirring at 90 ℃. Right after injection the temperature were set to 80 ℃. After 7 minutes, 300 µl oleic acid was injected followed by the injection of 208 µl hexane to quench the reaction. Then particles were cleaned once with addition of 0.7 ml acetone and twice with addition of 0.434 ml methanol. After each cleaning, the pellets were dissolved in 0.2 ml hexane. Finally the QDs were dissolved in toluene and stored in the dark in glovebox.

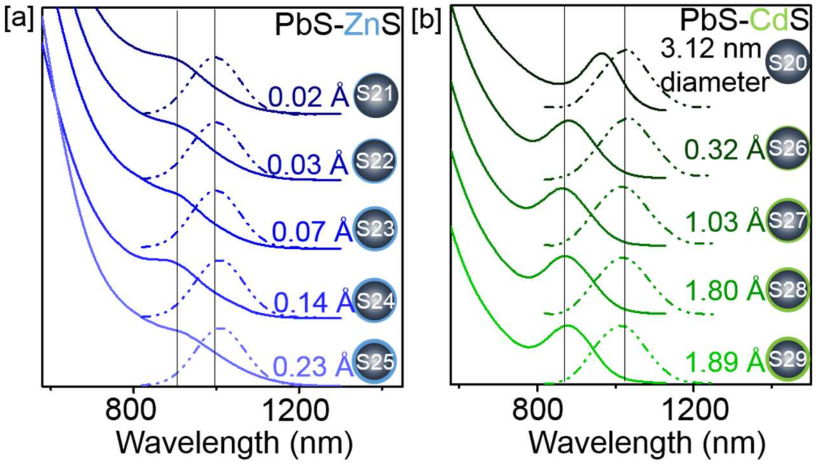

Figure S6. The absorption (solid line) and photoluminescence spectrum (dashed-dot line) of [a] PbS-ZnS (blue) and [b] PbS-CdS (green) core-adsorbate QDs with various shell thicknesses from a 3.12 nm diameter PbS QD core. The spectra were obtained in toluene at RT.

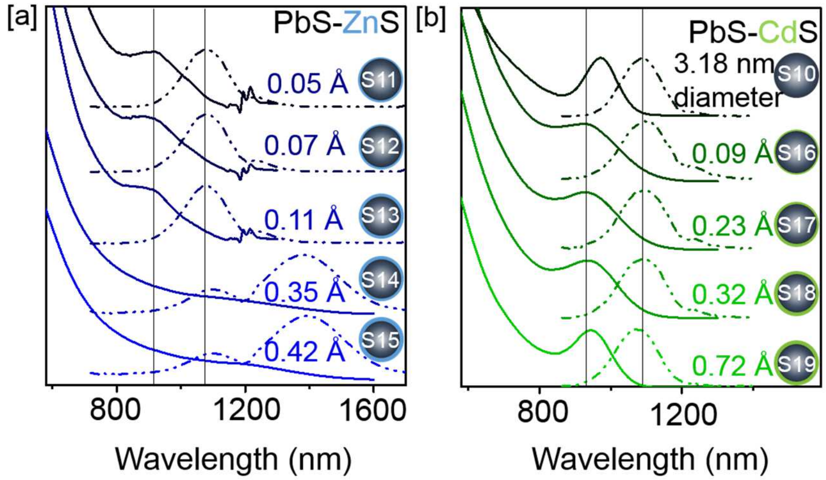

Figure S7. The absorption (solid line) and photoluminescence spectrum (dashed-dot line) of [a] PbS-ZnS (blue) and [b] PbS-CdS (green) core-adsorbate QDs with various shell thicknesses from a 3.18 nm diameter PbS QD core. The spectra were obtained in toluene at RT.

The aliquots employed for synthesis of different shell thickness of core-adsorbate QDs are listed below:

Table S4: PbS-ZnS core-shell QDs synthesized from 3.12 nm diameter PbS QD cores with different aliquots of zinc-acetate solution in oleylamine.

Sample #	ZnS shell thickness (nm)	Zn-acetate (µl)
PbS20	0	0
PbS-ZnS21	0.002	60
PbS-ZnS22	0.003	30
PbS-ZnS23	0.007	10
PbS-ZnS24	0.014	150
PbS-ZnS25	0.023	250

Table S5: PbS-ZnS core-shell QDs synthesized from 3.18 nm diameter PbS QD cores with different aliquots of zinc-acetate solution in oleylamine.

Sample #	ZnS shell thickness (nm)	Zn-acetate (µl)
PbS10	0.000	0
PbS-ZnS11	0.005	60
PbS-ZnS12	0.007	30
PbS-ZnS13	0.011	10
PbS-ZnS14	0.036	150
PbS-ZnS15	0.042	250

Table S6: PbS-ZnS core-shell QDs synthesized from 3.23 nm diameter PbS QD cores with different aliquots of zinc-acetate solution in oleylamine.

Sample #	ZnS shell thickness (nm)	Zn-acetate(µl)
PbS0	0.000	0
PbS-ZnS1	0.004	30
PbS-ZnS2	0.009	60
PbS-ZnS3	0.022	150

Table S7: PbS-CdS core-shell QDs synthesized from 3.12 nm diameter PbS QD cores with different aliquots of cadmium-acetate solution in oleylamine and oleic acid.

Sample #	CdS shell thickness (nm)	Cd-acetate (μl)
PbS20	0.000	0
PbS-CdS26	0.009	1
PbS-CdS27	0.023	3
PbS-CdS28	0.032	4
PbS-CdS29	0.072	10

Table S8: PbS-CdS core-shell QDs synthesized from 3.18 nm diameter PbS QD cores with different aliquots of cadmium-acetate solution in oleylamine and oleic acid.

Sample #	CdS shell thickness (nm)	Cd-acetate(μl)
PbS10	0.000	0
PbS-CdS16	0.009	1
PbS-CdS17	0.023	3
PbS-CdS18	0.032	4
PbS-CdS19	0.072	10

Table S9: PbS-CdS core-shell QDs synthesized from 3.23 nm diameter PbS QD cores with different aliquots of cadmium-acetate solution in oleylamine and oleic acid.

Sample #	CdS shell thickness (nm)	Cd-acetate (µl)
0	0.000	0
PbS-CdS4	0.037	2.5
PbS-CdS5	0.060	4
PbS-CdS6	0.160	10

6.9 Instrumentation

Transmission electron microscopy (TEM) was carried out on a FEI Tecnai12 TEM with the accelerating voltage set to 200 kV.

Absorption spectra was recorded on a Jasco-V670 UV–Vis absorption spectrophotometer. A 0.24 W/cm^2 785 nm Coherent OBIS laser was used for excitation during the linear photon upconversion experiments.

6.9.1 Photon upconversion

The upconverted light was collected following our previous work[3] where a 100 µm thick capillary tube (LRT-010–2–10 Friedrich & Dimmock, Inc.) inside an air-free cuvette for holding the sample was used for front face detection. This attenuates the parasitic reabsorption of the upconverted light. For blocking the excitation beam, a 745 nm short-pass filter (FF01-7450/SP-25 BrightLine multiphoton) and 532 nm notch filter (NF01-532U-25 Semrock) were used. Finally the upconversion signal was detected by an Ocean Optics JAZ spectrometer focused by a lens (focal length of 30 mm) into a PAF-

SMA-11-A (Thor Laboratories) fiberport connected to an Ocean Optics QP400–2-SR fiber. We calculated the upconversion QY from the following equation:

$$\Phi_{\mathrm{UC}}=2\Phi_{\mathrm{ref}}\times\frac{\text{(photons absorbed by reference)}}{\text{(photons absorbed by sample)}}\times\frac{\text{(photons emitted by sample)}}{\text{(photons emitted by reference)}}$$

(S1)

Considering possible errors in upconversion detection, laser power and background, the error in upconversion QY can be roughly calculated to be 0.5×10^{-5} %.

6.9.2 Time correlated single photon counting (TCSPC)

Photoluminescence lifetimes were recorded on a Picoharp Time-Correlated Single Photon Counting setup (Picoharp 300). Samples were excited by ultrafast pulses (190 fs, 35.7 kHz) centered at 480 nm from a light source consisting of a femtosecond laser system (PHAROS, Light Conversion) pumping an optical parametric amplifer and second harmonic generator (ORPHEUS/LYRA, Light Conversion). Excitation intensity was controlled by variable neutral density filters. For detection, a 512 channel InGaAs/InP Single-Photon Avalanche Diode (quasi free-running mode with gated module, Micro Photon Devices S.r.l.) was used and a count rate of <1% of the excitation rate was maintained. Fits were made to single exponential decays with a y-offset and the amplitude averaged lifetime $<\tau>$ was the amplitude-weighted average lifetime extracted from the fits.[1]

6.9.3 Relative PLQY measurements

The relative PLQY of QDs were measured in 3.5 mL air-free, quartz Starna cuvettes by recording the PL spectra of QDs and indocyanine green (ICG) dye as a PLQY reference on a PTI QuantaMaster 400–HORIBA. QDs were dissolved in air-free anhydrous toluene while ICG was dissolved in anhydrous dimethyl sulfoxide. Absorption at the excitation wavelength for all the QD samples and the dye was less than 0.1 to minimize the inner filter effect. ICG has a known PLQY of 12 % in dimethyl sulfoxide[4]. The excitation wavelength was set to 680 nm for both QDs and the dye reference. The PL spectra were corrected for the collection efficiency of the PTI QuantaMaster 400–HORIBA.

6.9.4 Inductively coupled plasma-optical emission spectroscopy (ICP-OES)

Perkin-Elmer Optima 7300DV was used for the ICP-OES characterization. Toluene was removed from QDs by vacuum at 100 mTorr for around 3 min. Aqua regia was added to the QDs to digest the QDs at RT. QDs were immediately dissolved after addition of the acid. The solutions were diluted to form a 2% (weight to weight ratio) aqua regia solution. Then the final solutions were filtered with a 0.22 μm Millex-GP syringe filter with PES membranes before the ICP measurements.

6.10 Calculation of shell thickness from ICP-OES analysis

Shell thickness was calculated from the ICP-OES analysis. Here, we assume the total core-shell QD volume remains constant after cation exchange, i.e. the final radius is equal to the radius of the PbS QD parent, which is 1.59 nm. Hence shell thickness can be calculated by subtraction of total core-shell radius (R) by the core radius (r). Core radius can be calculated from the ICP-OES analysis and the volumes corresponding to the shell and core are as follow:

$$V_{CdS/ZnS} = \frac{4}{3}\pi(R^3 - r^3) \text{ and } V_{PbS} = \frac{4}{3}\pi R^3 \tag{S1}$$

For PbS-CdS core-shell: $$a = \frac{n_{Pb}}{n_{Cd}} = \frac{n_{PbS}}{n_{CdS}} = \frac{\dfrac{V_{Pbs} \times \rho_{PbS}}{MW_{PbS}}}{\dfrac{V_{CdS} \times \rho_{CdS}}{MW_{CdS}}} . \tag{S2}$$

Hence $$r^3 = \frac{R^3}{(1 + \dfrac{0.952}{a})} \tag{S3}$$

For PbS-ZnS core-shell: $$b = \frac{n_{Pb}}{n_{Zn}} = \frac{n_{ZnS}}{n_{PbS}} = \frac{\dfrac{V_{Pbs} \times \rho_{PbS}}{MW_{PbS}}}{\dfrac{V_{ZnS} \times \rho_{ZnS}}{MW_{ZnS}}}, \tag{S4}$$

Hence $$r^3 = \frac{R^3}{(1 + \dfrac{0.757}{b})} \tag{S5}$$

Here V_{PbS}, V_{CdS}, *and* V_{ZnS} are the volumes corresponding to the PbS core, CdS shell, and ZnS shell in a nanocrystal. The molar ratios of the cations *a* and *b* are calculated from ICP-OES analysis. MW and ρ are the molecular weight and the density respectively.

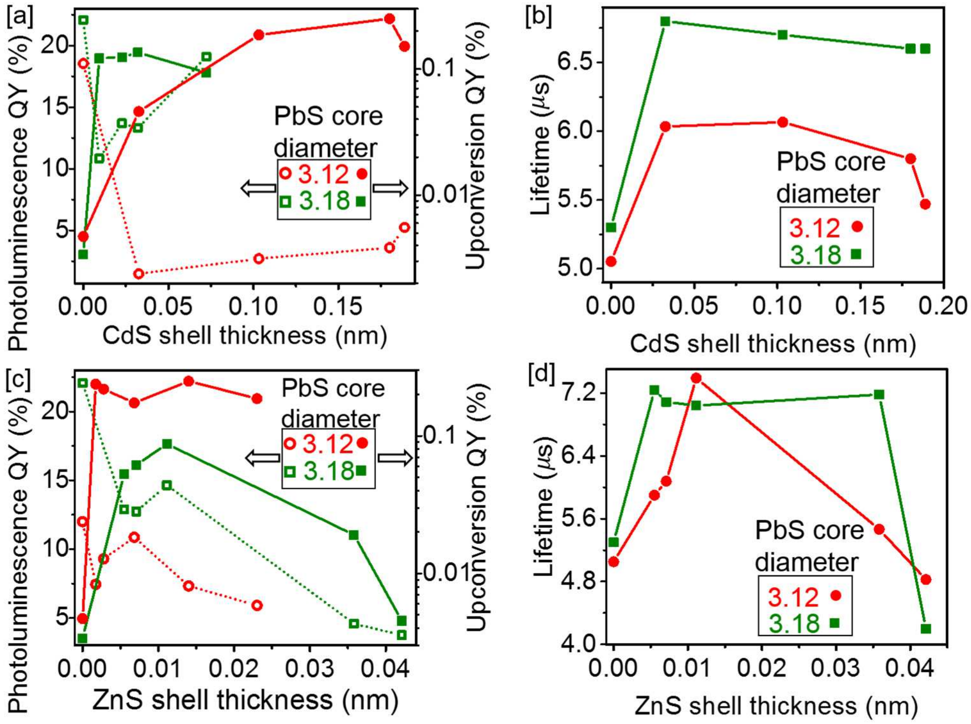

Figure S8. The photon upconversion QT (solid lines) and photoluminescence QY (dotted lines) of [a] PbS-CdS and [c] PbS-ZnS core-adsorbate QDs from 3.12 and 3.18 nm diameter PbS parent cores. The QDs were dissolved in 20 mM rubrene in toluene and were excited by 0.24 W/cm^2 785 nm CW laser. For photoluminescence QY the optical density of the QDs at the excitation wavelength was 0.002. Photoluminescence decay lifetime of [c] PbS-CdS and [d] PbS-ZnS core-shell. All measurements were performed in toluene at RT and shell thicknesses were calculated from ICP-OES.

6.11 Time-correlated single photon counting (TCSPC)

Around 10μM of QDs were dissolved in toluene in air free 3.5 ml Starna cuvettes. QDs were excited at 480 nm with a 1.437 μW pump at a repetition rate of 35.7 kHz. The step time was set to 512 ps. The excess bias, gate width, gate frequency, and hold-off time was set to 2.0V, 20.00 ns, 20 MHz, and 30 μs respectively. The rising point was assigned to zero, and the decay lifetimes were simply calculated by fitting a monoexponential decay function (see below).

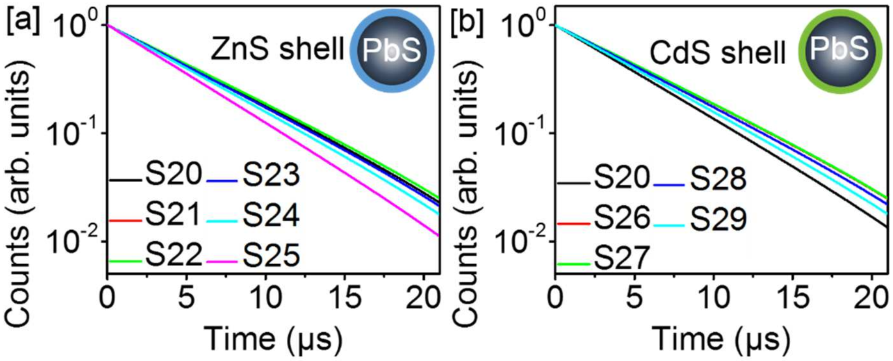

Figure S9. The photoluminescence lifetimes of [a] PbS-ZnS and [b] PbS-CdS core-shell QDs from 3.12 nm diameter PbS cores are monoexponential.

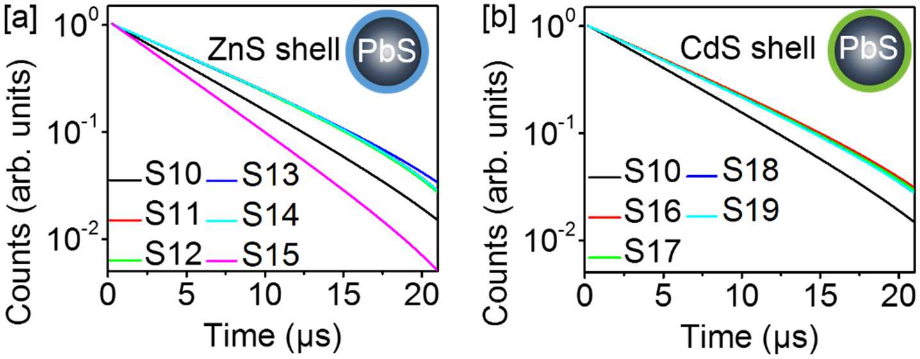

Figure S10. The photoluminescence lifetimes of [a] PbS-ZnS and [b] PbS-CdS core-shell QDs from 3.18 nm diameter PbS cores are monoexponential.

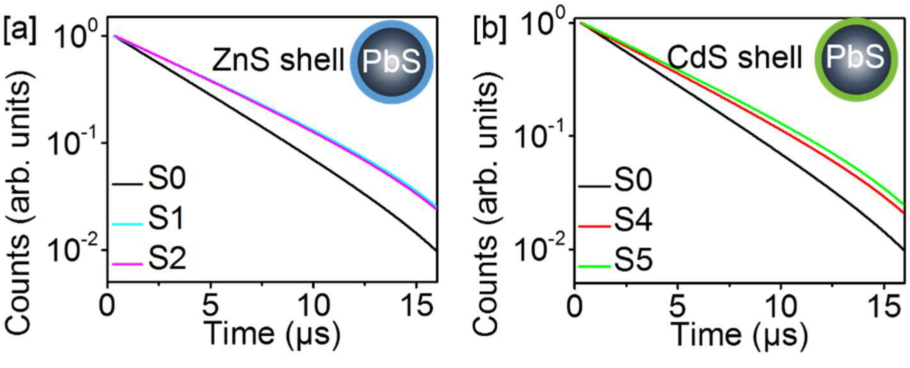

Figure S11. The photoluminescence lifetimes of [a] PbS-ZnS and [b] PbS-CdS core-shell QDs from 3.23 nm diameter PbS cores are monoexponential.

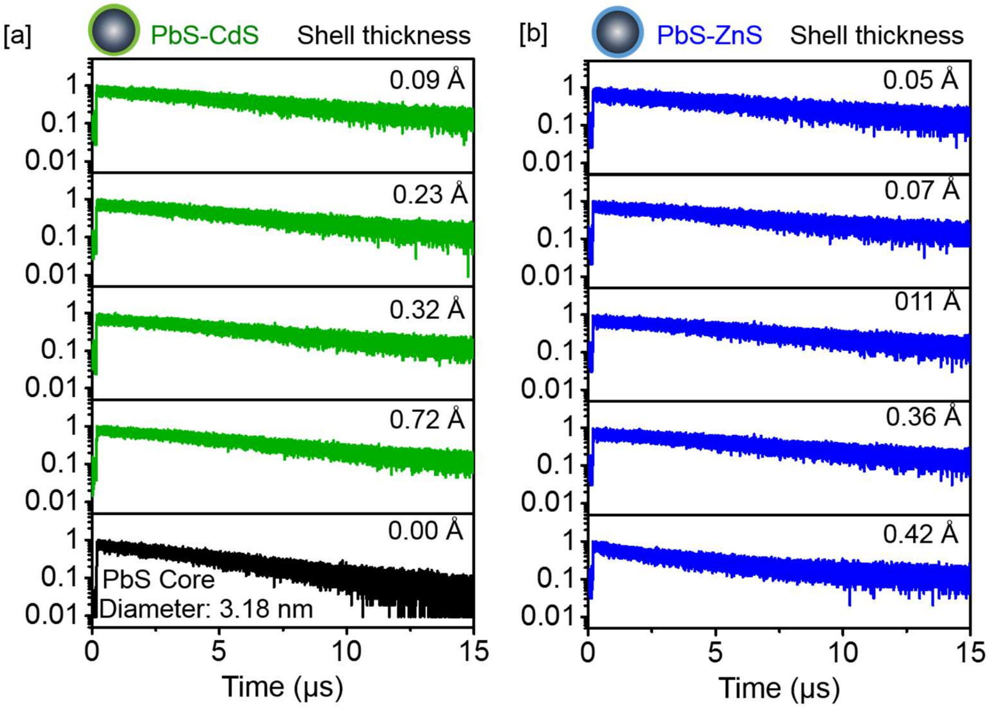

Figure S12. PL decay lifetime from TCSPC measurements of core-shell QDs with different shell thickness from 0.000 to 0.072 nm and 0.005 to 0.042 nm for [a] PbS-CdS and [b] PbS-ZnS core-shell QDs synthesized from 3.18 nm in diameter PbS core QD respectively in toluene at RT. QDs were excited at 800 nm with 1.43 μW picosecond laser. The repetition rate was set to 31.3 kHz. All QDs were fitted with monoexponential decays.

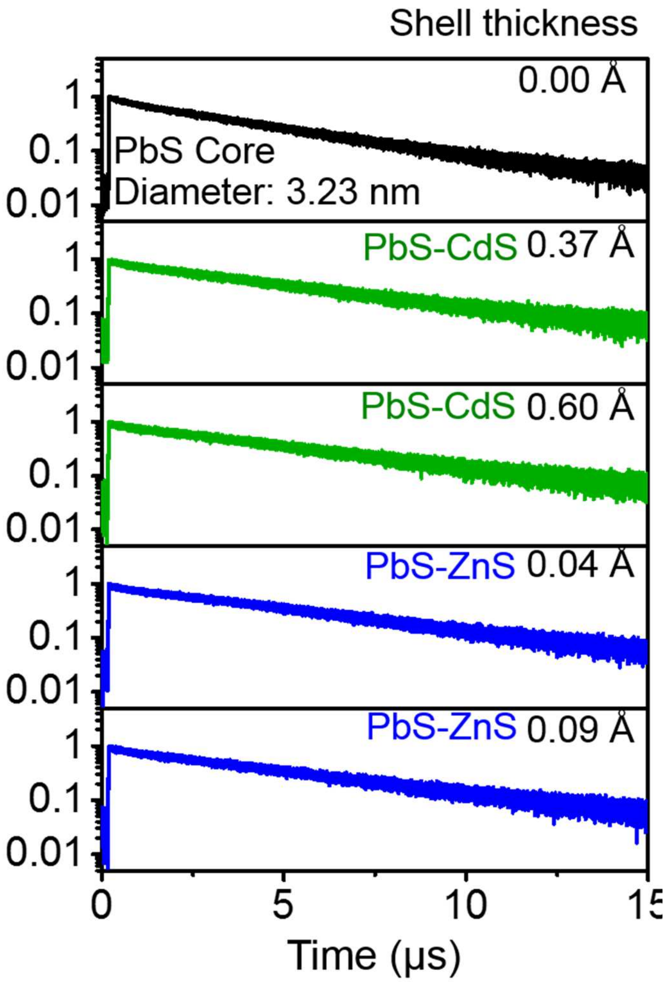

Figure S13. PL decay lifetime from TCSPC measurements of core-shell QDs with different shell thickness from 0.000 to 0.060 nm and 0.004 to 0.009 nm for PbS-CdS and PbS-ZnS core-shell QDs synthesized from 3.23 nm in diameter PbS core QD respectively in hexane at RT. QDs were excited at 800 nm with 1.43 μW picosecond laser. The repetition rate was set to 31.3 kHz. All QDs were fitted with monoexponential decays and the results of the fits are in Table 1.

6.12 PL QY quenching of differantly sized PbX (X=S and Se) NCs

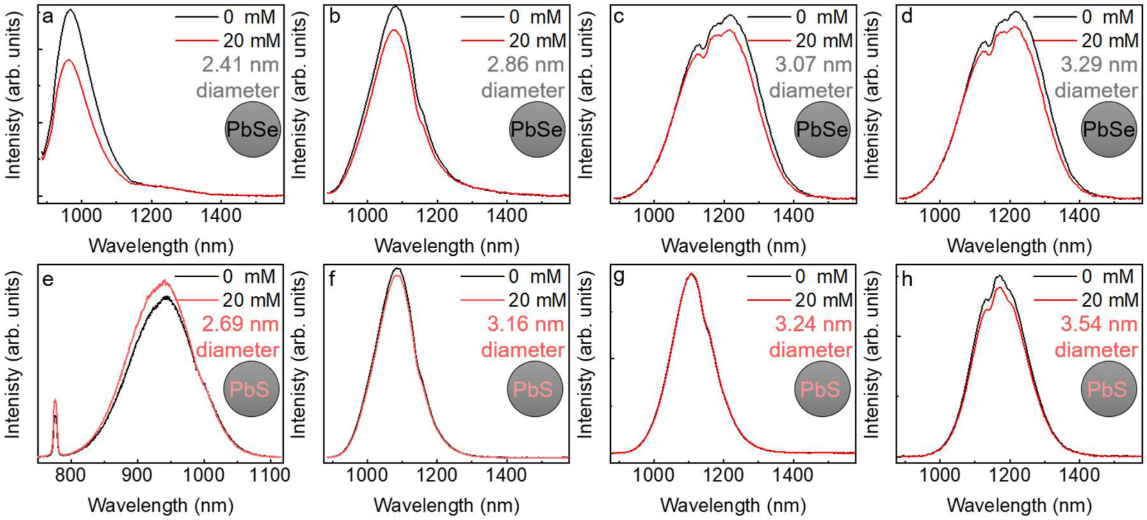

Figure S14. Photoluminescence spectra of differently sized PbSe NC (a, b, c, and d) and PbS NCs (e, f, g, and h) normalized by NCs absorption at excitation wavelength with 0 and 20 mM rubrene concentrations. PbSe and PbS NCs diameter varies from 2.41 to 3.29 and 2.69 to 3.54 nm. More PL quenching is observed for PbSe NCs in the presence of 20 mM rubrene. Samples were dissolved in dry and degassed toluene and were excited at 781 nm at RT.

6.13 References

[1] M. Mahboub, H. Maghsoudiganjeh, A. M. Pham, Z. Huang, M. L. Tang, Advanced Functional Materials 2016, 6091-6097.

[2] H. Zhao, M. Chaker, N. Wu, D. Ma, Journal of Materials Chemistry 2011, 21, 8898.

[3] Z. Huang, D. E. Simpson, M. Mahboub, X. Li, M. L. Tang, Chemical Science 2016.

[4] W. Shao, G. Chen, A. Kuzmin, H. L. Kutscher, A. Pliss, T. Y. Ohulchanskyy, P. N. Prasad, Journal of the American Chemical Society 2016, 138, 16192.